Title

Bioengineered technological platforms for quantitative understanding of cancer

Author

Aung, Aereas

Publication Date

2016

UNIVERSITY OF CALIFORNIA, SAN DIEGO

Bioengineered technological platforms for quantitative understanding of cancer

A dissertation submitted in partial satisfaction of the

requirements for the degree Doctor of Philosophy

in

Bioengineering

by

Aereas Aung

Committee in Charge:

Professor Shyni Varghese, Chair
Professor David Cheresh
Professor Juan Carlos del Alamo
Professor Juan Lasheras
Professor Geert Schmid-Schoenbein
Professor Shankar Subramaniam

2016

The dissertation of Aereas Aung is approved, and it is acceptable in quality and form for publication on microfilm and electronically:

Chair

University of California, San Diego

2016

Epigraph

"It is not the critic who counts; not the man who points out how the strong man stumbles, or where the doer of deeds could have done them better. The credit belongs to the man who is actually in the arena, whose face is marred by dust and sweat and blood."

Theodore Roosevelt, *The Man in The Arena*

Table of Contents

Signature page.. iii

Epigraph.. iv

Table of Contents.. v

List of Figures.. xii

List of Tables…………………………………………………………………………xv

Acknowledgements... xvi

Vita………………………………………………………………………………………xix

Abstract of the Dissertation xxi

Chapter 1: *In vitro* systems to study and model cancer progression.................................. 1

  1.1 Introduction.. 1

  1.2. *In vitro* systems to investigate cancer cell migration... 2

    1.2.1. 3D cell migration 2

    1.2.2. 3D cell migration Assays 4

  1.3. Cancer-on-chip devices... 6

    1.3.1. 2D versus 3D cultures.. 6

    1.3.2. Microfluidics-based platforms 7

    1.3.3. Organ-on-chip integrated cancer platforms 8

  1.4. Cancer-immune cell interactions 9

    1.4.1. Clinical outlook on immunotherapy 9

    1.4.1. Path towards immunosuppression.. 10

1.4.3. Role of monocytes and their polarized phenotypes within the tumor microenvironment 11
1.4.4. Importance of T-cell trafficking into cancer stroma and its implications 13
1.5. Conclusion 14
1.6. Figures 16
1.7. Tables 20
Chapter 2: 3D Traction stresses activate protease-dependent invasion of cancer cells 22
2.1. Abstract 22
2.2. Introduction 23
2.3. Materials and Methods 24
2.3.1. Cell Culture 24
2.3.2. Fabrication of Matrigel networks tethered to glass 25
2.3.3. Cell invasion and imaging 26
2.3.4. Removal of cells after cell invasion 27
2.3.5. Mechanical Yielding Tests of Matrigel Networks 27
2.3.6. MT1-MMP FRET Analysis 29
2.3.7. Zymography and fluorogenic peptide assay 29
2.3.8. Immunofluorescence Staining and Imaging 33
2.3.9. Quantitative Cell Invasion assay 34
2.3.10. Quantification of the matrix indentation profile caused by the invading cells from confocal images 34
2.3.11. Calculation of 3D Traction Stresses During Cell Invasion 36

2.3.12. Reference-free Estimation of Normal Traction Stresses During Cell Invasion 37

2.3.13. Estimation of Apparent Young Modulus Encountered by the Invading Cells 39

2.3.14. Characterization Of Matrigel Networks 40

2.4. Results and discussion 40

2.4.1. Invasion of MDA-MB-231 cells into Matrigel networks 40

2.4.2. Effect of mechanical resistance on invasion of MDA-MB-231 cells 43

2.5. Conclusion 46

2.6. Acknowledgements 46

2.7. Figures 48

Chapter 3: MT1-MMP trafficking in protease dependent invasion of cancer cells utilizes CARTS secretory pathway 64

3.1. Abstract 64

3.2. Introduction 65

3.3. Materials and Methods 66

3.3.1. Cell Culture 66

3.3.2. Plasmid Transfection 67

3.3.3. siRNA knockdown 67

3.3.4. Activation of glass surface 68

3.3.5. Fabrication of 30 μm thick Matrigel networks tethered to glass 68

3.3.6. Single cell invasion assay 69

3.3.7. Image analysis to quantify maximum invasion depth, h_{inv} 70

3.3.8. Immunofluorescent Staining 70

3.3.9. PAUF Secretion Assay 72

3.3.10. Western blot 73

3.4. Results 74

3.4.1. Cancer cells transition from protease independent to dependent mode during invasion 74

3.4.2. Protease dependent invasion utilizes CARTS pathway 74

3.4.3. Inhibition of CARTS pathway impairs cancer cell invasion 75

3.4.4. CARTS pathway inhibition prevents invadopodia formation during cancer cell invasion 76

3.4.5. Integrin dependent invasion of cancer cells into Matrigel network 77

3.5. Discussion 77

3.5.1. Additional evidence of CARTS pathway involvement in MT1-MMP Transport 78

3.5.2. Context specific use of CARTS during cancer cell invasion 79

3.5.3. Invadopodia formation and CARTS inhibition 79

3.6. Acknowledgements 80

3.7. Conclusion 81

3.7. Figures 82

Chapter 4: Chemotaxis-driven assembly of endothelial barrier in a tumor-on-a-chip platform 96

4.1. Abstract 96

4.2. Introduction 97

4.3 Materials and Methods 98
4.3.1. Cell culture 98
4.3.2 MCF7 Spheroid Formation 99
4.3.3. Fabrication of Silicon Mold 99
4.3.4. Synthesis of lithium phenyl-2,4,6-trimethylbenzoylphosphinate (LAP) as a photoinitiator 100
4.3.5. Synthesis of Gelatin Methacrylate (GelMA) 100
4.3.6. Fabrication of Tumor-on-a-Chip Device 101
4.3.7. Quantification of cell motility within the cell-laden GelMA hydrogel structures 104
4.3.8. Quantification of MCF7 spheroids growth within GelMA hydrogel structures 105
4.3.9. FITC-Dextran diffusion into cell-laden GelMA hydrogel 106
4.3.10. Immunofluorescence staining of HUVECs 106
4.3.11. Doxorubicin solution 107
4.3.12. Penetration of Doxorubicin into spheroid-laden GelMA structures 107
4.3.13. Confocal microscopy for imaging immunofluorescently stained cells 108
4.3.14. Effect of flow rates on mechanical compression of the GelMA hydrogels 108
4.3.15. Modeling of mass transfer within the cell-laden GelMA hydrogel structures 109
4.4. Results 109
4.4.1. Formation and characterization of trilayer hydrogel-based device 109
4.4.2. Flow induces concentration gradient within GelMA structures 110

4.4.3. Migration of HUVECs to the periphery of 3D GelMA structures 113
4.4.4. Co-Culture of HUVECs and cancer cell spheroids 114
4.4.5. Characterization of the HUVEC layer at the periphery of the hydrogel structure 115
4.4.6. Dose dependent response of cells within the GelMA hydrogel to Doxorubicin 116
4.5. Discussion 117
4.6. Acknowledgements 119
4.7. Figure 121
Chapter 5: Engineered tumor-on-a-chip device with cancer immune interactions for assessing T-cell recruitment 133
5.1. Abstract 133
5.2. Introduction 135
5.3. Materials and Methods 137
5.3.1. Cell Culture 137
5.3.2. MCF7 spheroid formation 138
5.3.3. Fluorescent labeling of cells 138
5.3.4. Preparation of GelMA hydrogel precursor solution 139
5.3.5. Fabrication of tumor-on-a-chip device for additive photopatterning 139
5.3.6. TALL-104 cell infiltration assay 142
5.3.7. Analysis of TALL-104 cell distribution within GelMA hydrogel 143
5.4. Results 143

    - 5.4.1. Characterization of 3D photopatterned GelMA hydrogels within a fluidics device 143
    - 5.4.2. Monocytes intravasate into the perfused media from the GelMA hydrogel containing a multi-cellular co-culture 144
    - 5.4.3. Additive 3D photopatterning for spatial organization and compartmentalization of multi-cellular co-cultures 145
    - 5.4.4. Formation of a cancer spheroid-immune cell co-culture encased within an endothelial barrier using the additive photopatterning approach 145
    - 5.4.5. Isolating the effect of cancer cell-cell contact using a dispersed cancer and immune cell co-cultures 146
    - 5.4.6. Monocytes and cancer spheroid synergistically recruit T-cells into the cell-laden GelMA hydrogel 147
  - 5.5. Discussion 149
  - 5.6. Acknowledgements 152
  - 5.7. Figures 153
- Chapter 6: Future Directions 157
- References 160

List of Figures

Figure 1.1: Various modes of 3D migration 16

Figure 1.2: Vasculature formation by endothelial cells 17

Figure 1.3: Integration of different organ systems.. 18

Figure 1.4: Cancer immune interactions 19

Figure 2.1: Verification of Matrigel network thickness.. 48

Figure 2.2: Effect of cell dissolving solution on the Matrigel network. 49

Figure 2.3 Efficiency of cell removal. 50

Figure 2.4: Schematic representation of the experiments utilized to determine the mechanical yielding of the Matrigel in the absence of cells. 51

Figure 2.5: Secreted proteases during cell invasion using zymography. 52

Figure 2.6: Protease activity during invasion of MDA-MB-231 cells into 30 μm thick Matrigel networks. 53

Figure 2.7: Quantitative single cell invasion assay 54

Figure 2.8: Characterization of Matrigel networks tethered to glass. 55

Figure 2.9. Quantification of the matrix indentation profile caused by the invading cells from confocal images. 56

Figure 2.10: Effect of time on degree of permanent deformation. 57

Figure 2.11: Invasion of MDA-MB-231 cells into 30 μm thick Matrigel networks. 58

Figure 2.12: Matrigel networks exhibit complete elastic recovery for compressive stresses >200 Pa. 59

Figure 2.13: Invasion of cells in serum free conditions. 60

Figure 2.14: Morphological transition at the leading edge of the cells invading into 30 μm thick Matrigel. 61

Figure 2.15 Effect of mechanical resistance on the invasion of MDA-MB-231 cells into Matrigel networks. 62

Figure 2.16: Establishing the dependence of γ on $h_{w/cell}$ ϕ_{3D}, and τ_{zz}. S 63

Figure 3.1: Protease independent invasion of MDA-MB-231 cells into 30 μm thick Matrigel networks. 82

Figure 3.2: Protease dependent invasion of MDA-MB-231 cells into 30 μm thick Matrigel networks. 83

Figure 3.3: MT1-MMP transport through CARTS pathway during MDA-MB-231 cell invasion. 84

Figure 3.4: Colocalization of MT1-MMP and PAUF within MDA-MB-231 cells invading into 30 μm thick Matrigel network. 85

Figure 3.5: CARTS inhibition abrogates MDA-MB-231 invasion into 30 μm thick Matrigel network. 86

Figure 3.6: Effect of H89 on MDA-MB-231 cell invasion. 87

Figure 3.5: Downregulation of TGN46 inhibits the formation of invadopodia-like protrusions in MDA-MB-231 cells. 88

Figure 3.6: Colocalization of MT1-MMP and PAUF within MDA-MB-231 cells invading into 30 μm thick Matrigel network. 89

Figure 3.7: Effect of H89 on MDA-MB-231 cell invasion. 90

Figure 3.7: Validation of TGN46 downregulation in MDA-MB-231 subsequent to Si-RNA treatment. 91

Figure 3.8: Validation of TGN46 downregulation in PC3 subsequent to Si-RNA treatment. 92

Figure 3.9: Downregulation of TGN46 inhibits the formation of invadopodia-like protrusions in MDA-MB-231 cells. 93

Figure 3.10: Downregulation of Eg5 inhibits the formation of invadopodia-like protrusions in MDA-MB-231 cells. 94

Figure 3.11: Down regulation of β1 and β3 integrin abrogates cancer cell invasion. 95

Figure 4.1: Schematic of fabrication of tumor-on-a-chip devices. 121

Figure 4.2: Co-culture of HUVECs and MCF7 spheroids within GelMA structures. 122

Figure 4.3: Flow-induced migration of encapsulated HUVECs. 123

Figure 4.4: Characterization of the device. 124

Figure 4.5: Flow induced compression of GelMA hydrogels 125

Figure 4.6: Concentration gradient within GelMA hydrogels. 126

Figure 4.7: Transient concentration changes within the GelMA hydrogel. 127

Figure 4.8: Steady state profile within the GelMA hydrogel 128

Figure 4.9: Cancer spheroids remain clustered within the GelMA hydrogel with culture time. 129

Figure 4.10: Immunostaining of HUVECs cells migrated to the periphery of the GelMA structure 130

Figure 4.11: Diffusion of FITC-Dextran into cell-laden GelMA hydrogels. 131

Figure 4.12: Dose-dependent response of encapsulated tumor spheroids to Doxorubicin. 132

Figure 5.1: Single step encapsulation process for co-cultures of cancer cells, monocytes, and endothelial cells 153

Figure 5.2: Additive photoencapsulation process for a spatially controlled co-culture of cancer spheroid, monocytes and endothelial cells. 154

Figure 5.3: Co-culture system with dispersed cancer cells, monocytes, and endothelial cells. 155

Figure 5.4: TALL-104 cell infiltration into bilayer GelMA hydrogels laden with cells. 174

List of Tables

Table 1.1. Summary of different modes of 3D migration.. 20

Table 1.2. Summary of chemokines secreted within the cancer microenvironment 21

Acknowledgements

I would like to sincerely thank and acknowledge a few individuals who have contributed tremendously towards the completion of my graduate degree. I would like to first and foremost thank my wife, Susan Lin, who has been by my side since high school. I would like to thank her for being my strongest supporter and my anchor when everything around me gets tumultuous. I would also like to thank her for being patient and understanding about the commitment required by my graduate career. Most importantly, I would like thank her for loving me for who I am which allowed me to remain to true to myself irrespective of any circumstance.

Secondly, I would like to thank my advisor, Shyni Varghese, for accepting me into her lab as an undergraduate student without any prior experience or knowledge. In addition, she devoted tremendous amount of time to teach and train me despite other obligations required by her faculty position. Furthermore, I would like to thank her for her sincere concern for my wellbeing and truly looking out for my future. Lastly, I would like to thank her for giving me the freedom to make mistakes and explore without limits, which allowed me to grow into the scientist that I am today.

I would also like to thank those who have shaped and molded my scientific abilities throughout my research career. To this end, I would like to thank Prof. Chao Zhang for guiding me as an undergraduate research assistant and instilling a sense of scientific disciple. I would like to thank him for teaching me the true meaning of being meticulous. I would also like to thank Dr. Juan Carlos del Alamo for helping me understand biology from a quantitative perspective. I have gained a tremendous amount of knowledge and insights from our collaboration.

In addition, I would like to thank the present and the past Varghese lab members, especially the recent devices sub-group, for their comradery on my journey towards my doctorate degree. This lab is truly unique for its strong sense of community and I am appreciative and grateful to have been a part of it during my graduate career.

I would also like to acknowledge the ARCS foundation for financially supporting my Ph.D. career as well as providing the rare opportunity to meet kind and caring individuals. Their generosity and effort has instilled in me a sense of desire to give back to the community in any way possible.

Lastly, I would like to thank my parents, Patrick and Sherry Aung, for the hardships they have endured to ensure that my sister and I have promising futures. They have built the foundation on which I could stand to reach for my goals and I truly thank them for their countless sacrifices and unconditional affection.

Chapter 1, in full, is a literature review on the topics discussed within this dissertation. "*In vitro* systems to study and model cancer progression." Aung, Aereas. The dissertation author was the only author for this section.

Chapter 2, in full, is a reprint of the material as it appears in Biophysical Journal, vol. 107, 2014. "3D Traction stresses activate protease-dependent invasion of cancer cells". Aung, Aereas; Seo, Young N.; Lu, Shaoying; Wang, Yingxiao; Jamora, Colin; del Alamo, Juan Carlos; Varghese, Shyni. The dissertation author was the primary investigator and author of this paper.

Chapter 3, in full, is currently being prepared for submission for publication of the material. “MT1-MMP trafficking in protease dependent invasion of cancer cells utilizes CARTS secretory pathway”. Aung, Aereas; Shih, Yu-Ru; Jamora, Colin; Varghese, Shyni. The dissertation author is the primary investigator and author of this material.

Chapter 4, in full, is a reprint of the material as it appears in Lab on a Chip, vol. 16, 2016. “Chemotaxis-driven assembly of endothelial barrier in a tumor-on-a-chip platform”. Aung, Aereas; Theprungsirikul, Jomkuan; Lim, Han L; Varghese, Shyni. The dissertation author was the primary investigator and author of this paper.

Chapter 5, in full, is currently being prepared for submission for publication of the material. “Engineered tumor-on-a-chip device with cancer-immune interactions for assessing T-cell recruitment”. Aung, Aereas; Theprungsirikul, Jomkuan; Davey, Shruti K.; Varghese, Shyni. The dissertation author is the primary investigator and author of this material.

Vita

2010	Bachelor of Science in Bioengineering: Biotechnology, University of California San Diego, La Jolla, United States
2016	Doctor of Philosophy in Bioengineering, University of California San Diego, La Jolla, United States

Publications

Lim, H.L.†, **Aung, A.**†, Varghese, S. "Mechanical oscillations and dynamic malleability in collectively migrating cell clusters." (Manuscript in preparation).

Agrawal, G.†, **Aung, A.**†, Theprungsirikul, J., Varghese, S. "Assessing maturation of engineered skeletal muscle in perfused microfluidics environment". (Manuscript in preparation).

Davey, S.K. †, **Aung, A.** †, Theprungsirikul, J., Varghese S. "Novel approach to quantify the dynamic matrix mechanical properties during cancer growth." (Manuscript in preparation).

Aung, A., Theprungsirikul, J., Davey, S.K., Varghese, S. "Engineered tumor-on-a-chip device with cancer-immune interactions for assessing T-cell recruitment". (Manuscript in preparation).

Aung, A., Theprungsirikul, J., Lim, H.L., Varghese, S. "Chemotaxis-driven assembly of endothelial barrier in a tumor-on-a-chip platform." *Lab on a Chip*. 16(10): 1886-98, 2016.

Aung, A.†, Bhullar, I.†, Theprungsirikul, J., Davey, S.K., Lim, H.L., Chiu, Y., Ma, X., Dewan, S., Lo, Y., McCulloch, A., Varghese, S. "3D cardiac µtissues within microfluidics device with real-time contractile force read out." *Lab on a Chip*. 16: 153-162. 2016.

Davey, S.K.†, **Aung, A.**†, Agrawal, G., Lim, H.L., Kar, M., Varghese, S. "Embedded 3D photo-patterning of hydrogels with diverse and complex architectures for tissue engineering and disease models." *Tissue Engineering: Part C*. 21(11): 1188-1196. 2015.

Aung, A., Seo, Y.N., Lu, S., Wang, Y., Jamora, C., del Alamo, J.C., Varghese, S. "3D Traction stresses activate protease-dependent invasion of cancer cells." *Biophysical Jour*. 107 (11): 2538-37. 2014.

Caro-Diaz, E.J.E., **Aung, A.**, Xu, J., Varghese, S., Theodorakis, E.A. "Fusarisetins: Structure-function studies on a novel class of cell migration inhibitors." *Organic Chemistry Frontiers.* 1(2): 135-39. 2014.

Aung, A.†, Gupta, G.†, Majid, G., Varghese, S. "Osteoarthritic chondrocyte-secreted morphogens induce chondrogenic differentiation of human mesenschymal stem cells." *Arthritis & Rheumatism*. 63 (1): 148-58. 2011.

Ayala, R., Zhang, C., Yang, D., Hwang, Y., **Aung, A**., Shroff, S.S., Arce, F.T., Lal, R., Arya, G., Varghese, S. "Engineering the cell-material interface for controlling stem cell adhesion, migration, and differentiation." *Biomaterials*. 32 (15): 3700-11. 2011.

Lim, H.L., Chuang, J.C., Tran, T., **Aung, A.,** Arya, G., Varghese, S+. "Dynamic Electromechanical Hydrogel Matrices for Stem Cell Culture." *Advanced Functional Materials.* 21 (1): 55-63. 2011.

Zhang, C., **Aung, A**., Liao, L., Varghese, S. "A novel single precursor-based biodegradable hydrogel with enhanced mechanical properties." *Soft Matter.* 5 (20): 3831-34. 2009.

Patents

Varghese, Shyni. **Aung, Aereas**. 2015. Microfluidic based perfusion devices. Application Number: 62/145,900. Filed April 10, 2015. Patent Pending.

Abstract of the Dissertation

Bioengineered technological platforms systems for quantitative understanding of cancer

by

Aereas Aung

Doctor of Philosophy in Bioengineering
University of California, San Diego, 2016

Professor Shyni Varghese, Chair

In the United States, cancer is the second leading cause of death only to be surpassed by heart diseases (1). Within 2016, an estimated 1.6 million new cases of cancer will be diagnosed and approximately 0.6 million individuals will die from this disease (1). The survival rate of individuals afflicted with cancer have increased over the

years due to early detection and increased fundamental understanding of this disease. However, the complex nature of cancer exceeds the current capacity to recapitulate its features *in vitro.* Additionally, the animal models that have been relied upon within the field of oncology may not be translatable to the human counterpart (2-5). In this dissertation, I have created novel *in vitro* technological platforms focusing on specific aspects of cancer progression. With these tools, I have identified underlying biological phenomenon and recapitulated the *in vivo* cancer microenvironment to provide better alternatives for the screening of cancer drugs.

Chapter 1 is a literature review focusing on cancer cell migration during metastasis and *in vitro* platforms used to model the cancer microenvironment. Specifically, I have focused on the role of the extracellular matrix (ECM) network on modulating the protease dependent or independent mode of migration during metastasis. *In vitro* systems used to study cancer cell metastasis within 3D matrices are also briefly reviewed. Next, I have described the use of organ-on-a-chip technology as the potential platforms towards creating low cost, efficient, and realistic tumor models for screening of oncologic drugs. Lastly, I have summarized the emergence of a potent cancer treatment, immunotherapy, and its mechanism through the immune cells within the tumor environment are activated to eliminate cancer. Furthermore, I have discussed the crucial role of cytotoxic T-cells in immunotherapies and the means by which they are recruited to the tumor stroma.

Studies have implicated the physical cues of the cancer microenvironment in modulating the particular mode of migration. In Chapter 2, I have investigated how these various cues activate an intracellular “trigger” to dictate a cell’s mode of invasion. I have

developed a novel single cell invasion assay to quantitatively investigate the interplay between cell generated traction forces and protease activity during cancer cell invasion into a basement membrane-like ECM network known as Matrigel. Within these studies, I observed the translocation of a crucial membrane bound protease, MT1-MMP, from the cytoplasm to the cell surface to degrade the surrounding protein network. Chapter 3 further investigates the transport pathway through which this translocation occurs. The results from this study implicate a regulated secretory pathway known as CARTS responsible for MT1-MMP transport and the protease dependent invasion of cancer cells. In addition to understanding cancer cell metastasis, I next shifted my research focus towards recreating the cancer microenvironment to test the efficacy of cancer drugs. Chapter 4 describes the development of a state-of-the-art 3D tumor-on-a-chip platform containing cancer and endothelial cells to assess the penetration and efficacy of cancer drugs. Here, I have used a morphogen gradient to induce the self-assembly of an endothelial and cancer cell mixture resulting in a tumor mass enveloped by an endothelial layer. The drug screening capacity of this system was assessed using doxorubicin as a model drug. Current immunotherapies rely on the presence of cytotoxic T-cells within the tumor microenvironment to eliminate cancer cells. In Chapter 5, I have adapted the tumor-on-a-chip device to incorporate immune cells to recapitulate cancer-immune interactions and investigate its effect on the recruitment of T-cells into the engineered microenvironment. In the last chapter, I have discussed potential applications for the platforms that I have created to better understand and investigate interactions between cancer and immune cells. Specifically, I have discussed the inclusion of macrophages as well as primary immune cells into the system for increased physiological relevance.

Chapter 1: *In vitro* systems to study and model cancer progression

1.1 Introduction

Cancer is an epidemic that is touted to claim the lives of approximately half a million individuals within the US alone in 2016 (1). This mortality rate is only to be superseded by heart disease. Over the years, the mortality rate for patients afflicted with all types of cancer has decreased due to early detection and treatment of this disease (6, 7). Such improvements can be attributed to the growing understanding of how cancer progresses as well as identifying novel therapeutics that disrupts certain stages of the disease. Despite the discovery of such approaches, numerous aspects of cancer have yet to be understood. Current methods to understand cancer as a disease involve a plethora of studies relying on animal models, particularly mice (2-5). Although these models offer the biological complexity that better mimics the physiological conditions within the human body, these *in vivo* systems still lack a desired level of control and understanding which poses a need for alternative *in vitro* systems. In particular, studies investigating cancer cell migration within extracellular (ECM) networks, the role of stromal cells on disease progression, or drug penetration into a tumor microenvironment have a growing need for well-defined microenvironments to better isolate the effect of single variables on the outcome of the experiments.

1.2. *In vitro* systems to investigate cancer cell migration

1.2.1. 3D cell migration

Unlike migration on 2D surfaces, migration of cancer cells within a 3D ECM network is complex phenomena that intricately balances the cell-generated forces, malleability of the ECM network and cell body, and proteolysis to allow cells to traverse a protein network (8). For single cells, two distinct modes of migration, amoeboid and mesenchymal, exist (Figure 1.1, Table 1.1) (9).

During the amoeboid mode of migration, cells maintain a rounded phenotype as they translate the cell bodies with minimal (pseudopodal) or non-adhesive (blebby) contacts with the ECM (10). In the specific context of pseudopodal migration, the movement of cells is mediated by a mixture of Rac activated membrane protrusions and loose adhesion at the front and Rho mediated contractions at the rear of the cell (11). For bleb-associated migration, the movement of cells is completely driven by Rho-mediated acto-myosin contractions (10, 12, 13). This form of movement has been touted to be associated with the forward propulsion of cell body caused by cellular contractions at the rear. In general, amoeboid mode of migration is devoid of protease activity as cells are observed to "squeeze" and deform around ECM proteins to traverse an ECM network (12, 14). In contrast, mesenchymal mode of migration is associated with elongated cell morphology, moderate to high ECM adhesivity, and Rac-mediated cellular protrusions at the front of the cell (15). In this mode of migration, cells have been observed to rely on protease degradation to traverse ECM network.

The properties of the ECM network have been touted to dictate the particular mode of migration (16). In particular, the physical properties of the ECM network such as pore size, topographical structure, and rigidity induce a specific type of migration. For ECM networks with high rigidity and pore sizes smaller than ~ 0.2 microns, cells are unable to displace the ECM proteins to propel the cell body forward (17, 18). As a result, cells tend to rely on mesenchymal mode of migration in protease activity and large forces are induced within the migrating cell. On the other hand, soft and cell deformable ECM networks with small or large pore sizes may encounter cells migrating under amoeboid mode of migration (9). Within this context, cells will employ the appropriate mode of migration based on their ability to physically "squeeze" or rely on proteolysis to "break" through their microenvironment (16). Interestingly, topographical cues have been shown to influence the mode of migration. Cells encounter various types of ECM proteins during migration *in vivo.* For instance, cells adopt a mesenchymal mode of migration on based on the fibrillar and anisotropic arrangement of collagen bundles, and such structural arrangements have been shown to induce proteolytic activity in migrating cells (19, 20).

Cell motility within a 3D environment are generated from actomyosin contraction at the cell rear to propel the cell forward or within the protrusions at the cell front to pull the cell body forward. Propulsive forces are often observed during amoeboid movement or migration within soft ECM networks. Furthermore, these forces are used to overcome cells with low adhesion strength to the substrate thereby allowing the cells to easily propel forward (12). On the other hand, the contractile forces generated within the frontal membrane protrusions are often observed during mesenchymal migration (16). The high adhesion strength of the cells to the ECM substrate provides the needed anchor to allow the cells to pull their rear forward without detaching from the network (15, 21).

Nevertheless, several exceptions have been observed in which elongated cells with low adhesion strength are capable of migrating with low traction stresses (13, 22). It is most probable that several combinations and archetypes of force generations and adhesion patterns exist that has yet to be identified.

1.2.2. 3D cell migration Assays

Assays for 3D cell migration can be generalized into two categories: embedded cell migration and invasion into ECM networks (23). For embedded cell migration assays, cell(s) are encapsulated with an ECM network and their movement within the protein network is analyzed. Due to the abundance and remodeling of collagen in *in vivo* tumors, cancer cells are usually encapsulated within collagen of varying percentages, mesh, or fiber size (24). Within such systems, the migration of cells is usually tracked to assess the mean distance traveled or even its directionality in the presence of potential chemoattractants (25, 26). Recent studies have also employed the use of polyacrylamide and collagen hydrogel bilayers to approximate the forces generated by the cancer cells migrating within the collagen network (27). Others have also estimated the strain energy imparted by cancer cells migrating within a collagen hydrogel (28). In addition to single cells, spheroids can also be encapsulated within ECM networks to better study the "jail break" of cancer cells into the cancer stroma (29, 30). Alternative methods for embedded cell migration assays employ the sequential use of plating cells on monolayer surfaces prior to forming an ECM hydrogel over the adhered cells after several days of initial seeding (31). This approach can be considered a hybrid 2D/3D migration since cells may or may not migrate vertically into the gel—the vertical migration is induced by adding chemoattractants above the hydrogel.

For ECM invasion assays, cancer cells are seeded onto the surface of an ECM hydrogel and are allowed to invade into the network. Such approaches are usually combined with transwells where ECM gels are formed on the porous membranes of the upper chamber to assess the invasion of cancer cells from the gel surface to the bottom of the porous membrane (32-34). The use of transwells allows for the use of chemoattractants to facilitate the invasion of cancer cells to the bottom chamber (32). Alternatively, the invasion of cancer cells into ECM networks can be assessed without the use a transwell thus allowing the invasion process to be imaged using a microscope. Such an approach permits the in depth analysis of the invasion process beyond quantifying the number of cells that have invaded into the bottom chamber of a transwell (35, 36). In contrast to using collagen gels to investigate cell migration in 3D, laminin-rich ECM are chosen to recapitulate the escape of cancer cells through the basement membrane during the metastatic process. Commercially available Matrigel is commonly used as a basement membrane substitute although the matrix differs in rigidity compared to its *in vivo* counterpart (35). Similar to the embedded cell migration assays, cancer spheroids can also be used in addition to single cells (37). Recent studies have highlighted alternative approaches to the invasion assay. In particular, Quaranta and colleagues have sequentially used a 2D scratch wound assay on cancer monolayers followed by embedding the cells in Matrigel (31). Such an approach provides directionality for cell migration as the wound area closes with time.

1.3. Cancer-on-chip devices

1.3.1. 2D versus 3D cultures

In the simplest form, monolayer of cancer cells serve as the first drug screening platform to provide information about functional efficacy beyond generating thousands of compounds that are capable of binding to a target molecule. However, the ease of creating cancer spheroids and the emergence of technology to standardize these multi-cellular structures allows drug testing on 3D cultures that better recapitulates *in vivo* tumor compared to cells on 2D surfaces (38, 39). The commonly used method of a hanging drop along with creation of 96 well plates capable of accommodating these cultures allows for rapid and high throughput screen of compounds on cancer spheroids (39). Studies have highlighted stark differences in the reaction of cancer cells to oncologic drugs based on 2D and 3D cultures. The packing of cells within the spheroid provides physiologically relevant barriers to drug penetration (40). In addition, the hypoxic conditions within cancer spheroids upregulate HIF-1 alpha and its associated downstream pathways, which have been shown to induce drug resistance (41). The comparison of cellular responses from 2D verses 3D cultures towards therapeutics highlights the necessity to use more complex models for cancer research. Although cancer spheroids provide a 3D microenvironment for cells, they remain within stagnant culture media, lack stromal cells and, more importantly, microvasculature which is crucial in promoting cancer growth *in vivo*.

1.3.2. Microfluidics-based platforms

The recent advent of organ-on-chip technologies lead to the pursuit of recapitulating disease models within fluidic devices for drug screening purposes. These systems offer several advantages over traditional methods of testing the efficacy of novel oncologic drugs. The capacity to entrap cancer spheroids as well as provide convective flow which recapitulates the circulation present *in vivo* systems. This perfusion-based system provides a more efficient mechanism for delivering nutrients and drugs while removing cellular waste from the growing tumor mass (42). These physiologically relevant conditions lead to differences in dose-dependent responses of cancer spheroids cultured in stagnant versus perfused conditions—stagnation of drug compounds within the spheroid as well as removal of cellular debris from apoptosed cells may resulted in different cellular responses (43, 44). In addition to providing perfusion from the surrounding media, recent studies have incorporated the use of stromal fibroblast and endothelial cells into the cancer microenvironment. George and colleagues have shown the importance of these cells in promoting the formation of vasculature around the cancer spheroids after exposing a mixture of cancer and endothelial cells to fibroblasts (Figure 1.2) (45). Interestingly, the observed vasculature was shown to transport single cancer cells within its lumen. Others have employed similar co-culture approaches to form micro-vessels within fluidic devices (46, 47). Alternatively, vascular channels have been formed via unique flow chamber designs and multi-layered fluidic devices. Within these systems, a membrane or a channel is designed to allow the attachment and proliferation of endothelial cells to form a monolayer (48). Furthermore, cancer cells are positioned behind this monolayer such that the diffusive fluxes from the media must pass through the vascular barrier. Such approaches achieve a more controlled formation of the vasculature since the flow path can be designed to specification. However, the scale of this vasculature is significantly larger than those formed spontaneously. These systems have been used to study cancer cell extravasation, drug, and nanoparticle penetration in the presence of a vascular barrier (48, 49).

1.3.3. Organ-on-chip integrated cancer platforms

Cancer-on-chip platforms provide varying degrees of complexity in comparison to traditional drug screening platforms comprised of 2D monolayers and 3D spheroids. As a result, these systems provide more accurate results in regards to the efficacy of an oncologic drug. During drug discovery and development, the success of the drug is not solely based on efficacy since patient safety must also be considered. As a result, animal studies are carried out to determine both efficacy and toxicity of a given compound and dosage. With the emergence of organ-on-chip systems to model organs such as liver, heart, and lung, the integration of these organ mimics with a disease model provides an attractive platform to determine both efficacy and toxicity within a single platform (50-52). Furthermore, the integration of these organ systems provides a means of crosstalk, which may be crucial in better predicting *in vivo* outcome. Schuler and colleagues have pioneered the integration of these devices involving liver- and cancer-on-chip platforms while maintaining crosstalk by allowing the recirculation of soluble factors between different organ systems and the disease model (Figure 1.3) (53). In addition to providing crosstalk between organ systems, the inclusion of liver cells within the platform allows compounds to be tested where the active forms are generated as secondary metabolites after being metabolized within the liver tissue. In particular, compounds such as 5-fluoro-pyrimidinone (5FP) are required to be metabolized by hepatic aldehyde oxidase to become a pro-drug used to treat cancer (54). Beyond liver tissues, the presence of cardiomyocytes are essential for predicting acute toxicity with the heart tissue thereby eliminating the compound from the drug discovery pipeline (55). Nonetheless, the incorporation of different organ systems is essential for recreating a human *in vitro* model that may pave the path towards accurate and translational drug screening platform in the future.

1.4. Cancer-immune cell interactions

1.4.1. Clinical outlook on immunotherapy

Within this decade, we have witnessed the rise of immuno-oncology (IO) drugs that recruit patients' own immune cells to combat and cure cancer. Such approaches hold great promise as the FDA recently approved several immunotherapeutics where one compound in particular, Ipilimumab, showed a reduction in the risk of death by ~30% and doubled the likelihood of patient survival from 1 to 2 years (56). These results are unprecedented in the field of oncology thus pharmaceutical companies have greatly increased their investment into IO as the number of immunotherapeutics is expected to increase from XY to XZ over the next ZZ years (57). Simply put, immunotherapies are here to stay however their efficacy is expected to increase as the therapeutic mechanism becomes better understood.

1.4.1. Path towards immunosuppression

In most cases, the presence of cancer elicits an immune response due to the recognition of the cancer specific antigen by immune cells (Figure 1.4) (58). Due to this immunosurveillance, cancer cells are eliminated by adaptive and innate immune responses, which recruit macrophages, natural killer cells, and cytotoxic T-cells amongst other immune cells capable of mounting an inflammatory response (59, 60). Under certain circumstances in which the proliferation rate of cancer cells is balanced by the elimination rate of cancer cells by the host immune system, equilibrium is reached which allows cancer cells to mutate under selective pressure to evade or halt the immune response (61, 62). This process occurs via several methods such as the decreased presentation of cancer-specific antigen by the downregulation of MHC class I receptors (63, 64). Furthermore, immuno-suppression can occur directly via expression of immune checkpoint inhibitors such as PD-L1 (65). In addition to directly inhibiting the T-cells as well as decreasing antigen presentation, cancer cells can alter the immune environment through the capacity to recruit anti-inflammatory immune cells. In particular, cancer cells have been shown to induce a Th2 microenvironment that is capable of polarizing macrophages towards alternative activation and recruiting regulatory T-cells (66). Therefore, the suppression of immune system occurs directly via receptors expressed on cancer cell surfaces as well as indirectly through immune cells that promote anti-inflammatory conditions. Cancers showing the presence of immune infiltration yet possess an immune suppressed phenotype has been shown to be most responsive towards immunotherapy treatments (67). Therefore, the need to fully investigate the complex interplay between cancer and immune cells may identify efficacious approaches to overcome the immune suppression process.

1.4.3. Role of monocytes and their polarized phenotypes within the tumor microenvironment

Within the tumor microenvironment, immune cells are comprised predominantly of macrophages. Throughout the progression of cancers, monocytes play crucial roles as they can be polarized towards different phenotypes of macrophages where they have been shown to eliminate cancer during the initial stages while aiding its progression towards metastasis in the latter stages of the disease (68). Specifically, studies have indicated that the monocytes polarized towards classically activated macrophages during immunosurveillance of cancer will eliminate and promote the inflammatory reaction against the cancer cells. However, after cancer-induced suppression of the immune system, alternatively activated macrophages (M2) dominate the macrophage population within the cancer stroma. The shift for in the macrophage population can partly be attributed to the changing cytokine signal in the cancer microenvironment. Specifically, the switch in the presence of T helper cell type I to type II induces the secretion of IL-4 and IL-13 amongst other anti-inflammatory cytokines (66). IL-4 and IL-14 have been shown to have strong effects on the polarization of monocytes towards alternatively activated macrophages. As a result, the increase in the alternatively activated macrophage population may originate from the plasticity of macrophages *in vivo,* in response to changes in the T helper cell mediated cytokine signatures within the cancer microenvironment. However, the exact origin or cause of M2 macrophage population has yet to be identified since recruitment of monocytes followed by subsequent conversion towards alternative activation can also occur.

The presence of alternatively activated macrophages promotes the progression of cancer through a multitude of functions ranging from immune suppression to angiogenesis. For immune suppression, M2 macrophages have been shown to recruit regulatory T-cells via chemokines such as CCL5 and CCL20, secrete TGF-beta and IL-10 both of which interferes with the function of cytotoxic T-cells to eliminate cancer cells, and express PD-L1 to exhaust T-cells (69-71). These activities aid in the suppression of immune cells thereby safeguarding cancer cells against apoptosis. Additionally, these macrophages aid in the remodeling of local ECM networks by the production of proteases (71-73). Softening the microenvironment can potentially facilitate the growth of cancer cells by decreasing the physical resistance provided by the stromal ECM. Furthermore, macrophages have also been shown to secrete soluble factors that promote the metastasis of cancer cells from the primary tumor. The duality of TGF-beta includes the suppression of T-cell activity as well as the induction of epithelial-mesenchyme transition that triggers the metastatic process. In addition, the secretion of EGF promotes the migration of single cancer cells towards blood vessels (74). Lastly, studies have identified the presence of M2 macrophages in hypoxic regions of the cancer masses. Here, M2 macrophages are known to secrete VEGF to promote the formation of vasculature around the tumor (75). Interestingly, studies have also identified hypoxia-induced recruitment of monocytes and their subsequent conversion towards the M2 phenotype (76). Taken together, the macrophages may allow the growth of cancer cells to overcome the diffusion limitation by inducing vasculature formation near to hypoxic regions (76). M2 macrophages have been shown to play a pivotal role in sustaining as well as progressing cancer therefore incorporation of these cells within *in vitro* tumor models is crucial to recapitulate the *in vivo* microenvironment.

1.4.4. Importance of T-cell trafficking into cancer stroma and its implications

The recent application of chimeric antigen receptor (CAR) bearing T-cell therapy against cancer has yielded unprecedented level of success in treating certain types of cancers such as leukemia and melanoma. This therapy isolates a patient's own T-cells from blood, induce the expression of a CAR specific to the patient's cancer antigen, and generate a MHC-independent killing of cancer cells. This potent therapy circumvents some of the immunosuppressive mechanisms created by the cancer cells such as the down-regulation of cancer specific antigens (77). However, the use of CAR T-cell therapy has been limited in the treatment of most solid tumors. The major limitation imposed by solid tumors is the inability of CAR T-cells to effectively infiltrate into the cancer stroma as well as into the tumor mass. Therefore, the understanding of factors inducing efficient T-cell infiltration along with novel therapeutics to bring about such changes are invaluable in translating this therapy towards other types of cancer.

T-cell recruitment is regulated by the presence of key chemokines secreted predominantly by inflammatory immune cells (Table 1.2) (78). Amongst numerous chemokines, CCL3, CCL4, CCL5, CXCL9, CXCL10, CXCL11, and CX3CL1 are responsible for the trafficking of T-cells to the tumor site (79). The expression of several of these chemokines is present within monocytes and classically activated macrophages. However, the expression and secretion of these chemokines within immune suppressive microenvironments have not yet to be well characterized. In addition to chemokines that directly recruit T-cells, the presence of other chemokines that recruit immune cells capable of inducing effector T-cell functions are also vital for a full-scale cytotoxic T-cell response. In particular, the presence of CCL17 and CCL19 have been implicated in the recruitment of dendritic cells which are necessary for antigen presentation along with co-stimulatory receptor activation of cytotoxic T-cells (80).

1.5. Conclusion

This chapter highlights the need for well-defined and controlled *in vitro* platforms to better understand cancer as a disease. These platforms range in varying levels of complexity. From the perspective of single cell migration, *in vitro* platforms general investigate migration within or into an ECM network. Such systems can aid in understanding the interplay that balances ECM remodeling, cell force generation, and cell malleability. Moreover, these systems provide insight into the metastatic process of cancer cells. Next, more complex systems that recapitulate *in vivo* tumor tissues were discussed. These systems were described in the context of microfluidics based technology which allows for better control of assessing drug delivery and penetration into tumors. In addition, these platforms approach the physiologically relevant conditions compared to traditional methods of monolayer or even spheroid cultures. Lastly, the importance of cancer and stromal cell interactions were highlighted from the context of cancer-immune interactions. The emergent trend on the use of immunotherapy as the oncologic treatment of tomorrow coerces the need for improved systems incorporating immune cells. To this end, key immune cells such as macrophages and their role in tumor progression was discussed. Furthermore, the cutting-edge technology of CAR T-cell Therapy aims to spear head the effort towards popularizing immunotherapy treatments for cancer patients. Therefore, the potential triggers for improving the recruitment of T-cells into the cancer microenvironment were reviewed.

1.6. Figures

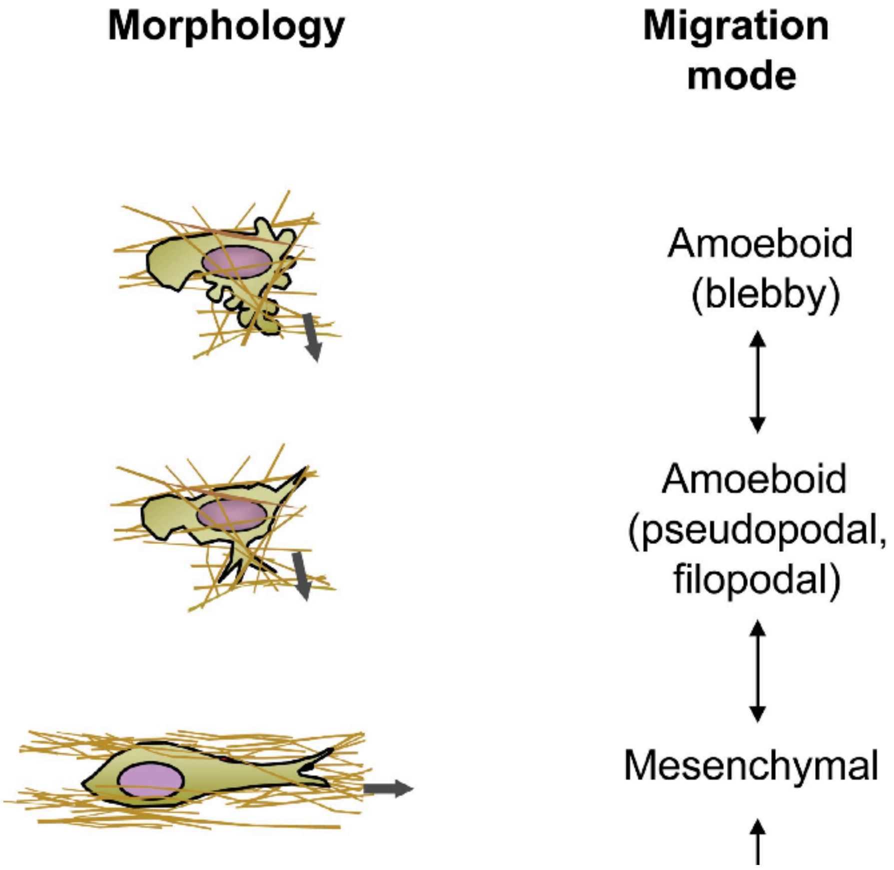

Figure 1.1: Various modes of 3D migration

Cells migrating within 3D ECM networks adopt two distinct modes of migration: amoeboid and mesenchymal. Within the amoeboid mode of migration, cells can adopt a blebby or pseudopodal phenotype characterized by low adhesion and propulsive movements. In mesenchymal mode of migration, cells high adhesion to the substrate as it adopts an elongated phenotype. Reproduced from **(81)**.

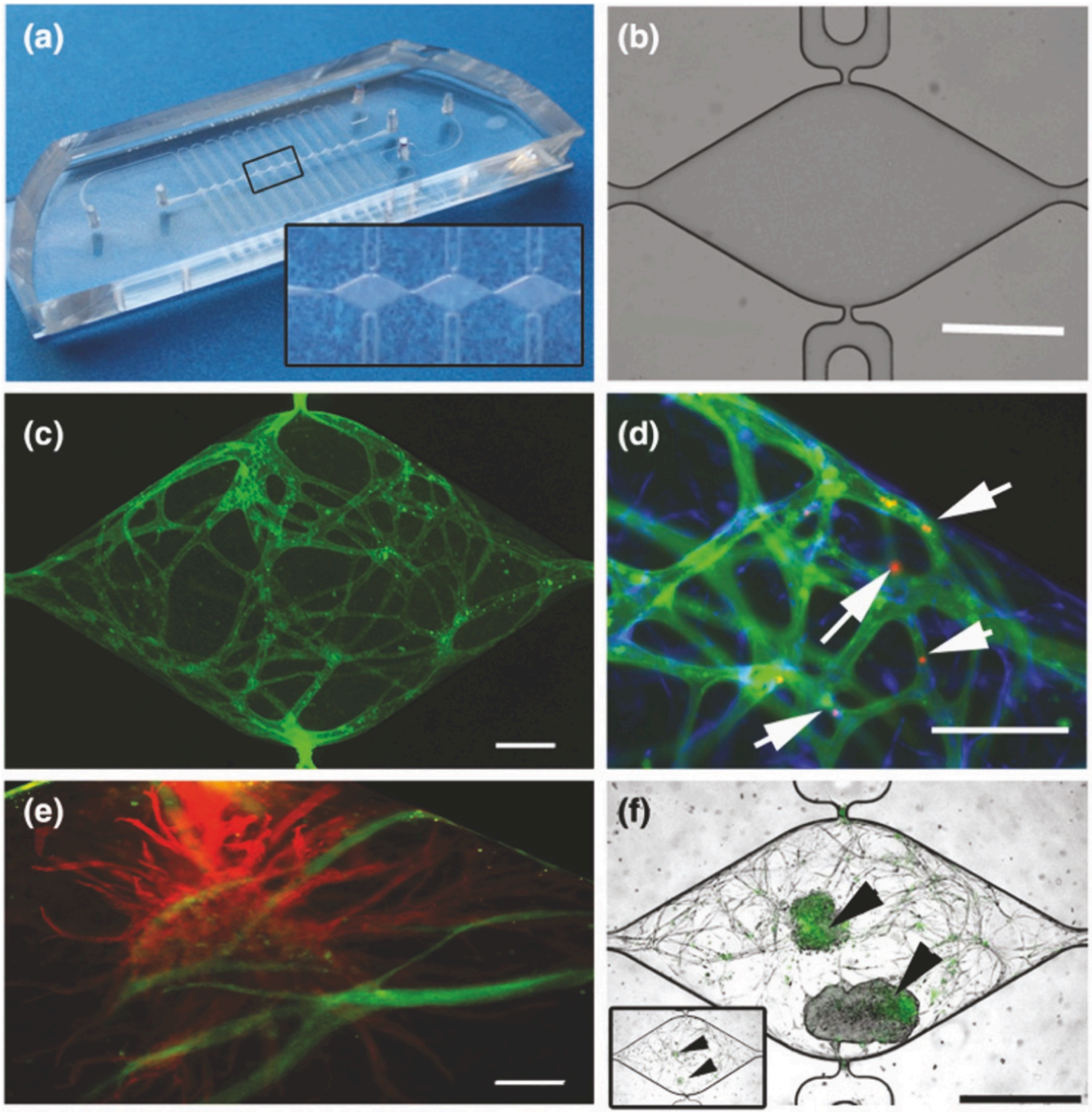

Figure 1.2: Vasculature formation by endothelial cells

(a) Microfluidic device. (b) Image of the interior chamber of the device. (c) Vascular bed formed by endothelial cells stained for CD31 after 14 to 21 days in culture. (d) Magnified image of vascular bed. (e,f) Incorporation of a third cell type such as cancer or cardiomyocytes allows the vasculature to form around the cells. Reproduced from **(82)**.

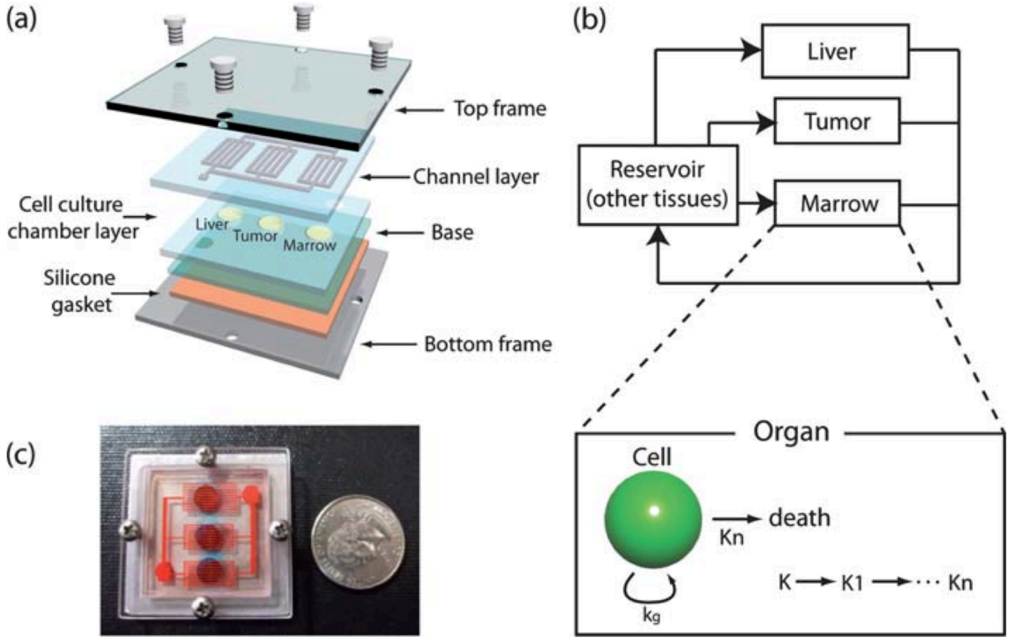

Figure 1.3: Integration of different organ systems

(a) Schematic of the microfluidic device. (b) Diagram of the organ system involved within the device. Here, liver, bone marrow, and a tumor model were integrated together. The interactions are described by a pharmacokinetic model. (c) The actual image of the device next to a dime to illustrate its size. The flow channels contain a red dye solution for visualization purposes. Reproduced from (53).

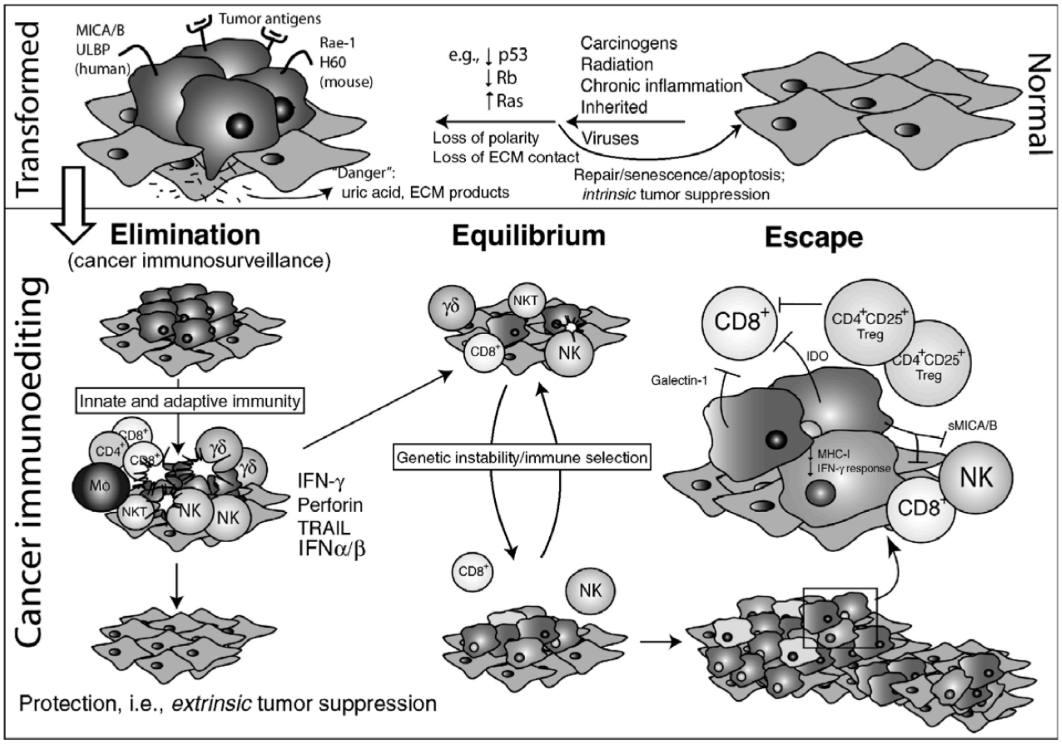

Figure 1.4: Cancer immune interactions

Cancer cells are eliminated by immune systems during immunosurveillance. However, in certain cases, cancer can undergo immunoediting by suppressing the active immune system. Cancer capable of escaping the immune assault progresses towards growth and metastasis. Reproduced from **(58)**.

1.7. Tables

Table 1.1. Summary of different modes of 3D migration.

The migration of single cells in 3D is characterized by amoeboid and mesenchymal phenotype. Example cell types undergoing a particular mode of migration is displayed. Furthermore, the properties of the ECM or cell eliciting a particular mode of migration are also included. Reproduced from (8).

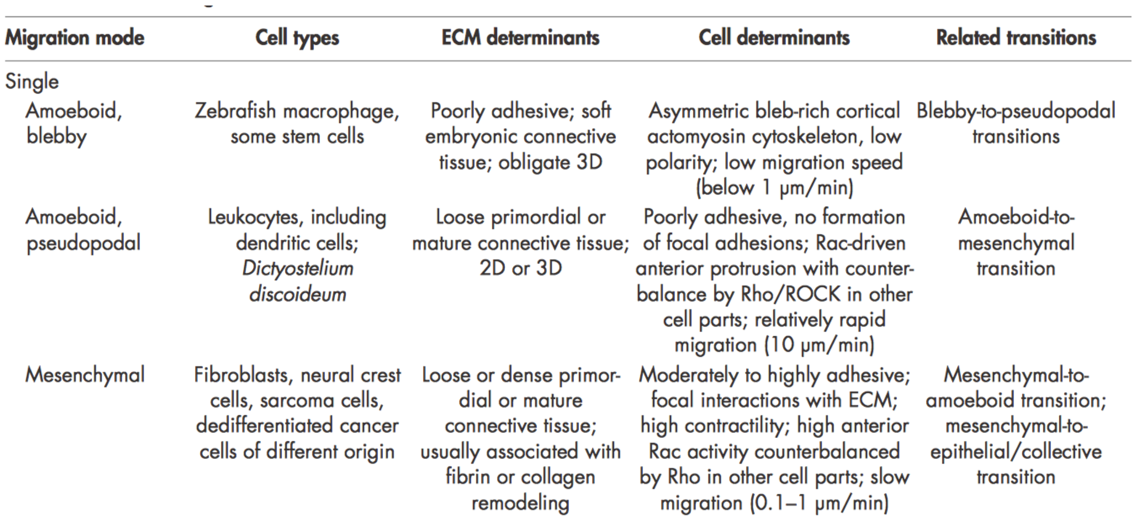

Migration mode	Cell types	ECM determinants	Cell determinants	Related transitions
Single				
Amoeboid, blebby	Zebrafish macrophage, some stem cells	Poorly adhesive; soft embryonic connective tissue; obligate 3D	Asymmetric bleb-rich cortical actomyosin cytoskeleton, low polarity; low migration speed (below 1 μm/min)	Blebby-to-pseudopodal transitions
Amoeboid, pseudopodal	Leukocytes, including dendritic cells; *Dictyostelium discoideum*	Loose primordial or mature connective tissue; 2D or 3D	Poorly adhesive, no formation of focal adhesions; Rac-driven anterior protrusion with counter-balance by Rho/ROCK in other cell parts; relatively rapid migration (10 μm/min)	Amoeboid-to-mesenchymal transition
Mesenchymal	Fibroblasts, neural crest cells, sarcoma cells, dedifferentiated cancer cells of different origin	Loose or dense primordial or mature connective tissue; usually associated with fibrin or collagen remodeling	Moderately to highly adhesive; focal interactions with ECM; high contractility; high anterior Rac activity counterbalanced by Rho in other cell parts; slow migration (0.1–1 μm/min)	Mesenchymal-to-amoeboid transition; mesenchymal-to-epithelial/collective transition

Table 1.2. Summary of chemokines secreted within the cancer microenvironment

The type of chemokine, the corresponding receptors, the cell type capable of secreting the chemokine, and the effect of the chemokine towards regulating cytotoxic T-cells (CTLs) are listed. Reproduced from (78).

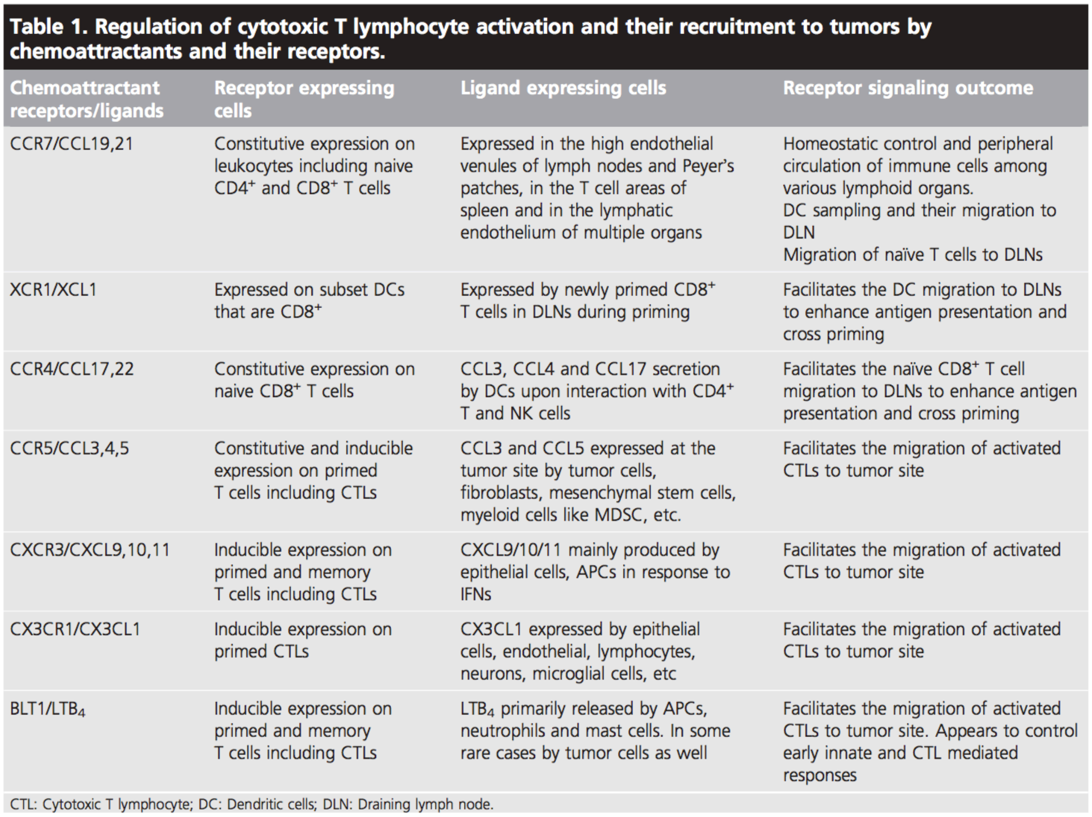

Table 1. Regulation of cytotoxic T lymphocyte activation and their recruitment to tumors by chemoattractants and their receptors.

Chemoattractant receptors/ligands	Receptor expressing cells	Ligand expressing cells	Receptor signaling outcome
CCR7/CCL19,21	Constitutive expression on leukocytes including naive $CD4^+$ and $CD8^+$ T cells	Expressed in the high endothelial venules of lymph nodes and Peyer's patches, in the T cell areas of spleen and in the lymphatic endothelium of multiple organs	Homeostatic control and peripheral circulation of immune cells among various lymphoid organs. DC sampling and their migration to DLN Migration of naïve T cells to DLNs
XCR1/XCL1	Expressed on subset DCs that are $CD8^+$	Expressed by newly primed $CD8^+$ T cells in DLNs during priming	Facilitates the DC migration to DLNs to enhance antigen presentation and cross priming
CCR4/CCL17,22	Constitutive expression on naive $CD8^+$ T cells	CCL3, CCL4 and CCL17 secretion by DCs upon interaction with $CD4^+$ T and NK cells	Facilitates the naïve $CD8^+$ T cell migration to DLNs to enhance antigen presentation and cross priming
CCR5/CCL3,4,5	Constitutive and inducible expression on primed T cells including CTLs	CCL3 and CCL5 expressed at the tumor site by tumor cells, fibroblasts, mesenchymal stem cells, myeloid cells like MDSC, etc.	Facilitates the migration of activated CTLs to tumor site
CXCR3/CXCL9,10,11	Inducible expression on primed and memory T cells including CTLs	CXCL9/10/11 mainly produced by epithelial cells, APCs in response to IFNs	Facilitates the migration of activated CTLs to tumor site
CX3CR1/CX3CL1	Inducible expression on primed CTLs	CX3CL1 expressed by epithelial cells, endothelial, lymphocytes, neurons, microglial cells, etc	Facilitates the migration of activated CTLs to tumor site
BLT1/LTB_4	Inducible expression on primed and memory T cells including CTLs	LTB_4 primarily released by APCs, neutrophils and mast cells. In some rare cases by tumor cells as well	Facilitates the migration of activated CTLs to tumor site. Appears to control early innate and CTL mediated responses

CTL: Cytotoxic T lymphocyte; DC: Dendritic cells; DLN: Draining lymph node.

Chapter 2: 3D Traction stresses activate protease-dependent invasion of cancer cells

2.1. Abstract

Cell invasion and migration such as in cancer metastasis is rooted in the ability of cells to navigate through varying levels of physical constraints exerted by the extracellular matrix (ECM). Cancer cells can invade into matrices either in a protease independent or dependent manner. An emerging critical component that influences the mode of cell invasion is traction stresses generated by the cells in response to the physico-structural properties of the ECM. In this study, we have developed a reference-free quantitative assay for measuring three-dimensional (3D) traction stresses generated by the cells during the initial stages of invasion into matrices exerting varying levels of mechanical resistance. Our results show that as cells encounter higher mechanical resistance, a larger fraction of them shift to protease-mediated invasion and this process begins at lower values of cell invasion depth. On the other hand, the compressive stress generated by the cells at the onset of protease-mediated invasion is found to be independent of "matrix stiffness", suggesting that 3D traction stresses are a key factor in triggering protease-mediated cancer cell invasion. At low 3D compressive traction stresses, cells utilize bleb formation to indent the matrix in a protease independent manner. However, at higher stress values, cells utilize invadopodia-like structures to mediate protease dependent invasion into the 3D matrix. The critical value of

compressive traction stress at the transition from protease independent to protease dependent mode of invasion is found to be approximately 165 Pa.

2.2. Introduction

Metastatic dissemination of cancer cells is a key contributor to more than 90% of cancer-inflicted mortality (83). Though metastasis involves multiple steps, the ability of cancer cells to break through the basement membrane and traverse through the ECM is a crucial manifestation of cancer malignancy. Recent studies suggest that cancer cells can invade into matrices either in a protease independent or dependent manner. An emerging critical component that influences the mode of cell invasion is the physical properties of the ECM, which includes porosity, alignment, and stiffness (12, 20, 25, 81, 84-90). For instance, cells encapsulated in a loosely crosslinked collagen network have been shown to migrate without the use of MMPs in a protease independent manner by adopting an amoeboid phenotype and employing actomyosin-generated forces to squeeze through the pores and channels of the ECM network (12, 25, 81, 84-86). Conversely, cells utilize protease-mediated degradation to navigate through dense ECM networks lacking such porous structures (20, 86-89, 91).

It is widely established that the mechanical properties of the tissue are drastically altered in the vicinity of solid tumors such as breast cancer as the disease progresses (92). The changes in mechanical and structural environment of the tumor have been shown to contribute to dissemination and enhanced migration of cancer cells. Results from Leventhal *et al.*, have demonstrated the prevalent effect of collagen crosslinking-mediated stiffening of the matrix on cancer cell dissemination (93, 94). The mechanical and structural changes of the environment could significantly affect the cellular traction force, which is a key regulator of migration, of the residing cancer cells (93). Chavrier and colleagues have shown that the contractility of the cell rear promotes migration and invasion of MDA-MB-231 cells in a Matrigel network (12). Similarly, studies have shown that contractile forces contribute to glycosylphosphatidylinositol-anchored Receptor CD24-facilitated cancer cell invasion (95). The increased invasiveness could also attributed to traction stress-mediated invadopodia formation (90). Studies have also reported significant differences in mechanical properties of the cells with their metastatic competence (96).

The aforementioned studies clearly demonstrate the pivotal role that the physical properties of the ECM play to promote invasion and migration of cancer cells. In this study, we quantify the interdependence between the initiation of cancer cell invasion into 3D matrices and the mechanical resistance to cell penetration opposed by the matrix. To this end, we developed a quantitative single cell invasion assay and determined the role of cell generated three-dimensional (3D) traction stresses on driving cancer cell invasion and protease activity using MDA-MB-231 cells as a model system.

2.3. Materials and Methods

2.3.1. Cell Culture

MBA-MD-231 (ATCC) cells were expanded in growth medium (GM) comprised of high glucose DMEM (Life Technologies), 10% fetal bovine serum (FBS, Hyclone), 2 mM L-glutamine (Life Technologies), and 50 units per ml of penicillin/streptomycin (Life Technologies). The cells were maintained at 37° C and 5 % CO_2.

2.3.2. Fabrication of Matrigel networks tethered to glass.

In order to tether the Matrigel networks, glass-bottom dishes (Fluorodishes, World Precision Instruments) were activated to react with amine groups of the Matrigel network. To activate the glass surfaces, 2.5 M NaOH was added for 30 minutes to remove impurities from the glass surface (97). The glass-bottom dishes were then rinsed with distilled water, dried, and reacted with 3-Aminopropyl-trimethoxysilane (Sigma-Aldrich) for 7 minutes. The treated dishes were then washed with distilled water, dried, and reacted with 0.5% glutraldehyde (Electron Microscopy Sciences) for 40 minutes. The activated surfaces were rinsed thoroughly and kept in distilled water for an additional 30 minutes. All of the above reactions were carried out at room temperature. The activated glass bottom dishes were used immediately.

The Matrigel networks were formed following manufacturer's instructions. Briefly, frozen Matrigel® (Cat. # 354234 & Lot # 30133, BD Biosciences) solutions were thawed overnight on ice at 4° C. Fluorescent particles with a nominal diameter of 200 nm (Fluospheres, Life Technologies; max excitation at 660 nm and max emission at 680 nm) were dispersed in the Matrigel solution to achieve a final concentration of 2% (v/v). After mixing thoroughly, 18.75 μL of the solution was quickly transferred to the activated glass-bottom dish and spread over a circular region of approximately 15 mm in diameter. The solution was then spun using a Spin Coater KW-4A (Chemat Scientific) at room temperature for 1 minute at RPMs of 600, 800, 1100, and 1300 to thin the Matrigel solution to create networks with different thicknesses (T) of 30, 20, 10, and 6 ± 2.5 μm, respectively, without altering the concentration. The spun Matrigels were incubated at 37° C for 6 minutes to complete gelation before the addition of phosphate buffer solution (PBS). After 15 minutes of incubation in PBS, the Matrigel was UV-sterilized for 30 minutes before replacing the PBS with GM. The thicknesses of the equilibrated Matrigels were determined using a spinning disk confocal microscope (Perkin Elmer UltraView Vox Spinning Disk Confocal). The difference in the vertical position at which the fluorescent beads were in focus at the top and bottom of the gel was designated as the thickness of the gel. Both the surface and the bottom of the Matrigels were imaged at multiple locations to determine the gel thickness. Figure 2.1 shows the X-Y and X-Z cross sectional images of Matrigel networks with varying thicknesses. The dishes were then incubated in medium at 37° C and 5% CO_2 overnight prior to cell seeding.

2.3.3. Cell invasion and imaging

The invasion of MDA-MB-231 cells into the Matrigel network was determined by using a quantitative single-cell invasion assay. MDA-MB-231 cells were plated onto the Matrigel networks tethered to the glass-bottom dishes at a density of 6,000 cells/cm^2 in GM with serum or OptiMEM (OM) for serum-free conditions. The cells were allowed to invade into the Matrigel for 1, 2, and 4 hours. Individual cells were imaged and their corresponding stage positions were marked. For each location, a DIC image of the cell and fluorescence image stacks of the matrix embedded with fluorescent particles were acquired. The z-slice spacing was set as 200 nm and the z-range was chosen to encompass 3 μm above the surface of the Matrigel to 3 μm below the maximum penetration depth of the cells. Previously marked stage positions were re-imaged after the removal of the invaded cells. A total of $n > 160$ cells were used and analyzed.

2.3.4. Removal of cells after cell invasion

The invading cells were removed using a cell-dissolving solution as described elsewhere (98). The cell dissolving solution was made by mixing NH_4OH and Triton X-100 in PBS to achieve a final solution containing 20 mM NH_4OH and 3% w/v Triton X-100. To remove the cells, 1 mL of the culture medium was removed from the 2 mL total volume before adding 0.5 mL of the cell dissolving solution. To this, 2 mL of PBS was added before removing 3 mL of the above mixture followed by an addition of 2 more mL of PBS. The continuous washing with PBS was used to neutralize the drastic changes in pH due to the cell dissolving solution (Fig. 2.2A). The effect of the cell removal process on swelling and/or shrinking of the Matrigel network was determined as described in SI Text (Fig. 2.2B-E). The removal of cells was also confirmed through bright field images and staining for F-actin. (Fig. 2.3).

2.3.5. Mechanical Yielding Tests of Matrigel Networks

Glass-bottom dishes with grid markings were generated by attaching Cellattice sheets (Electron Microscopy Sciences) underneath the dishes using an optical adhesive. The glass surface within the dish was activated and the Matrigel networks embedded with fluorescent beads were synthesized as described above. Specific locations of the Matrigel network and the lattice grids were imaged at 60x magnification by using a water immersion lens mounted onto a spinning disk Confocal. 10-μm thick image stacks of the network with embedded fluorescent beads were obtained at vertical increments of 0.2 μm. A schematic of the experimental procedure to measure the mechanical yielding of the matrix is outlined in Fig. 2.4. The tips of cantilevers with a spring constant of 0.5 N/m were modified by attaching 30 μm diameter glass beads. These modified tips were mounted onto the BAFM and used to indent the Matrigel at the imaged locations. One set of deflection threshold was used to indent 5 different locations before increasing the threshold to apply larger forces. The deflection threshold ranged from 10 to 70 nm while ramp sizes for all indentations were set at 1.872 μm. The indentation depth, defined as the difference between the cantilever deflection and the z ramp displacement obtained from the force curves, was used to calculate the maximum applied compressive pressure using the Hertzian model corrected for finite substrate thickness (99). These locations were then re-imaged using the spinning disk confocal microscope as mentioned above. The image stacks obtained before and after the BAFM indentation were processed to account for rotational and translation shifts using custom MATLAB software. Specifically, maximum cross correlation between the pre-indentation images and the rotated post-indentation images was determined to correct for the rotational and translational shifts. The displacement field was obtained from corrected image stacks using 3D image correlation algorithms described elsewhere (100).

2.3.6. MT1-MMP FRET Analysis

Cells were plated into 24-well plates, cultured in GM, and allowed to reach 80 % confluence before transfection. The cells were transfected with MT1-MMP FRET biosensor plasmid using Fugene HD Transfection Reagent (Promega) two days prior to the experiments. For transfection, each well containing the cells was exposed to 1.7 μL of Fugene transfection reagent mixed with 25 μL of OM (Life Technologies) containing 1.1 μg of the DNA plasmid. Prior to plating the cells, 50 μg/ml of fibronectin (Sigma) diluted in PBS was coated onto glass surfaces or 30 μm thick Matrigels for 1.5 hours at 37 ºC. Untreated cells or cells treated overnight with the MMP inhibitor GM6001 (50 μM) were plated on either glass or Matrigel surfaces. Images were collected 4 hours post-plating using a Zeiss Axiovert inverted microscope equipped with 100x objective (1.4 NA) and a cooled charge-coupled device camera (Cascade 512B; Photometrics) using the MetaFluor 6.2 software (Universal Imaging). The parameters of dichroic mirrors, excitation and emission filters for different fluorescence proteins were described previously (101). In brief, the MT1-MMP biosensor was excited at 420 ± 20 nm, and the emissions were collected at 475 ± 40 nm or 535 ± 25 nm for ECFP or FRET images, respectively. The quantification of ECFP/FRET ratio signal was performed using our MATLAB-based software *fluocell* (102, 103). Higher FRET ratio indicates increased activity and/or presence of MT1-MMP on the cell surface.

2.3.7. Zymography and fluorogenic peptide assay

Secreted Protease Activity Detection Using Zymography

To obtain ~ 30 μm thick gels, 7 μL of the thawed Matrigel solution was added into each well of a 24-well plate. The Matrigel solution was spread across the well using a pipette at 4° C and left for 10 minutes before transferring to 37° C for 30 minutes. PBS was added to the wells containing Matrigel networks and the entire plate was sterilized by exposing to UV for 30 minutes. The PBS was replaced with OM and incubated overnight at 37^{o}C before plating the cells. The OM was removed and the cells were plated at a density of 10,000 cells/cm^2 in 650 μL OM for each well, and cell invasion into Matrigel was allowed to persist for 6 hours resulting in a ϕ_{3D} >20° (Fig. 2.5A). 600 μL of the collected OM was centrifuged to remove non-adhered cells at 1,000 RPM for 10 minutes. 500 μL of this solution was concentrated for secreted factors by using centrifugal filter tubes with a molecular weight cutoff of 50 kDa (Microcon) as instructed by the manufacturer's protocol. Conditioned medium from 8 wells were collected to obtain a concentrated solution of ~ 30 μL.

The concentrated conditioned medium was assayed for protease activity as described elsewhere (104). Briefly, we used a stacking gel comprised of 3.68 % acrylamide and 0.01 % bisacrylamide and a resolving gel comprised of 7.5 % acrylamide gel, 0.33 % bisacrylamide, and 0.08% gelatin. After the gels were polymerized, cathode and anode reservoir buffers were added to the outer and inner chamber of an upright electrophoresis apparatus, respectively. The cathode buffer consisted of 10.25 mM ammediol, 10 mM glycine, and 0.1 % SDS adjusted to pH of 9.39 while anode buffer consisted of 21 mM ammediol adjusted to pH of 8.23. The gel lanes consisted of a positive control, a negative control, concentrated conditioned medium, activated concentrated conditioned medium, and control for activated concentrated conditioned medium. The positive and negative controls consisted of 0.1 μg of Bovine Collagenase IV (Gibco) and OM concentrated from 8 wells containing acellular Matrigels, respectively. To activate the concentrated conditioned medium, the medium was incubated in 1 mM 4-Aminophenylmercuric Acetate (APMA, Sigma-Aldrich) dissolved in 80 mM NaOH for 2 hours in 37°C prior to loading the samples. The control for the activated and concentrated conditioned medium was generated by incubating the medium in 80mM NaOH without APMA. 16 μL of each solution was loaded into their respective lanes and gel electrophoresis was run for 1.5 hours using a voltage of 150 V. After electrophoresis, the proteins in each lane were renatured by submerging the gel in a developing buffer mixed with 2.5 % Triton-X 100 for one hour with frequent washing before incubating the gels in developing buffer overnight at 37 °C. The developing buffer used consisted of 50 mM Tris base, 200 mM NaCl, 5.2 μM $ZnCl_2$, 5 mM $CaCl_2{\cdot}2H_2O$, and 3 mM NaN_3. After the overnight incubation, the gel was stained for 30 minutes in 0.125 % Coomassie brilliant blue R-250 dissolved in a mixture of methanol, acetic acid, and water at volume ratios of 1.25:0.5:0.75. The gel was subsequently destained in a solution comprised of methanol, water, and formic acid at a volume ratio of 1.5:3.5:0.05. The gel was destained until the desired contrast between the light bands devoid of gelatin due to protease-mediated degradation and the surrounding gelatin was achieved. The gel was frequently imaged to document the contrast.

The presence of bands in the lane consisting of concentrated conditioned medium indicates that secreted proteases were present within the medium. The finding that the bands did not shift when compared to the lane consisting of medium treated with APMA further reveals that the secreted proteases were in the active form (Fig. 2.5B).

Secreted Protease Activity Detection Using Fluorogenic Peptides

Matrigels were synthesized in 24-well plates as previously mentioned. Cells were plated onto the Matrigel-containing wells at a density of 6,000 cells/cm^2 with a total volume of 500 μL. Acellular Matrigel cultured in GM under identical culture conditions was used as a negative control (NC). The cells were allowed to invade into the Matrigel for 3 hours ($\phi_{3D} > 15°$) before collecting 200 μL of the media from each well. For each well, the collected media was centrifuged to remove any suspended cells. 98 μL of the collected media was then mixed with 2 μL of 0.5 mM stock solution of MMP sensitive fluorogenic peptide substrate (Cat # ES001 & Lot # DHY08, R&D Systems). This approach was used to circumvent the interference from Matrigel during the measurements from the plate reader. For the positive control, 0.1 μg of Bovine Collagenase IV solubilized in 98 μL of PBS was mixed with 2 μL of the peptide substrate stock. The mixtures were transferred to a 96 well plate and allowed to incubate for 15 minutes at 37° C. The fluorescence caused by MMP cleavage was determined using a plate reader (Infinite 200 Pro, Tecan) at excitation and emission wavelengths of 320 ± 4.5 and 405 ± 10 nm, respectively. The higher fluorescence value for conditioned medium from invading MDA-MB-231 cells compared to NC indicates higher protease activity associated with the invasion of MDA-MB-231 cells (Fig. 2.6).

2.3.8. Immunofluorescence Staining and Imaging

MDA-MB-231 cells were plated onto Matrigel at a seeding density of 6,000 cells/cm^2 and allowed to invade the matrix for over 2 hours. To stain cells generating steep indentations ($\phi_{3D} > 10°$), Matrigels with the invading cells were fixed in 4% paraformaldehyde for 10 minutes, washed in PBS, and incubated in a blocking buffer containing 3% bovine serum albumin and 0.25% triton X-100 in PBS for 30 minutes. The fixed cells were incubated with primary antibodies such as Alexa Fluor 488-conjugated Phalloidin (Life Technologies), anti-Cortactin p80/85 antibody (Millipore), and/or anti-MT1-MMP (Abcam, Cat. Ab38970) diluted 1:100 in the blocking buffer for 1 hour at room temperature. The samples were washed extensively in PBS before adding Alexa Fluor 568-conjugated secondary antibody diluted (1:250) in the blocking buffer for 1 hour. The samples were washed in PBS and were imaged immediately.

For cells generating flat indentations ($\phi_{3D} < 10°$), glutaraldehyde (GA)-mediated fixing of the cells was found to provide the best results. The cells were plated at a density of 20,000 cells/cm^2 and were allowed to invade for 15 minutes before fixing with 0.1% w/v GA in PBS for 1 minute. The higher cell density was used to ensure enough cells have invaded into the matrix during the short time span. The samples were subsequently washed in PBS and permeabilized with blocking buffer for 30 minutes. After removing the blocking buffer, the GA-treated samples were incubated in 0.1% w/v sodium borohydride in PBS to neutralize unreacted aldehyde moieties for 30 minutes to quench the autofluoresence. Sodium borohydride was subsequently removed and the samples were washed in PBS before incubating with primary and secondary antibodies.

All experiments were carried our independently at least thrice, beyond the replicates used in each experiments.

2.3.9. Quantitative Cell Invasion assay

We have developed a quantitative single cell invasion assay that can quantify the traction stresses and the accompanying matrix deformations while the cancer cells migrate into the matrix. The cell invasion assay utilized an ECM network, Matrigel, tethered onto glass and embedded with fluorescent particles to track the progressive matrix deformation as MDA-MB-231 cells invade into the matrix as single cells (Fig. 2.7) (see Fig. 2.8 for characterization of the Matrigel networks). We chose Matrigel because of its tight microstructure of the network (mesh size ≤ 20 nm); the absence of large network pores and channels will eliminate the possibility of cells squeezing through the network (105, 106).

2.3.10. Quantification of the matrix indentation profile caused by the invading cells from confocal images

MDA-MB-231 cells were allowed to invade the Matrigel network and imaged using a confocal microscope to detect the accompanying matrix deformation. The image stacks corresponding the cell invasion were analyzed using a custom MATLAB code to quantify the matrix indentation depth caused by the cells $H_i(x,y)$, the maximum indentation depth caused by the cells, $h_{w/\,cell}$, the indentation depth after the cell removal, $h_{w/o\,cell}$, and the radius of indentation, R (Fig. 2.9). First, each z-slice of the stacks was normalized with the average image intensity of the whole z-stack. A Sobel edge detection filter was applied to each slice in the stack to detect and count the number of in-focus pixels as a function of z (blue line in Fig. 2.9). The slice with the maximum z-change of in-focus pixels is set as the top surface of the matrix and used as reference to obtain the indentation profile, $h_{w/\,cell}$, $h_{w/o\,cell}$, and R. For each image slice, we calculated the in-plane Euclidean distance transform, which yielded the minimum distance to an in-focus pixel in that z-slice. Because cell indentation pushed the beads downwards and out of focus (see inset in Fig. 2.7A), the maximum value of the Euclidean distance in the whole z-stack was defined as R (green circles in Fig. 2.9). On the other hand, the z-slice at which the Euclidean distance reached its floor was designated as the bottom of the cell. The z-distance between the top and bottom slices provided $h_{w/\,cell}$. After cell removal, the previously marked positions of the cells (*i.e.,* before their removal) were reimaged to determine $h_{w/o\,cell}$.

The quantities $h_{w/\,\mathrm{cell}}$ and $h_{w/o\,cell}$, provides unique information about the nature of matrix deformation due to cell invasion — elastic vs. permanent. The extent of permanent matrix deformation caused by the invading cells was quantified by the ratio of maximum indentation depths before and after removing the cells, $\gamma = h_{w/o\,cell} / h_{w/\,cell}$. A zero-value for γ indicates elastic recovery, while $\gamma \neq 0$ suggests permanent deformation of the matrix due to structural changes during cell invasion. The deformation of the matrix was further quantified by using the angle of 3D indentation calculated as $\phi_{\mathrm{3D}} = tan^{-1}(h_{w/\,cell} / R)$, where R is the radius of matrix deformation (Fig. 2.7A). The angle ϕ_{3D} quantifies whether the matrix deformation created by the cell is flat ($\phi_{\mathrm{3D}} \approx 0$) or steep ($\phi_{\mathrm{3D}} \approx 90^{\circ}$).

Representative indentation profiles of the Matrigel network with varying thicknesses during cell invasion are shown in Fig. 2.7B.

To eliminate the interference of post-plating time on degree of permanent deformation of the matrix, we have determined $\phi_{3\text{D}}$ values for different post-plating times (1, 2, 4 hours). Our results indicated that a subset of cells imaged during different post plating times attain similar $\phi_{3\text{D}}$ values. Therefore, to rule out the possibility of these cells exhibiting different extent of matrix degradation as a function of time, the γ values for cells at similar ϕ_{3D} values but different plating times were plotted (Fig. 2.10). The effect of time on the degree of permanent deformation was negligible since the gamma values for cells analyzed at different post-plating times were statistically insignificant.

2.3.11. Calculation of 3D Traction Stresses During Cell Invasion

To calculate 3D traction stresses such as those shown in Figure 2.7D, we acquired time-lapse image z-stacks of cells invading into the Matrigel. The cells were removed before the matrix was permanently deformed to determine the stresses generated by the cells by using 3D Fourier Traction Force Microscopy (3DTFM) methods that have been fully detailed elsewhere (107, 108). The lack of degradation of the Matrigel was experimentally confirmed by the lack of vertical surface indentation after cell removal. The corresponding images of the un-deformed matrix were used as a reference state to obtain the matrix 3D deformation of each z-stack by image correlation. Imposing these measurements as boundary conditions and zero displacements at the bottom of the matrix tethered to glass, we obtained the exact analytical solution to the equation of elastic equilibrium for a homogeneous and isotropic 3D body:

$$\nabla(\nabla \cdot \vec{u}) + (1 - 2\sigma)\nabla^2 \vec{u} = 0. \qquad [1]$$

The solution to this equation provided the full 3-D strain tensor in the whole Matrigel network, which was plugged into Hooke's law to calculate the traction stresses. An important feature of this solution is that it takes into account the finite thickness of the gel (107, 108). The Poisson's ratio of the Matrigel network was approximated to be 0.495 while the elastic modulus was measured to be 400 Pa.

2.3.12. Reference-free Estimation of Normal Traction Stresses During Cell Invasion

Standard 3D TFM methods, such as the one used to plot Figure 2.7D, require imaging the network in an undeformed condition to use it as zero-stress reference (28, 107, 109-111). This can be achieved by either tracking single particles or, as done in our study, by applying image correlation techniques (112, 113). However, if cells switch from protease independent to protease dependent invasion, the network may experience permanent remodeling and it may not be in an undeformed reference condition after cell removal. This also imposes stringent experimental requirements that an unperturbed zero-stress reference state needs to be imaged for each cell prior to the invasion process. To circumvent these limitations and to determine the threshold traction stress at which the invading cells switch from a protease independent to a dependent mode, we developed a novel reference-free method that does not require imaging the undeformed condition to measure the compressive traction stresses generated by the cells. This method models the measured indentation profiles generated by the invading cells as

$$H(x,y) = h_{w/\,cell}\left(\frac{r^6}{6\lambda^6} - 1\right)e^{-\frac{r^2}{\lambda^2}}, \qquad [2]$$

where $r = \sqrt{x^2 + y^2}$ is the distance to the indentation center. The parameters $h_{w/\,cell}$ and R were determined experimentally, and $\lambda = 0.74R$ was fixed by imposing $w(R) = 0$. The functional dependence of this model profile was chosen to conform to the following experimental observations and physical considerations: 1) the vertical deformation caused by the cell is negative (i.e. downward) under the cell center and positive around the cell periphery (Fig. 2.7); 2) the vertical deformation decays to zero away from the cell periphery; and 3) the cell is in mechanical equilibrium. The model is plotted in Fig. 2.7B together with measurements of matrix deformation in the normal direction for several cells showing good agreement with experimental data regardless of matrix thickness.

For each cell, the normal traction stresses were computed using Eq. 2 for the normal deformation profile and zero tangential deformation in the 3DTFM equations (107). Particularly, we focused on the maximum negative value of the normal traction stresses,$\tau_{zz}(0)$, which is found at the lowest point of the indentation, because this value indicates the pushing force exerted by the cell to penetrate into the matrix. Figure 2.7C compares the value of $\tau_{zz}(0)$ obtained with this reference-free method with the value obtained using the full 3DTFM method of del Alamo *et al.* for a small group of cells to which both methods were applied (107). The results show good agreement between the two methods, although the reference-free method slightly underestimates $\tau_{zz}(0)$ (mean error = 11 %) due to the averaging involved in the fitting procedure used to obtain $h_{w/\,cell}$

and *R*. This approach is further justified because the normal traction stresses are much higher than the tangential ones for the invading cells, and the tangential stresses are zero under the central region of the cell where the normal stresses are maximal (Figure 2.7D). This reference free approach facilitates high-throughput and quantitative analyses of individual cells with varying indentation profiles. Our calculation of normal stresses is flexible regarding the shape of *H(x,y),* which could be easily replaced by any other profile. It should be noted that a Hertz model could not be used for this purpose as the cells not only pushed into the matrix but also pulled away from it (Fig. 2.7B) to satisfy the mechanical equilibrium condition.

2.3.13. Estimation of Apparent Young Modulus Encountered by the Invading Cells

Because the Matrigel networks are anchored to the underlying glass, which is significantly stiffer compared to the Matrigel network, and because compressive traction stresses penetrate deep into the gel (Fig. 2.7D), the apparent Young's modulus encountered by the cells has been shown to increase as the thickness of the matrix decreases to a value comparable to cell size (107). To quantify the apparent Young's modulus (E_{app}) encountered by each invading cell, we multiplied the nominal Young's modulus of the Matrigel (E = 400 Pa) with the ratio of the measured normal traction stresses considering the finite thickness of the matrix to the stresses calculated for a matrix of infinite thickness (107):

$$E_{app} = E\frac{\tau_{zz}(h)}{\tau_{zz}(\infty)}$$

2.3.14. Characterization Of Matrigel Networks

Prior to characterization, the Matrigels were incubated overnight in growth medium (GM) at 37° C and 5% CO_2. Surface topography of Matrigels of T = 30 and 10 μm tethered to a glass-bottom culture dish was obtained in GM using a Bioscope Atomic Force Microscope (BAFM) equipped with a Nanoscope IIIA controller (Bruker). The topographical images were obtained in contact mode by using Si_3N_4 cantilevers with 0.02 N/m nominal spring constants at forces of ~ 4 nN over areas of 10×10 μm^2. The surface roughness values were determined using the Nanoscope software and the images were processed with a flattening order of 2 to account for tilts during the measurements. The measurements show similar roughness and topography for the Matrigel networks of 10 and 30 μm thickness (Fig. 2.8A, B).

2.4. Results and discussion

2.4.1. Invasion of MDA-MB-231 cells into Matrigel networks

By employing the quantitative cell invasion assay, we have determined the invasion of MDA-MB-231 cells into a Matrigel networks of 30 μm thickness tethered onto glass. The 3DTFM analyses of the invading cells suggest that to invade downward into Matrigel, the cells pulled away from the matrix at several locations along the cell periphery, while pushing against the matrix under its center (see Fig. 2.7D). Because all forces must be in equilibrium as cell inertia is negligible, this lead to a significant amplification of the pushing stresses (by over a factor of 3 as in Fig. 2.7D), a mechanism that we have named *"stress focusing"*. These normal traction stresses (τ_{zz}) were also found to be much higher than the tangential ones ($\sqrt{\tau_{zx}{}^2 + \tau_{zy}{}^2}$), suggesting that the invading cells were actively burrowing through the matrix using mechanical forces. Because pushing traction forces penetrate much deeper into the matrix than pulling and shearing traction stresses, it could be possible that cells utilize this type of force to sense the mechanical resistance exerted by the matrix (Fig. 2.7D).

The cell invasion analyses demonstrate that as the cells invaded deeper into a 30 μm thick matrix, they created steeper matrix deformations leading to an increase in ϕ_{3D} and $h_{w/cell}$ (Fig. 2.11A). The cells exerting these large deformations ($\phi_{3D} \geq 20^o$ and $h_{w/cell} > 5\ \mu m$) resulted in permanent matrix deformations (Fig. 2.11B). On the contrary, for small deformations ($\phi_{3D} \leq 10^o$ and $h_{w/\,cell} \sim 2\ \mu m$), the cells deformed the matrix elastically and the Matrigel recovered its undeformed state after cell removal. Permanent deformation due to pure mechanical yielding of the matrix in response to cellular traction stresses was ruled out because the Matrigel did not undergo permanent deformation when subjected to pure mechanical loads > 200 Pa — a value higher than the maximum traction stress measured at the transition from elastic to permanent matrix deformation (Figs. 2.4 and 2.12) (114). Thus the permanent deformations observed during cell invasion for large matrix indentations were due to proteolytic degradation of the Matrigel network.

This transition from elastic to permanent matrix deformation as the cells invade deeper into the matrix suggests a switch from a protease-independent to a protease-dependent mode of invasion. To further understand the cellular responses associated with different modes of invasion, we examined the changes in F-actin and MT1-MMP, a key

MMP involved in MDA-MB-231 invasion (84, 115), for the population of cells that elastically and permanently deformed the 30 μm thick matrix. Immunofluorescent staining for F-actin revealed plasma membrane blebbing, which preceded the invasion of cells into the Matrigel and persisted until a ϕ_{3D} of ~ 15^o and $h_{w/cell}$ of ~ 3 μm was reached. The majority of these blebs were found at the leading edge, whereas the MT1-MMPs were clustered within the cytoplasm (Figs. 2.11 C, D). The absence of MT1-MMP on the cell periphery for such small matrix deformations was confirmed by low levels of MT1-MMP FRET signal, which were comparable to cells treated with broad-spectrum MMP inhibitor, GM6001 (Fig. 2.6A left and center panel, 2.6B). The matrix-mediated bleb formation was also observed in cultures containing no serum, thus eliminating the contribution of serum components on this phenomenon (Fig. 2.13).

Conversely, for large matrix deformations ($\phi_{3D} > 20^o$ and $h_{w/cell} > 4$ μm), blebbing was no longer observed and the MT1-MMP was re-localized from the cytoplasm to the plasma membrane. These cells with round morphology exhibited invadopodia like protrusions enriched with actin fibers, cortactin, and MT1-MMP at the leading edge (Fig. 2.11E, F) (116-119). Although cortactin was located all along the protruded structures, MTI-MMP was located at the base of the invadopodia in discrete locations. At the onset of permanent matrix deformation, the invading cells showed the coexistence of bleb and invadopodia-like structures (Fig. 2.14). A recent study by Bergert *et al*. has shown that migrating cells exhibit bleb to lamellipodia transition in response to changes in actomyosin contractility (120). Giri *et al*. reported the usage of dendritic protrusions by the cells to deform the surrounding matrix (121). The re-localization of MTI-MMP to the cell membrane and MT1-MMP activation with large matrix deformation was further confirmed by FRET analyses using these MT1-MMP biosensors (Figs. 2.6A, B) (122). We also observed the presence of secreted MMPs and their activity by zymography and by monitoring the cleavage of MMP sensitive fluorogenic peptides (Fig. 2.5 and 2.6C).

2.4.2. Effect of mechanical resistance on invasion of MDA-MB-231 cells

In order to decouple the role of traction stresses on triggering protease activity from other parameters, such as steepness and depth of the matrix indentation, we examined the invasion of MDA-MB-231 cells into Matrigel networks that exert varying levels of mechanical resistance while keeping the network composition and interfacial properties constant. Matrigel networks with similar interfacial properties but varying "effective rigidity" were created by adjusting the overall thickness of the gels to approximately T = 10, 20, and 30 ± 2.5 mm. This quantitative approach allows a unique opportunity to vary the mechanical resistance in a controlled manner without altering the network composition and matrix surface properties across the experiments and thus eliminating the effect of matrix interfacial properties on cell functions (123, 124).

As the thickness of the gels decreased, the apparent Young's modulus encountered by the cells increased and a higher fraction of cells deformed the matrix permanently (Fig. 2.15A, first and second panels). Cells on thinner gels elicited permanent matrix deformation at smaller matrix deformations and shallower indentation angles (Fig. 2.15A, third and fourth panels), suggesting that neither $h_{w/cell}$ nor ϕ_{3D} were decisive factors in triggering proteolytic ECM degradation. The critical values of $h_{w/cell}$, ϕ_{3D}, and normal traction stress at the transition between protease-independent and protease-dependent invasion were determined averaging data from cells with $0.05 < \gamma < 0.2$, which had barely degraded the ECM. Contrary to $h_{w/cell}$ and ϕ_{3D}, the critical value of normal traction stresses (i.e., the pushing traction forces) at the transition between elastic and permanent matrix deformation, $|\tau_{zz,}(0)|_{crit}$, was found to be independent of gel thickness and around 165 ± 20 Pa (right panel of Figs. 2.15A and 2.16). Because the normal traction stresses were calculated assuming elastic deformation ($\gamma = 0$), our prediction of $\tau_{zz,\ crit}$, could possibly overestimate the true traction stresses at the onset of proteolytic matrix degradation. Nevertheless, it should be noted that the small error associated to this approach (5%-20%) is lower than the statistical noise in the measurements (the standard deviation in the plot is ≈ 33% of the mean), and it does not introduce a bias when considering different matrix thickness.

We also examined the transition from bleb to invadopodia for cells invading into a thinner Matrigel exhibiting very small matrix deformations. Similar to the 30 μm thick matrix, bleb formation was observed before any substantial deformation of the matrix was detected while MT1-MMPs remained within the cytoplasm (Fig. 2.15B). As cells continued the invasion process, blebbing was deflected along the cell-matrix interface while MT1-MMP still remained in the cytoplasm (Fig. 2.15C). This suggests that the blebs were unable to push forward in the normal direction, where they encountered a higher mechanical resistance due to the influence of the glass at the bottom of the gel. As the cells spread further on the Matrigel surface, the blebbing disappeared, actin stress fibers formed at the basal domain of the cells, and invadopodia-like protrusions were localized with cortactin and MTI-MMP (Figs. 2.15D, E). These findings further confirm that invadopodia enriched with MT1-MMP form at low matrix deformation when the mechanical resistance is increased.

Together, these findings identify traction stresses as a key determinant in triggering protease-dependent cancer cell invasion into 3D matrices. This is in accordance with recent studies implicating the potential role of mechanical forces on extracellular proteolysis (20, 90, 91, 125). Although other extracellular matrix properties such as pore size and fibrillar structure(s) were not addressed, the findings from this study can be easily extended to unravel the effect of these ECM properties on cancer cell invasion. The physical characteristics of ECM provide different levels of mechanical resistance and thereby cell generated traction stresses to trigger protease-mediated invasion and migration. For instance, networks with large pores allows cells to migrate through the matrix with minimal resistance thus the cells would be in a state below the threshold of traction forces (86). On the other hand, the alignment of the fibrillar structure of the ECM mediated by the cells increases the mechanical tension in the extracellular network and promotes proteolysis (20). Furthermore, the anisotropic alignment of 3D cellular traction stresses has been correlated with cancer cell invasiveness (28). The interplay between traction stresses and ECM remodeling could also vary dynamically, as the cell could adapt its protease-dependent invasive phenotype to the time evolving resistance resulting from matrix degradation. Future developments of quantitative force microscopy assays that consider inhomogeneity and anisotropy of the ECM, and its time evolving material properties, will provide further insight into the interplay between traction stresses and protease-dependent cancer cell invasion into 3D matrices.

2.5. Conclusion

In summary, the results reported here demonstrate the role of 3D traction stresses on regulating the mode with which cancer cells invade the ECM networks to contribute to cancer metastasis. We showed that invading cells pull away from the matrix at several locations while they compress the matrix at only one site, thus enabling a *"stress focusing"* mechanism that amplifies the compressive load applied to the matrix and conceivably promote invasion. At low compressive stresses, the cells indent the matrix in a protease independent manner by using bleb formation. However, at compressive traction stresses higher than ~165 Pa, the cells invade in a protease dependent manner as they utilize invadopodia like structures where MT1-MMP activity on the cell surface is high. Identification of such quantitative approaches could not only advance our understanding of cell mechanics-ECM proteolysis interdependency on dissemination of cancer buy could also shed light onto new pathways that could be targeted to develop new therapies to treat cancer metastasis.

2.6. Acknowledgements

The authors gratefully acknowledge Jennifer Santini for assistance with microscope and image analyses, Susan C. Lin and Jay A. Shankar for assistance with experiments, and the UCSD Neuroscience Microscopy Shared Facility (P30 NS047101). A.A. acknowledges ARCS fellowship, S.V. acknowledges CRCC research award, and J.C.d.A. acknowledges funding from NIH (5R01GM084227-03).

Chapter 2, in full, is a reprint of the material as it appears in Biophysical Journal, vol. 107, 2014. "3D Traction stresses activate protease-dependent invasion of cancer

cells”. Aung, Aereas; Seo, Young N.; Lu, Shaoying; Wang, Yingxiao; Jamora, Colin; del Alamo, Juan Carlos; Varghese, Shyni. The dissertation author was the primary investigator and author of this paper.

2.7. Figures

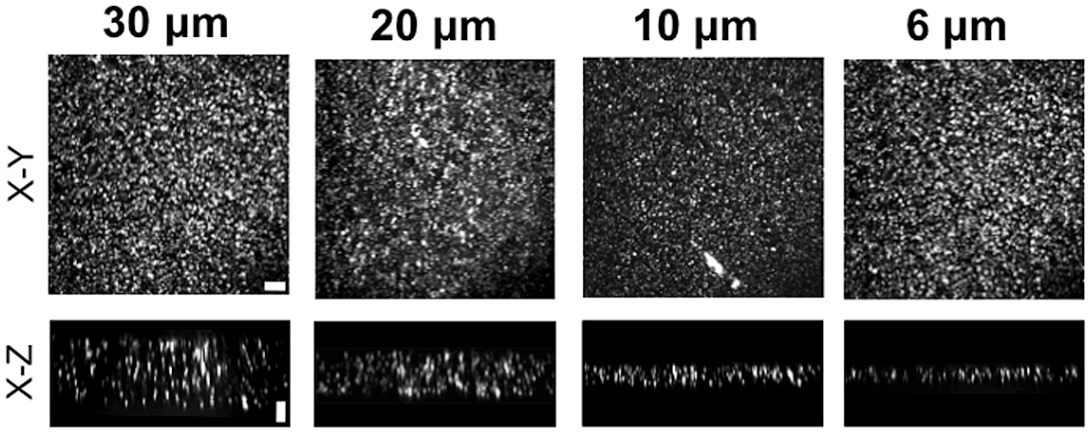

Figure 2.1: Verification of Matrigel network thickness.

X-Y and X-Z planes of Matrigel networks created with varying thickness and tethered to glass obtained via confocal imaging. Horizontal and vertical scale bars represent 10 µm.

A

[NH_4OH]	pH
5 mM	8.4
10 mM	9.6
20 mM	10.1

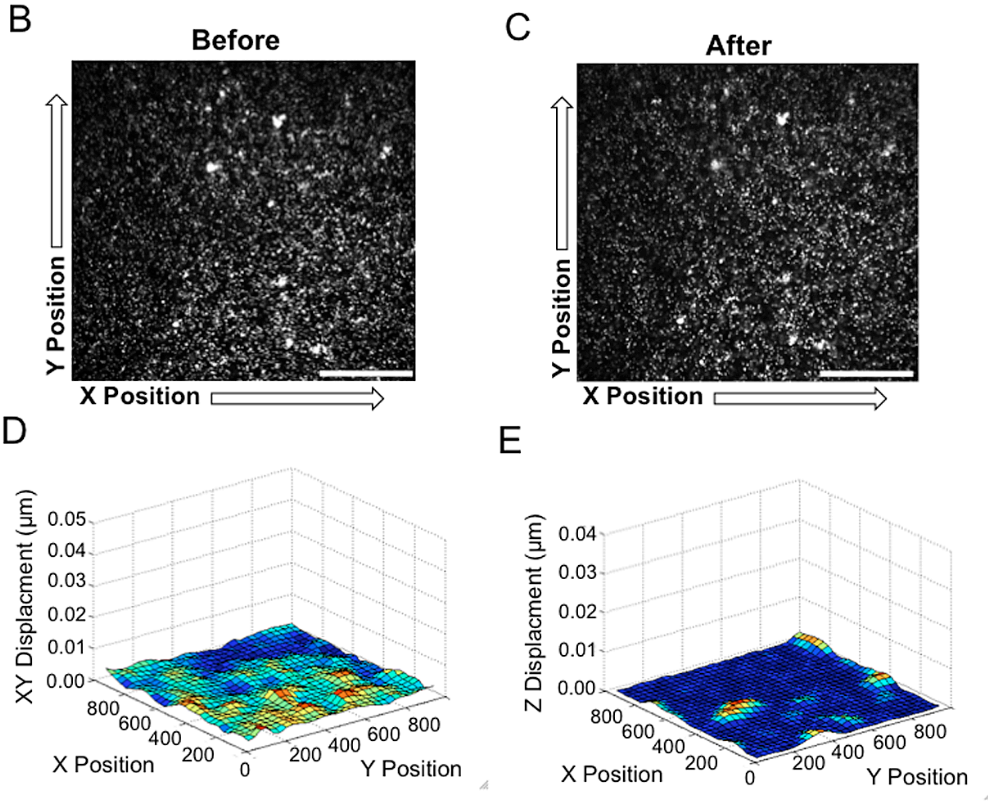

Figure 2.2: Effect of cell dissolving solution on the Matrigel network.

(A) Table shows the pH of the cell dissolving solution containing 3% Triton-X 100 with increasing concentration of NH_4OH. Confocal images of the surface of the Matrigel network embedded with fluorescent beads (B) before and (C) after the treatment with the dissolving solution comprised of 20 mM NH_4OH and 3% Triton-X 100. The tangential (D) and the vertical (E) displacement fields obtained by image correlation analysis show that the effect of dissolving solution on Matrigel network is negligible. Scale bars: 30 μm.

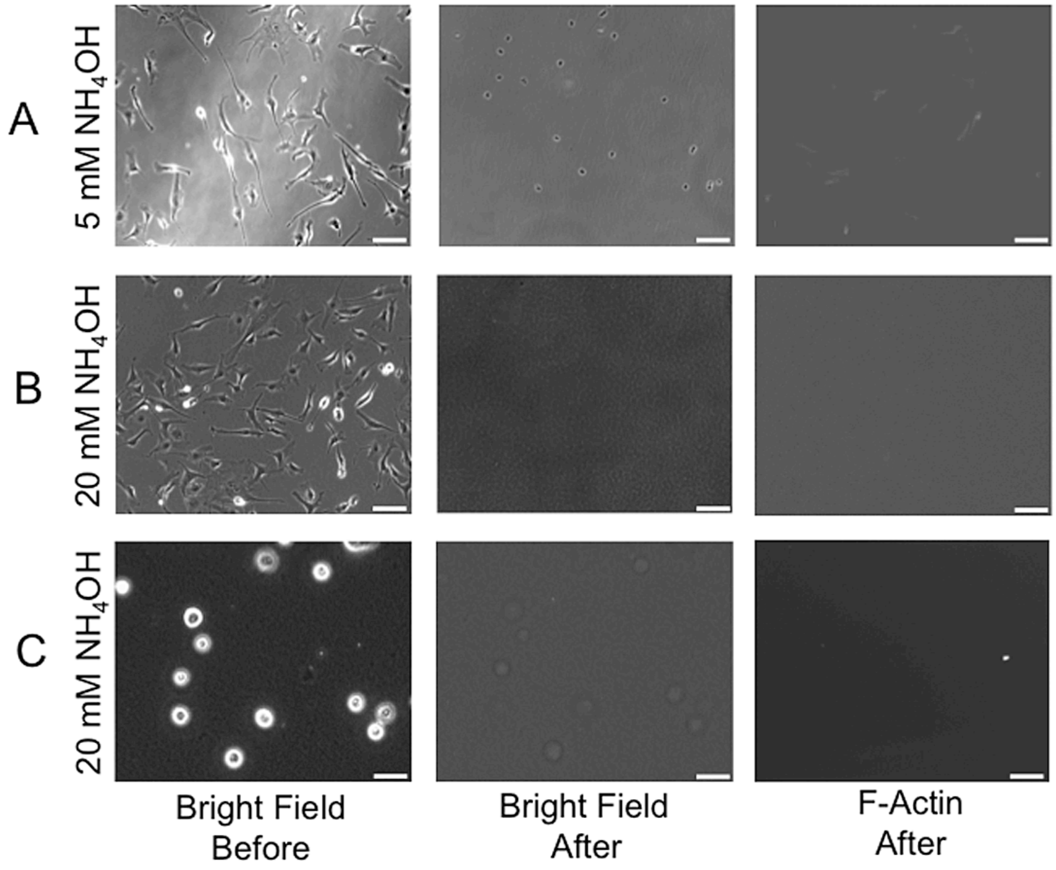

Figure 2.3 Efficiency of cell removal.

MDA-MB-231 cells on Petri dishes were treated with cell dissolving solution containing 3% Triton-X 100 and (A) 5 mM and (B) 20 mM NH_4OH. (C) MDA-MB-231 cells invading into 30 μm thick Matrigels were treated with cell dissolving solution containing 20 mM NH_4OH and 3% Triton-X 100. Bright field images of cells were taken before (left column) and 15 minutes after (right column) the treatment with cell dissolving solution. F-Actin staining validates that 20 mM NH_4OH and 3% Triton-X 100 is sufficient to remove the cells (right column). Scale bars: 50 μm.

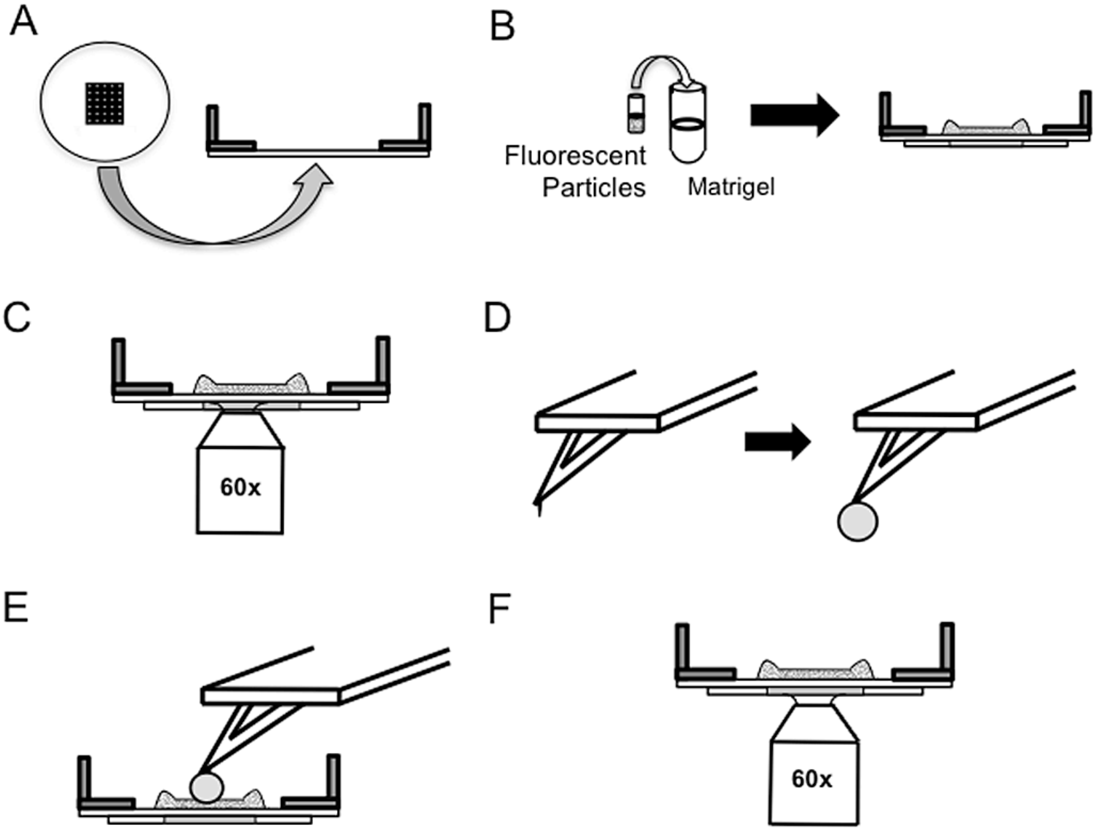

Figure 2.4: Schematic representation of the experiments utilized to determine the mechanical yielding of the Matrigel in the absence of cells.

(A) Cell lattice grid attached to glass-bottom dish. (B) Matrigel network embedded with fluorescent beads tethered to the glass-bottom dish. (C) Confocal microscope was used to acquire Z-stack images of the fluorescent beads at specific grid locations. (D) AFM cantilever tip modified with 30 μm diameter glass bead. (E) The modified cantilever was subsequently used to indent the pre-imaged locations of the Matrigel network using BAFM. (F) Re-imaging of the above locations (imaged in E) to determine permanent deformation of the Matrigel due to mechanical loading.

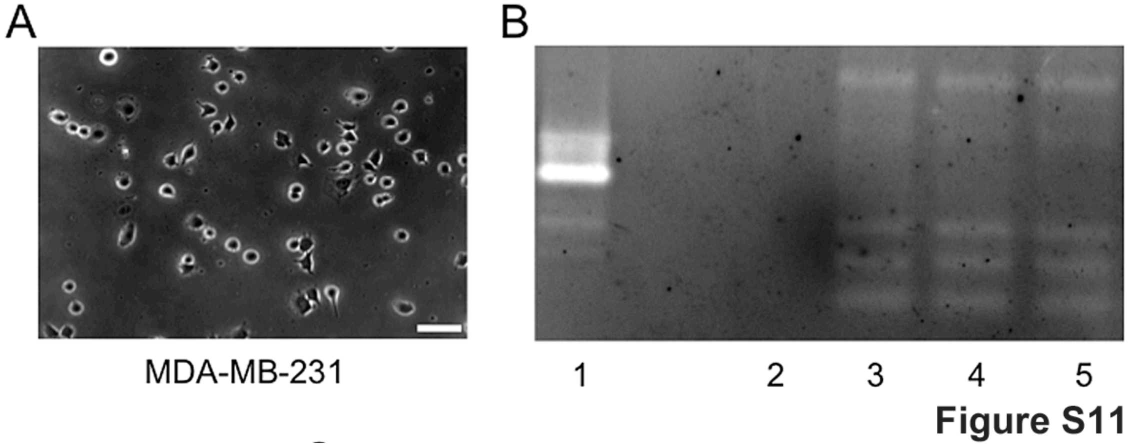

Figure 2.5: Secreted proteases during cell invasion using zymography.

(A) Phase contrast images of MDA-MB-231 cell cultured on 30 μm thick Matrigel in Opti-MEM (OM) at an initial cell density of 10,000 cells/cm^2. (B) Gelatin zymogram for different samples. Lane 1: 0.1 μg of bovine collagenase IV containing OM collected from acellular Matrigel as a positive control. Lane 2: OM incubated with Matrigel as a negative control. Lane 3: OM collected during cell invasion (ϕ_{3D} > 20°). Lane 4: OM collected during cell invasion incubated with 1 mM APMA dissolved in 80 mM NaOH to activate proenzymes. Lane 5: OM collected during cell invasion incubated with 80 mM NaOH.

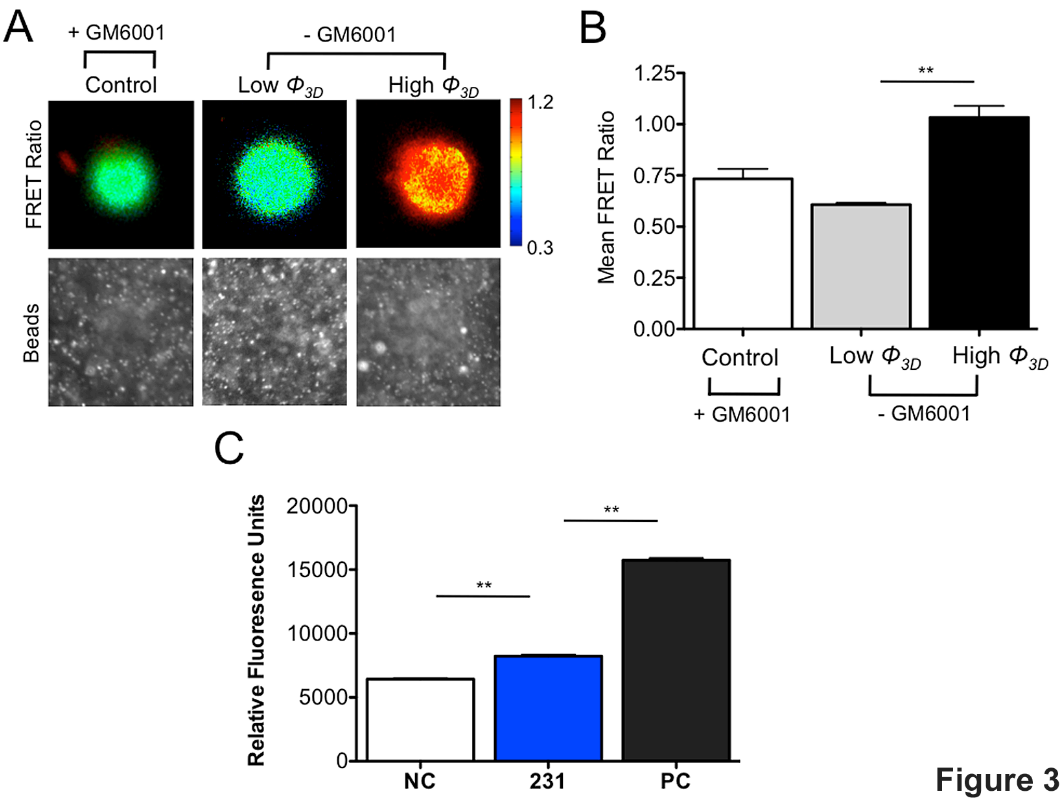

Figure 3

Figure 2.6: Protease activity during invasion of MDA-MB-231 cells into 30 µm thick Matrigel networks.

Cells were transfected with the MT1-MMP FRET biosensor to detect the activity of MT1-MMP at the cell surface. High FRET ratio indicates active MTI-MMPs at the cell surface. (A) The MT1-MMP activity map for cells invading into 30 µm thick Matrigel for low ϕ_{3D} (< 10°) and high ϕ_{3D} (> 20°). The MMP inhibitor GM6001 was used as a control (left panel). (B) The corresponding mean FRET ratios where the mean FRET ratios of cells at low ϕ_{3D} were found to be significantly lower compared to cells at high ϕ_{3D} values. ** denotes statistical significant amongst groups ($p < 0.05$) calculated using T-test ($n > 12$). (C) Fluorogenic peptide assay for broad-spectrum secreted proteases measured at 405 nm wavelength is shown for NC, 231, and PC. NC and PC indicate negative control (growth medium collected from acellular Matrigel) and positive control (growth medium collected from acellular Matrigel containing bovine collagenase IV), respectively, while 231 indicates medium collected Matrigel networks with invading MDA-MB-231 cells ($\phi_{3D} > 20°$). ** denotes statistical significance amongst groups ($p < 0.005$) calculated based on one way analysis of variance (ANOVA) followed by Bonferroni post-test ($n = 3$). The error bars indicate the standard deviation of the measurements.

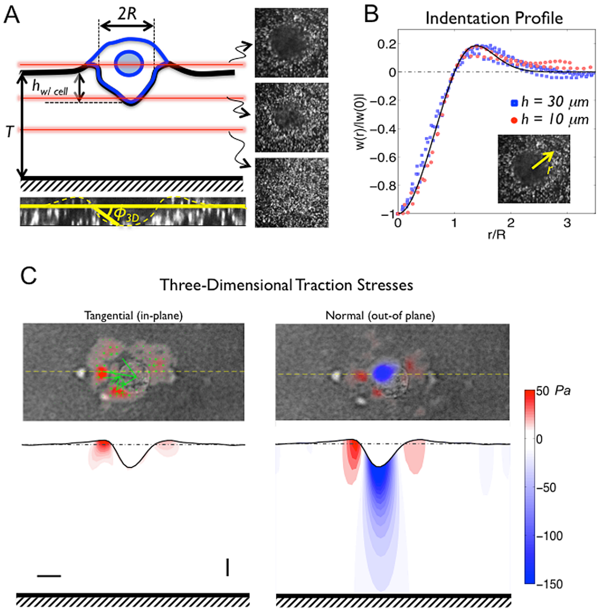

Figure 2.7: Quantitative single cell invasion assay

(A) Schematic representation of a cancer cell (MDA-MB-231) invading into a Matrigel network embedded with 200 nm fluorescent beads and tethered onto glass. Experimentally obtained confocal z-stack images are shown. The red lines illustrate the confocal sectioning along the vertical axis of the invading cells. $h_{w/cell}$ and R denote the depth and radius of matrix indentation during cell invasion, respectively. T is the thickness of the Matrigel. ϕ_{3D} is the indentation angle, defined as $\phi_{3D} = tan^{-1}(h_{w/cell} / R)$. (B) Indentation profiles generated by invading cells along the radial direction (shown in the inset image) are shown in blue squares and red circles for cells in 30 μm (n=4) and 10 μm (n=2) thick Matrigels, respectively. The black line is a semi-empirical fit, which shows an agreement between the experimental data and the model and satisfies mechanical equilibrium. The y-axis indicates the normal deformation at various radial locations, w(r), normalized to the deformation at the center of the indentation, w(0). (C) Maximum compressive stresses exerted by the same cells in panel B, obtained using our novel reference-free TFM method (x axis) and the full 3D TFM method of del Alamo et al (107) (y axis). The solid line represents x=y (zero error) while the dashed lines represent y = 0.75 x and y = 1.25 x. (D) Tangential and normal traction stresses of MDA-MB-231 cells elastically deforming a 30 μm thick Matrigel obtained using 3DTFM. The top panels display the traction stresses on the free surface of the gel (i.e. x-y plane) superimposed on the DIC cell image. The bottom panels display the measured traction stresses and deformation profile on the vertical section of the gel (i.e. x-z plane) corresponding to the yellow dashed lines in the top panels, showing the propagation of normal stresses into the gel. The color bar represents the magnitude of the stresses and the green arrows indicate the direction and magnitude of the tangential stresses. Horizontal and vertical scale bars are 5 and 1 μm, respectively.

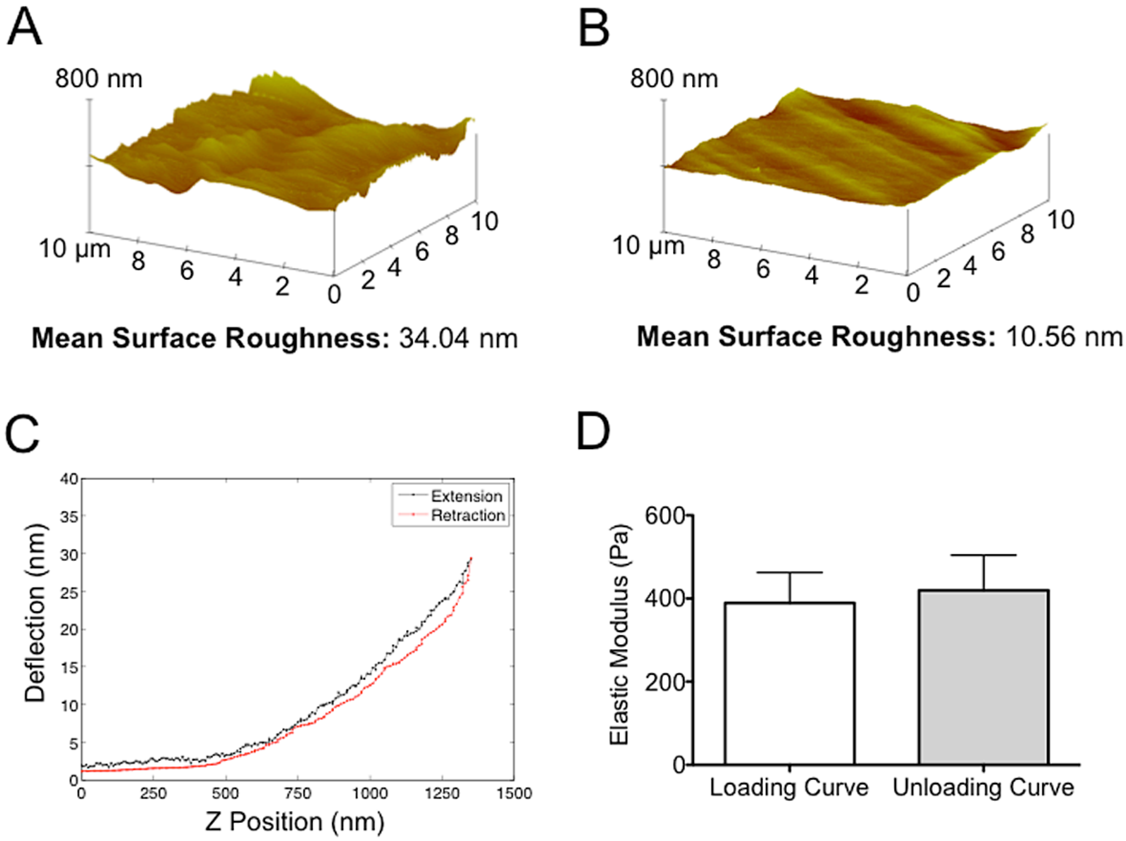

Figure 2.8: Characterization of Matrigel networks tethered to glass.

Surface topography and roughness of 30 µm (A) and 10 µm (B) thick Matrigel networks tethered to glass were obtained by using a BAFM. (C) The elastic modulus of the 30 µm thick Matrigel estimated from the indentation of several locations of the equilibrated Matrigel. The Hertzian model corrected for finite thickness was fitted to the approach and retraction curves to obtain the elastic modulus of the Matrigel network.

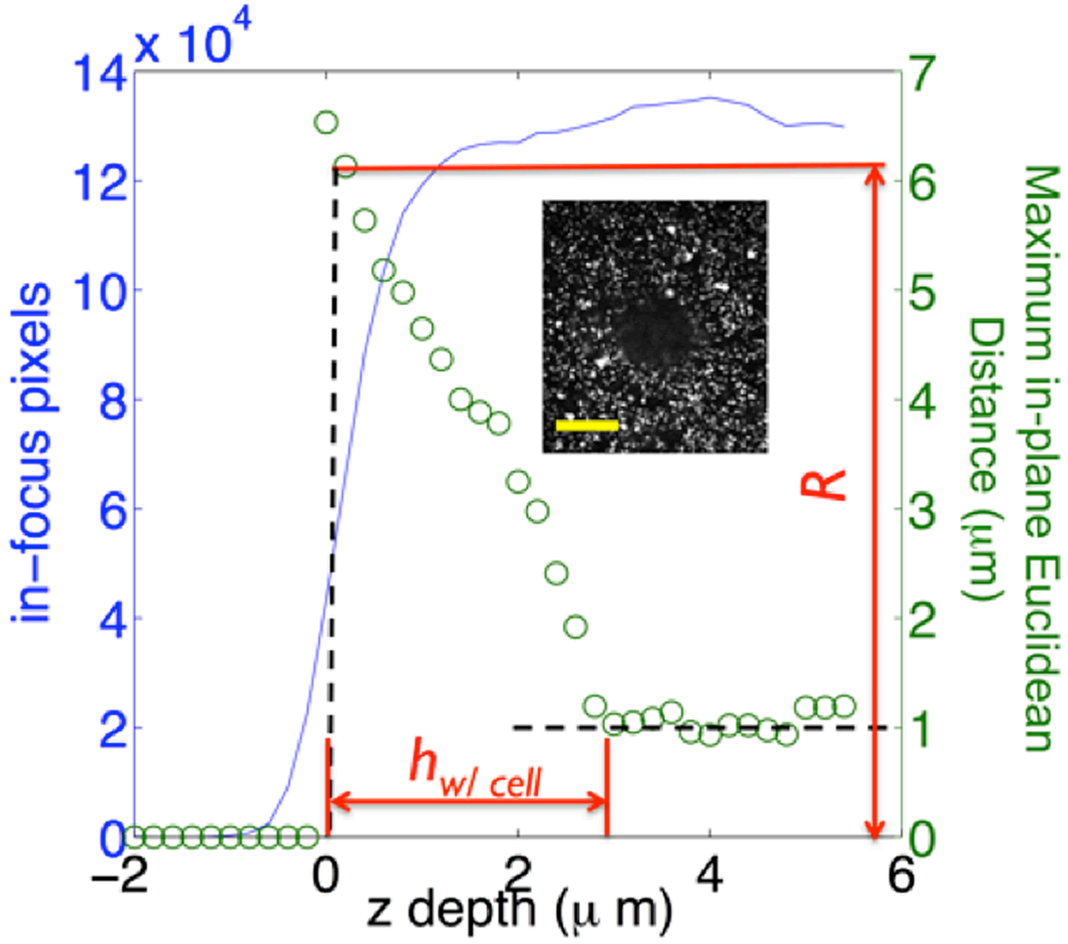

Figure 2.9. Quantification of the matrix indentation profile caused by the invading cells from confocal images.

Image analysis of a confocal fluorescent bead z-stack of a Matrigel network embedded with fluorescent beads that has been indented by an invading cell (see inset, scale bar = 5 microns). The indentation appears as a dark region of out-of focus beads that have been displaced downwards by the cell. Blue line (left y-axis): Number of in-focus pixels in each z-slice as a function of z. The z-position with highest variation of in-focus pixels corresponds to the top surface of the network. Green circles (right y-axis): Maximum Euclidean distance to an in-focus pixel in each z-slice as a function of z. The maximum value of the Euclidean distance in the whole Matrigel was defined as R. The z-slice at which the Euclidean distance reached its floor was designated as the bottom of the cell. The z-distance between the top and bottom slices allows to determine $h_{w/\,cell}$.

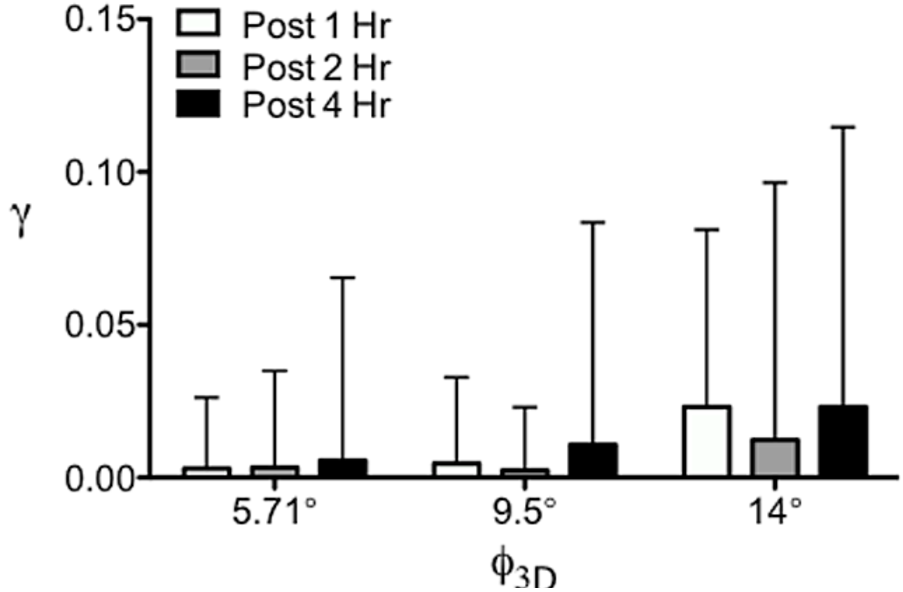

Figure 2.10: Effect of time on degree of permanent deformation.

Graph of the extent of permanent matrix deformation, γ, at different ϕ_{3D}, where the cells were allowed to invade into 30 μm thick Matrigel for 1, 2, and 4 hours, rules out the influence of time on γ. The plot was generated by binning the cell population around the listed angles with an allowance of ± 1°.

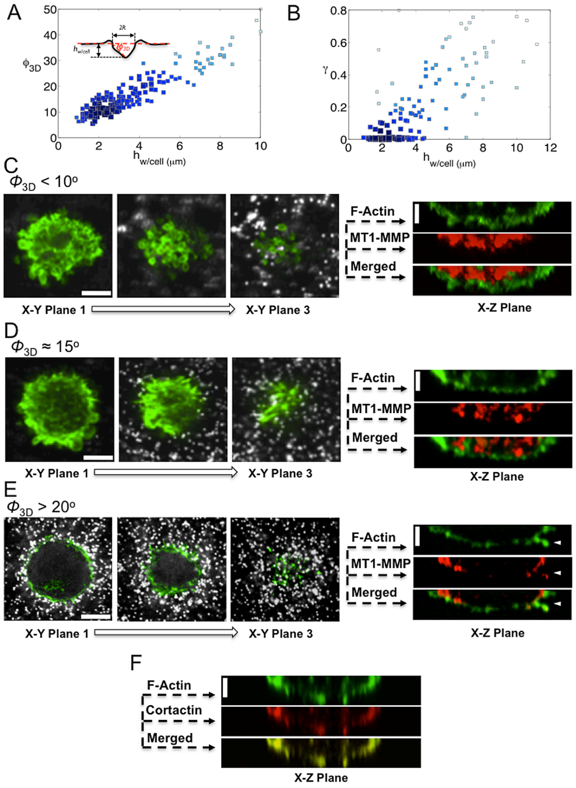

Figure 2.11: Invasion of MDA-MB-231 cells into 30 μm thick Matrigel networks.

(A) Scatter plot of the increase in the indentation angle, ϕ_{3D}, as the cells invade into the Matrigel network. Each symbol corresponds to one cell. The size and color of the symbols is proportional to the density of data points such that large, dark symbols indicate highly frequent observations. The inset shows the schematic of the matrix indentation generated by the invading cells. (B) Corresponding scatter plot showing the extent of permanent matrix deformation caused by the invading cells, γ, as a function of invasion depth, $h_{w/cell}$. Similar to panel A, each symbol corresponds to one cell and large, dark symbols indicate highly frequent observations. (C-E) Confocal z-slice images of the invading cells as a function of ϕ_{3D}. (Left panels) X-Y images showing the F-actin staining (green) and beads (white) within the network. (Right panels) X-Z section of the corresponding X-Y image stacks for F-actin (green) and MT1-MMP (red). At $\phi_{3D} \leq 10°$, plasma membrane blebbing was observed (X-Y Plane 1-3), while MT1-MMP was located in the cytoplasm (X-Z Plane). At $\phi_{3D} \sim 15°$, the extent of blebbing diminished and MT1-MMP was again detected within the cytoplasm. At $\phi_{3D} \geq 20°$, actin rich invadopodia-like protrusions filled with MT1-MMP were observed at the cellular cortex as indicated by the arrows. (F) Co-localization of F-actin and cortactin confirms invadopodia formation. Both horizontal and vertical scale bars represent 10 μm.

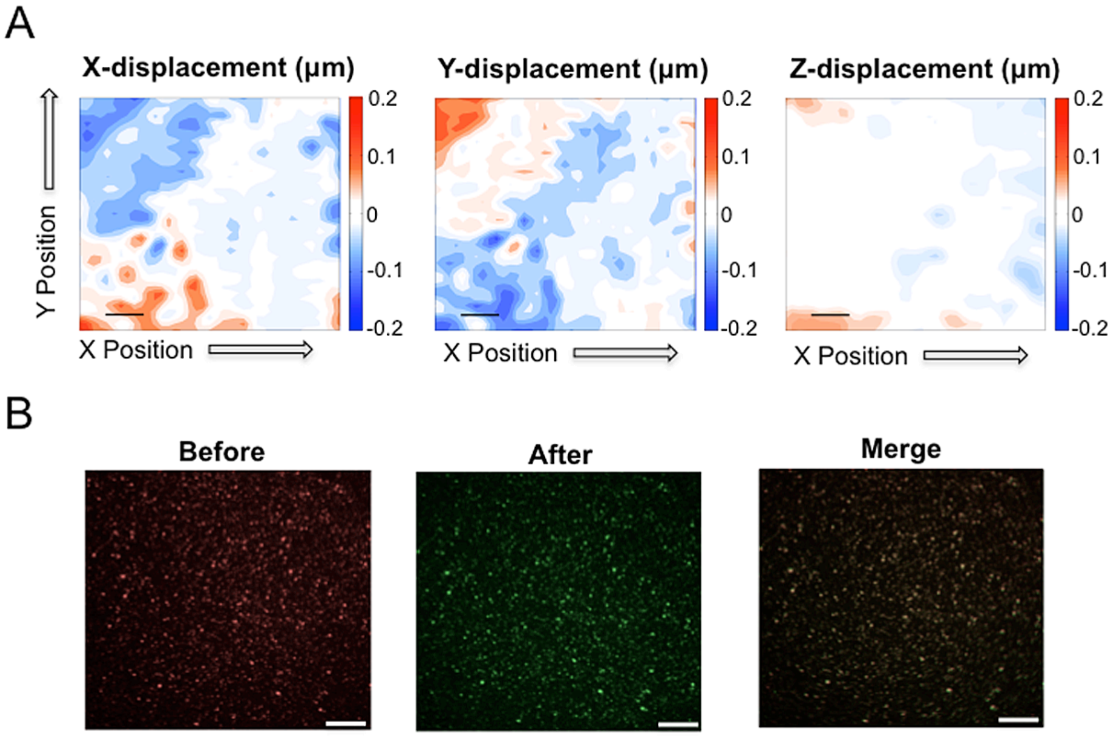

Figure 2.12: Matrigel networks exhibit complete elastic recovery for compressive stresses >200 Pa.

(A) Three components of the displacement field measured for a Matrigel network that was subjected to a compressive pressure of 207.4 Pa. (B) Confocal images of the Matrigel networks embedded with beads before and after subjecting them to the compressive pressure. The identical images reveal the absence of any permanent matrix deformation due to the application of compressive pressure of 207.4 Pa. Scale bars: 10 μm.

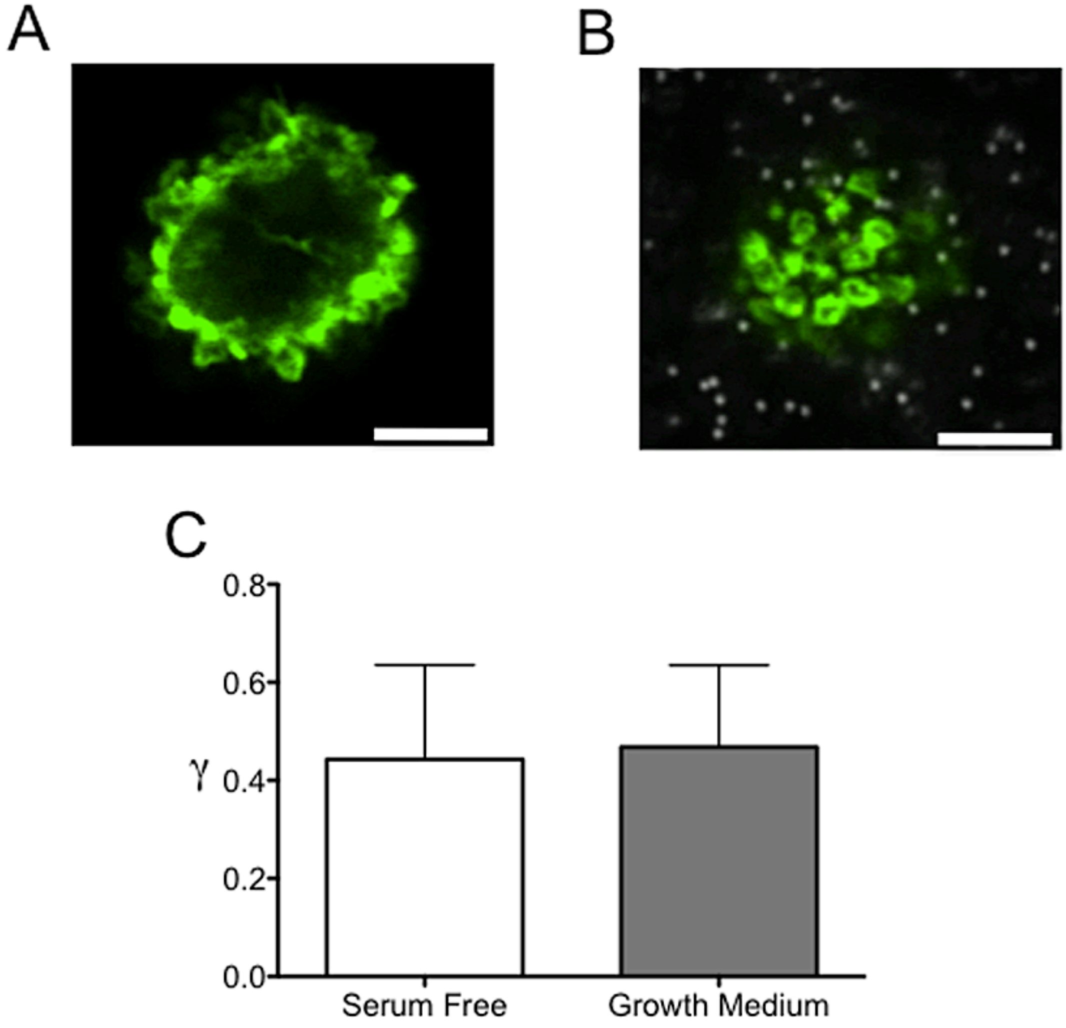

Figure 2.13: Invasion of cells in serum free conditions.

The invasion of MDA-MB-231 cells in a serum free condition was analyzed for 30 μm thick Matrigels. F-actin staining shows blebbing of the invading cells as indicated by curved actin structures from the confocal section of the cell 10 μm above the leading edge (A) and at the leading edge (B). (C) The gamma values generated by the cells are comparable in both growth medium containing serum and serum free medium at ϕ_{3D}> 20°.

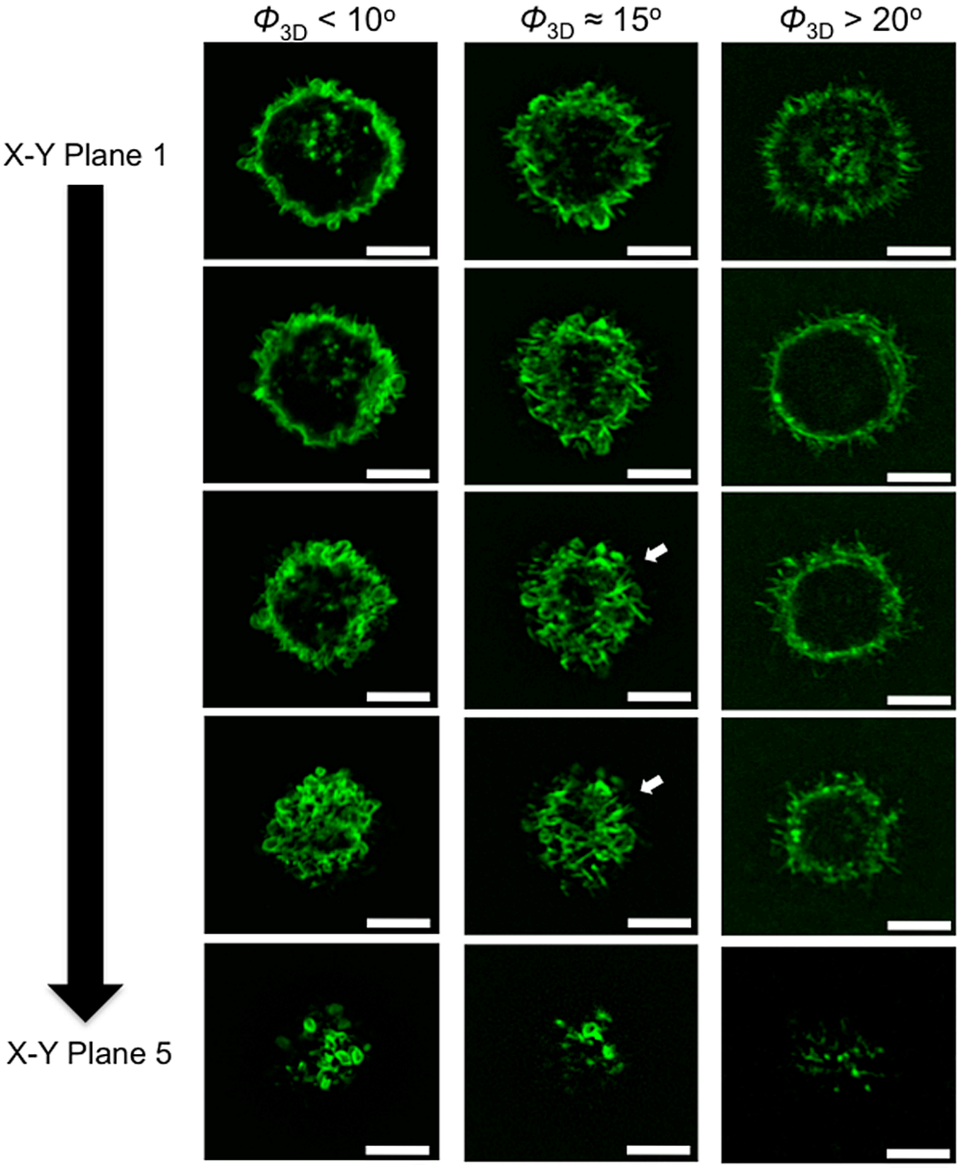

Figure 2.14: Morphological transition at the leading edge of the cells invading into 30 μm thick Matrigel.

Cross sectional images of cells stained for F-actin at different ϕ_{3D} values. X-Y Plane 1 indicates the region 10 μm above the leading edge while X-Y Plane 5 indicates the leading edge of the invading cell. White arrows show the actin-rich protrusions. Scale bar: 10 μm.

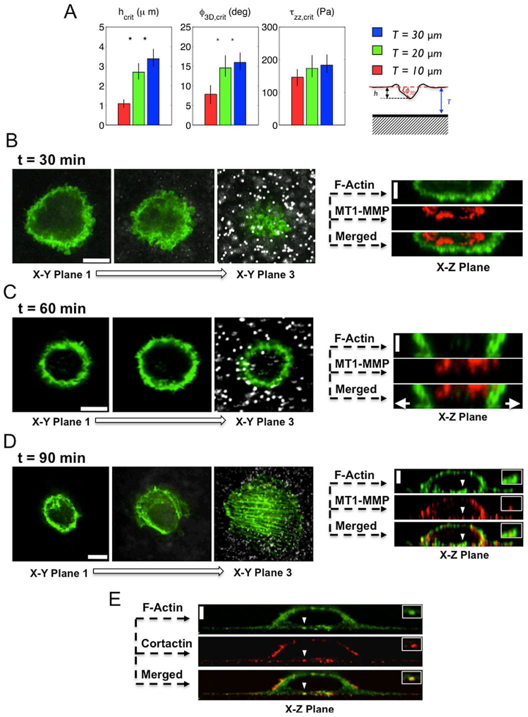

Figure 2.15 Effect of mechanical resistance on the invasion of MDA-MB-231 cells into Matrigel networks.

(A) h_{crit}, $\phi_{3D,crit}$, and $\tau_{zz,crit}$ for cells invading into Matrigel networks of varying thickness (T = 10 (red), 20 (green) and 30 (blue) μm) calculated between γ values of 0.05 to 0.2. Stars denote statistically significant differences amongst groups using the Kruskal-Wallis non-parametric analysis of variance (* and * denote $p < 0.005$ and $p < 0.05$ respectively). The error bars indicate the 5% confidence interval of the mean (n = 73, 88 and 161, respectively, for T = 10, 20 and 30 microns). (B-D) Confocal images of the cells invading into a 6 μm thick Matrigel network at $\phi_{3D} \leq 5°$ with varying post-plating time (30-90 min). (Left panels) X-Y images showing the F-actin staining (green) and beads (white) within the network. (Right panels) X-Z section of the corresponding X-Y images for F-actin (green) and MT1-MMP (red). At t = 30 min, plasma membrane blebbing was observed in cells similar to invasion into 30 μm thick Matrigel (X-Y Plane 1-3). MT1-MMP was detected within the cytoplasm (X-Z Plane). At t = 60 min, the blebs were found to divert along the Matrigel surface as indicated by arrows (X-Y Plane 1-3). MT1-MMP was again detected within the cytoplasm (X-Z Plane). At t = 90 min, cells adopted a spread morphology with the appearance of actin stress fibers at the basal domain of the cell (X-Y Plane 1-3). The MT1-MMP translocated to the cellular periphery (X-Z Plane). (E) The presence of invadopodia is observed through colocalization of cortactin and F-actin at discrete locations. The insets in the X-Z plane in (D) and (E) illustrate the zoomed in images of the location of invadopodia formation indicated by the white arrows. Both horizontal and vertical scale bars represent 10 μm.

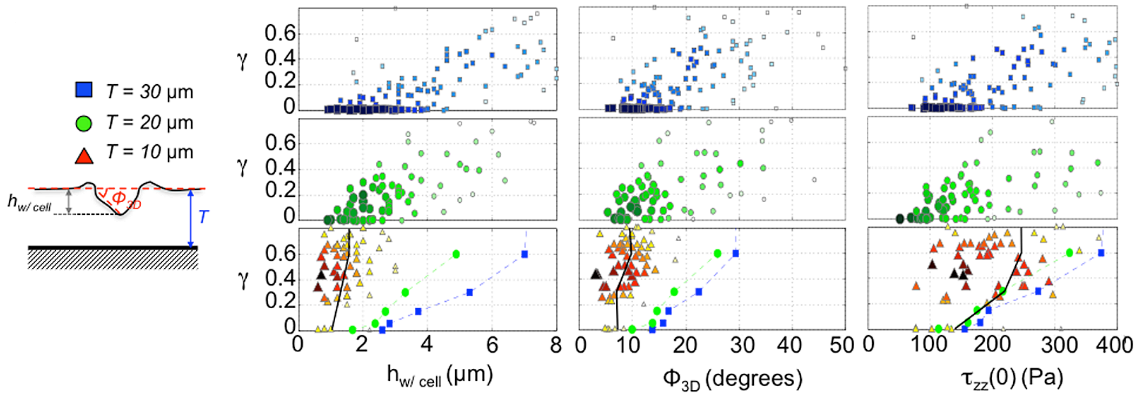

Figure S13

Figure 2.16: Establishing the dependence of γ on $h_{w/cell}$ ϕ_{3D}, and τ_{zz}. S

Scatter plots showing the extent of permanent matrix deformation caused by the invading cells, γ, in Matrigels of varying thickness, *T*, and represented as a function of different parameters listed below. In all panels, each symbol corresponds to one cell. The size and color of the symbols is proportional to the density of data points such that large, dark symbols indicate highly frequent observations. Left column: γ versus cell penetration $h_{w/cell}$ (units μm). Center column: γ versus cell indentation angle ϕ_{3D}. Right column: γ versus maximum compressive traction stress, $\tau_{zz}(0)$ (units Pa). Top row (blue squares): *T* = 30 μm; middle row (green circles): *T* = 20 μm; bottom row (red triangles): *T* = 10 μm. The line plots in each panel of the bottom row represent the median values of $h_{w/cell}$ (left column), ϕ_{3D} (center column) or $\tau_{zz}(0)$ (right column) corresponding to each value of γ for the three Matrigel thicknesses (blue line: *T* = 30 μm, green line: *T* = 20 μm, black line: *T* = 10 μm) to indicate collapse or lack of collapse of the data obtained for different *T* values.

Chapter 3: MT1-MMP trafficking in protease dependent invasion of cancer cells utilizes CARTS secretory pathway

3.1. Abstract

Invasion and migration of cancer cells within a 3D environment is a physical process by which cancer cells push and pull against their surroundings to traverse extracellular matrix (ECM) networks. During this process, the pliability of the cell and the ECM network along the forces generated by the cells determine whether the invading cells utilize protease dependent or independent mode of migration. In protease dependent migration, cells translocate a key matrix metalloproteinase (MT1-MMP) from the cytoplasm to the cell surface where this protease activates other MMPs as well as actively degrade the surrounding ECM to aid cell locomotion. In this study, we illustrate that the cancer cells employ a regulated transport pathway known as CARriers of the TGN to cell surface (CARTS) to shuttle MT1-MMP from the cytoplasm to the cell surface during invasion into Matrigel networks. Our results indicate that MT1-MMP is indeed found within golgi vesicles involved in the CARTS pathway and in addition, the disruption of the CARTS pathway via inhibition of vesicle formation, down regulation of CARTS specific kinesin motor proteins, and loss of CARTS vesicular marker inhibited the formation of invadopodia-like structures during migration and impeded the invasion process.

3.2. Introduction

Metastasis of cancer is the leading cause of death amongst people afflicted with this disease. This process begins with the invasion of cancer cells from the primary tumor to adjacent tissues where the migrant cells intravasate into local blood vessels, extravasate to a secondary site, and form a new tumor mass. The initial stages of metastasis in which cancer cells invade into and migrate within the adjacent tissues has garnered a substantial focus on understanding the process by which these cells traverse the extracellular matrix (ECM) networks with a wide variety of physicochemical properties such as pore structures, mechanical properties, or protein composition (81, 86). Emerging studies have shown that cancer cells can migrate both in a protease dependent or independent manner in response to the physicochemical properties of the ECM (8). Recently, we have shown that 3D compressive traction stresses generated by the cells modulates the transition from bleb-mediated protease independent to invadopodia-mediated protease dependent mode of invasion into ECM networks (35).

The transition between the different modes is distinguished by the formation of invadopodia, which is a key cellular machinery required for protease dependent migration and invasion (116, 126). Within these actin-rich protrusions, numerous matrix-metalloproteinases (MMP) accrue amongst which MT1-MMP has been touted as a key regulator of proteolysis (115, 127). Studies have established the role of MT1-MMP in activating other secreted MMPs such as MMP-2 and MMP-9—both of which are hallmark secretory MMPs of invasive cancer cells (127-129). Additionally, the significance of the MT1-MMP is further highlighted by the impaired migration of cancer cells devoid of this membrane bound MMP within crosslinked and rigid ECM networks which render the cells incapable of deforming the fibers and/or squeezing through the pore structures (130-132).

The crucial role of MT1-MMP during protease dependent migration elicits a further understanding of its transport mechanism from the cytoplasmic vesicles to the invadopodia. Recent findings indicate that transport of MT1-MMP to the plasma membrane is a crucial means to regulate its activity within the cell (115, 130, 133, 134). Studies have demonstrated that MT1-MMP synthesized *de novo* resides within the Golgi prior to being transported to the plasma membrane while the recycled MT1-MMP shuttles between the trans-Golgi network, late endosomal vesicles, and the plasma membrane (135, 136). Additionally, *Bravo-Cordova et al.* has identified Rab8 as the GTPase involved in the vesicular transport of MT1-MMP within cancer cells (133). Despite the findings of these studies, the exocytotic pathway through which MT1-MMP is transported remains elusive. Within this study, we employed an invasion assay into Matrigel networks and observed that the transport of MT1-MMP after the transition from protease independent to dependent mode of invasion occurs via CARTS pathway, a newly identified regulated secretory pathway (137). The inhibition of the CARTS pathway resulted in the impaired invasion into the Matrigel network as well as the loss of invadopodial protrusions indicative of protease dependent invasion.

3.3. Materials and Methods

3.3.1. Cell Culture

MDA-MB-231 were cultured in growth medium containing Dulbecco's modified eagle medium (DMEM; high glucose; Hyclone), 10% (vol/vol) fetal bovine serum

(Gibco), supplemented with 100 units/mL of penicillin, and 100 μg/mL of streptomycin (Gibco). PC-3 were cultured in growth medium containing F-12K Kaighn's medium (Life Technologies) with 10% (vol/vol) fetal bovine serum (Gibco), 100 units/mL of penicillin, and 100 μg/mL of streptomycin (Gibco).

3.3.2. Plasmid Transfection

MDA-MB-231 cells were plated into 24-well plates, cultured in GM, and allowed to reach 80 % confluency. Cells were transfected with the mRFP-PAUF plasmid using Fugene HD Transfection Reagent (Promega) two days prior to the experiments. Each well containing the cells was exposed to 1.7 μL of Fugene transfection reagent mixed with 25 μL of OptiMEM (OM) (Life Technologies) containing 1.1 μg of the plasmid.

3.3.3. siRNA knockdown

For knockdown studies, MDA-MB-231 and PC-3 cells were transfected with 2.5 nM of each targeting and sham siRNA oligonucleotides (Silencer Select; Life Technologies) according to the manufacturer's instructions. Briefly, siRNA and RNAimax were first individually mixed with OptiMEM (Life Technologies), both solutions were then incubated together for 5 minutes at room temperature before being added to cells in the presence of growth medium. Sham oligonucleotide sequences are 5' UAACGACGCGACGACGUAAtt 3' (sense), 5' UUACGUCGUCGCGUCGUUAtt 3' (antisense); TGN46 Type I (TGOLN2) oligonucleotide sequences are 5' CAACAAGCGGAAGAUCAUUTT 3' (sense), 5' AAUGAUCUUCCGCUUGUUGTG

3’ (antisense); and Eg5 (KIF11) oligonucleotide sequences are 5’ GACUGAUCUUCUAAGUUCAtt 3’ (sense), 5’ UGAACUUAGAAGAUCAGUCtt 3’ (antisense).

3.3.4. Activation of glass surface

The procedure for activating glass surfaces to be amine-reactive was adapted from previous studies (35). In brief, glass surfaces within 14 mm diameter glass-bottom dishes (MatTek) were treated with 0.1 M NaOH for 30 minutes, rinsed in DI water, and dried using an aspirator. The cleaned glass surface was treated with 3-Aminopropyl-trimethoxysilane (Sigma-Aldrich) for 5 minutes prior to rinsing in DI water and drying. The glass surface was treated with 0.5% Glutraldehyde for 40 minutes and rinsed in DI water to complete the activation process. The glass-bottom dishes were used immediately.

3.3.5. Fabrication of 30 µm thick Matrigel networks tethered to glass

Aliquot of frozen Matrigel solution (Corning) was thawed on ice at 4° C for 16 hours. Crimson beads of 200 nm diameter (Fluorospheres from Life Technologies, max excitation at 660 nm and max emission at 680 nm) were dispersed in the thawed solution to reach a concentration of 2% v/v. 28 µL of the mixture was spread over the activated glass surface within the 14 mm diameter glass-bottom dish. The solution was immediately spin-coated at 400 RPM for 1 minute using Spin Coater KW-4A (Chemat Scientific) to thin down the polymer solution prior to incubating the dish at 37 °C for 6 minutes to complete the gelation process. The resulting Matrigel network was incubated in PBS for 30 minutes before UV-sterilizing for 30 minutes. PBS was replaced with growth medium and was incubated overnight at 37 °C and 5% CO_2 prior to the plating of cancer cells.

For studies analyzing the effect of PKI and H89 on cancer cell invasion, Matrigels of 30 μm thickness were synthesized as previously mentioned and were incubated in GM containing 8.5 μM PKI (EMD, Millipore) or 20 μM H89 (EMD, Millipore) overnight.

3.3.6. Single cell invasion assay

Cancer cells were plated onto 30 μm thick Matrigel tethered onto glass at a density of 5000 cells/cm^2 in growth medium. The cells were allowed to invade into the matrix for 2 hours prior to imaging the cells using a spinning disk confocal microscope (Perkin Elmer UltraView Vox Spinning Disk Confocal). Z-stack images were obtained from 3 μm above the surface of the Matrigel to 2 μm below the maximum invasion depth of the cancer cell at vertical increments of 0.2 μm. The surface of the Matrigel was approximated as the Z plane in which the fluorescent beads come into focus while the maximum invasion depth was approximated as the plane at which the indentation observed within the beads disappears.

For cancer cell invasion in presence of H89 and PKI, the cells were resuspended in GM containing 8.5 μM PKI or 20 μM H89 for 20 minutes at 37 °C prior to plating onto Matrigel networks that were also preincubated overnight with PKI or H89.

3.3.7. Image analysis to quantify maximum invasion depth, h_{inv}

The maximum invasion depth, h_{inv}, was quantified as previously described using a custom Matlab algorithm (35). Briefly, the z-stack image volume was normalized to the mean intensity of the image volume. Individual z slices were passed through a Sobel edge detection filter to quantify the number of pixels in focus for each z plane. The z plane at which the maximum change in the number in focus occurs was designated as the top surface of the Matrigel. To determine h_{inv}, we quantified the Euclidean distance transform for each individual z slice subsequent to the top surface of the Matrigel. The value of the distance transform reaches its maximum at the surface of the Matrigel due to the indentation caused by the cell and reaches its minimum at the bottom of the cell where the indentation dissipates. By scaling the difference between z plane at which the top surface of the Matrigel and the z plane at which the minimum value of the distance transform is reached to z spacing between each slice, we obtain the maximum invasion depth of the invading cell, h_{inv}.

3.3.8. Immunofluorescent Staining

To stain the invading cells at $h_{inv} > 4$ μm, cancer cells were plated onto 30 μm thick Matrigel networks tethered onto glass at a density of 5000 cells/cm^2. The cells were allowed to invade into the matrix for 2 hours prior to fixing with 4% paraformaldehyde for 10 minutes, washing with PBS thrice at 10 minute intervals, and blocking with 2% Bovine Serum Albumin and 0.1% Triton-X100 in PBS (blocking buffer). The sample was incubated with primary antibody for MT1-MMP (Abcam, Cat. Ab38970) diluted

1:100 in for one hour in blocking buffer. The samples were rinsed thrice with PBS at 10 minutes intervals prior to adding Alexa Fluor 568-conjugated secondary antibody (Life Technologies) for MT1-MMP and Alexa Fluor 488-conjugated Phalloidin (Life Technologies), both diluted 1:250 in blocking buffer, for 1 hour at room temperature. The sample was rinsed thoroughly with PBS prior to imaging.

To stain the invading cells at $h_{inv} < 2$ μm, cancer cells were plated onto the Matrigel network at a density of 20,000 cells and were allowed to invade for 15 minutes. The high cell density was used to ensure that sufficient number of cells have adhered onto the surface during the short duration allotted for invasion. The cells were fixed with 0.1% Glutraldehyde for 1 minute before washing thoroughly with PBS thrice at 10 minutes interval. To quench the autofluoresence caused by the unreacted aldehehyde groups, 0.1% w/v sodium borohydride in PBS was added for thirty minutes before washing in PBS twice. The samples were subsequently incubated in blocking buffer, primary, and secondary antibodies as described above.

For immunostaining of cells transfected with mRFP-PAUF at both $h_{inv} < 2$ μm and $h_{inv} > 4$ μm, the cells were permeabilized with 50 μg/mL digitonin in PBS instead of Triton-X 100 for 15 minutes prior to the addition of antibodies. The immunostained samples were imaged using Olympus FV1000 Laser Scanning Confocal microscope or Perkin Elmer UltraView Vox Spinning Disk Confocal. A z-slice spacing of 200 nm was used to generate 3D image stacks. The primary antibodies used were anti-MT1-MMP (Abcam), anti-TGN46 (Sigma-Aldrich) and Alexa Fluor 488-conjugated Phalloidin (Life Technologies).

3.3.9. PAUF Secretion Assay

Frozen aliquots of Matrigel solution was thawed as previously described. A 24 well plate was chilled on ice and at 4° C prior to adding and spreading 20 μL of the thawed solution in each well to result in a Matrigel with a thickness of ~ 30 μm. The plate was kept at 4° C on a flat surface for 10 minutes before transferring to 37° C for 20 minutes to complete the gelation process. The Matrigel networks were incubated in PBS at 37° C for 30 minutes and were UV-sterilized for an additional 30 minutes. PBS was replaced with a mixture of GM and 0.1% DMSO before incubating overnight at 37° C and 5% CO_2 prior to seeding the cancer cells. To measure the PAUF secretion in presence of PKD blocker H89, Matrigel networks were instead incubated in GM containing 20 μM of H89.

MDA-MB-231 cells transfected with mRFP-PAUF were plated onto the Matrigel networks formed within the 24 well plates in 500 μL of GM and 0.1% DMSO. Time zero readings for the negative control and the growth medium was generated using medium containing GM and 0.1% DMSO from acellular Matrigel and medium from cells in suspension prior to seeding them on Matrigel, respectively. The mRFP-PAUF secretion from the cells invading into the Matrigel was examined as a function of time (1, 2, and 4 hrs post-plating). At specified time points, 105 μL of the media was collected from each well and centrifuged. 100 μL of this collected medium was transferred into a 96-well plate and used for fluorometric measurements. A plate reader (Infinite 200 Pro, Tecan) with an excitation and emission wavelengths of 568 ± 4.5 and 600 ± 10 nm, respectively, was used. To measure the PAUF secretion in presence H89, the cells were incubated with

GM containing 20 μM of H89 for 10 minutes in suspension prior to plating. GM containing 20 μM of H89 from acellular Matrigel networks were used as negative control for cells invading in the presence of H89.

To determine the maximum invasion depth, h_{inv}, as a function of time, cells were plated onto Matrigel networks tethered to glass bottom dishes as previously described. Cells were allowed to invade into the matrix for 1, 2, and 4 hours prior to imaging using a spinning disk Confocal. The confocal z-stacks were analyzed for h_{inv} as described above.

3.3.10. Western blot

Cells were lysed in lysis buffer containing protease inhibitors (Sigma-Aldrich). Cell lysate was quantified with Bradford assay reagent (Bio-Rad), and electrophoresis was carried out on 8% polyacrylamide gels and then transferred to polyvinylidene fluoride (PVDF) membranes. Membranes were blocked and incubated with mouse TGN46 (Santa Cruz), mouse Eg5 (Santa Cruz) and mouse beta-actin (Santa Cruz) primary antibodies overnight at 4°C. Anti-mouse secondary horseradish peroxidase antibodies were incubated the next day for 1 hour. Membranes were covered in chemiluminescent substrate (GE Healthcare) and imaged with a FluorChem E System imager (ProteinSimple) for chemiluminescence.

3.4. Results

3.4.1. Cancer cells transition from protease independent to dependent mode during invasion

MDA-MB-231 cells invading into 30 μm thick Matrigel network tethered onto glass were immunostained for F-actin and MT1-MMP at various maximum invasion depths. At $h_{inv} < 2$ μm, cells employ protease independent mode of invasion. The confocal sections indicate the presence of actin mediated bleb formations, which are predominantly observed at the leading edge of the cell (Fig. 3.1A). MT1-MMP was sequestered within the cell cytoplasm suggesting the lack of protease activity on the cell surface (Fig. 3.1A, B). As the cancer cells invade deeper into the matrix ($h_{inv} > 4$ μm), a transition from protease independent to dependent mode of invasion occurs where the formation of blebs are replaced by the actin-rich protrusions (Fig. 3.2A). Additionally, MT1-MMP was observed to translocate from the cytoplasm to the cell surface and localize within these protrusions (Fig. 3.2A, B). Previous studies have indicated that these actin-rich protrusion observed during protease dependent invasion are also enriched with cortactin indicating that these protrusions are invadopodia-like structures (35).

3.4.2. Protease dependent invasion utilizes CARTS pathway

While the transport of MT1-MMP from the cytoplasmic vesicles to the cell periphery during the transition into protease dependent invasion is intriguing, it is equally important to understand how this is achieved. We investigated the role of the recently identified CARTS (CARriers of the TGN to the cell Surface) pathway, which is distinct from the carriers of proteins that are constitutively secreted from the cell, on MT1-MMP translocation (137). Interestingly, for cells invading into a 30 µm thick Matrigel ($h_{inv} > 4$ µm), the MT1-MMP was found to co-localize with TGN46 within the Golgi apparatus, a protein landmark for the CARTS pathway (Fig. 3.3A, bottom). On the contrary, no such overlap was observed for cells with $h_{inv} < 2$ µm (Fig. 3.3A**,** top). Additionally, both MT1-MMP and TGN46 was found to co-localize with PAUF (pancreatic adenocarcinoma upregulated factor), a secretory cargo that utilizes CARTS on its way to being released from the cell (Figs. 3.3B, 3.4). Quantification of extracellular PAUF as the cells invaded into a 30-µm thick Matrigel shows an increase in PAUF secretion with increasing $h_{w/\text{cell}}$ (i.e., large matrix deformation) (Fig. 3.3C). Since the PAUF cargo is co-transported with MT1-MMP at $h_{inv} > 4$ µm, the increase PAUF secretion further supports the translocation of MT1-MMP from the cytoplasm to the cell periphery.

3.4.3. Inhibition of CARTS pathway impairs cancer cell invasion

To further verify the translocation of MT1-MMP through the CARTS pathway, we blocked Protein Kinase D (PKD), which is required for the fission of the transport carrier from the trans Golgi network (TGN) that is destined for the cell surface. Our blocking studies showed that the invasion of MDA-MB-231 cells was significantly impeded in the presence of H89. Since this pharmacological inhibitor is also known to inhibit Protein Kinase A (PKA), we used a PKA specific inhibitor (PKI) and found that the H89-mediated attenuation of cell invasion could not be recapitulated with PKI (Fig. 3.5A). The effect of H89 on cell invasion was also reversible where the removal of H89 from the culture restored the cell invasion (Fig. 3.6B**)**. In addition to invasion, the blocking of PKD with H89 prevented PAUF secretion (Fig. 3.6A).

To exclude the possibility of the off-target effects of H89, we investigated whether the knockdown of TGN46 via Si-RNA can recapitulate the effects of H89 on cancer cell invasion. Our results show that the downregulation of TGN46 within MDA-MB-231 cells post 2 days after Si-RNA treatment impairs the invasion of cancer cells (for the validation of TGN46 knockdown post Si-RNA treatment and the sustained effect of TGN46 knockdown on cancer cell invasion post 4 days after Si-RNA treatment see Figure 3.7A-C) (Fig. 3.5B). To determine the generality of impaired cancer cell invasion after the inhibition of CARTS pathway, we have also investigated the effect of TGN46 knockdown on PC3. Our results show that PC3 cell invasion into 30 μm thick Matrigel is abrogated post 2 days after knockdown (see Figure 3.8A-B for validation of TGN46 knockdown in PC3 cells) (Fig. 3.8A, D). Similarly, the downregulation of Eg5, a kinesin motor shown to transport CARTS specific vesicles, resulted in the impaired invasion of both MDA-MB-231 and PC3 cells into the Matrigel network (138) (Fig. 3.5C, 3.8B-C.

3.4.4. CARTS pathway inhibition prevents invadopodia formation during cancer cell invasion

To further determine whether the inhibition of CARTS pathway prevents the translocation of MT1-MMP from the cytoplasm to cell periphery, invading cancer cells were immunostained for actin and MT1-MMP. Confocal sections of Si-TGN46 treated cancer cells invading into the Matrigel network reveal the lack of actin rich protrusions indicative of invadopodia-like structures amongst cells at $h_{inv} > 2$ μm. Due to the lack of invadopodia-like structures, the MT1-MMP fail to localize at discrete locations as observed in Fig. 3.9, the MT1-MMP staining remains diffused within the cytoplasm.

Additionally, the lack of invadopodia-like structures at the cell periphery was not supplemented by bleb formations since the cortical actin reveals a smooth cell periphery (Fig. 3.9). Similarly, the lack of invadopodia-like structures was also observed after treatment with Si-Eg5 (Fig. 3.10). Together, these results suggest that CARTS inhibition impairs the invasion of cancer cells into Matrigel network via the lack of invadopodia formation, which requires the presence of MT1-MMP to trigger proteolysis.

3.4.5. Integrin dependent invasion of cancer cells into Matrigel network

Cancer cells were treated with siRNA to downregulate the expression of β1 or β2 integrins. The efficiency of the knockdown was assessed via western blot (Fig. 3.11A). Our results indicate that the downregulation of α_v or β_{II} impaired the invasion of cancer cells into the Matrigel network. However, the down regulation of both β1 or β2 integrin abrogated the invasion of cancer cells into the network (Fig. 3.11B).

3.5. Discussion

The current study indicates that cancer cells utilize CARTS pathway to transport MT1-MMP during protease dependent invasion into Matrigel networks. This pathway was also inhibited by preventing the biogenesis of TGN46 vesicles and downregulating the TGN46 marker or the kinesin motor transporter Eg5. The invasion of cancer cells into the Matrigel network was impeded irrespective of the stage at which CARTS pathway was inhibited. The immunostaining of cells inhibited by TGN46 or Eg5 both reveal the lack of invadopodia-like structures during the impaired invasion process.

3.5.1. Additional evidence of CARTS pathway involvement in MT1-MMP Transport

During cancer cell invasion into Matrigel networks, our immunostaining results have illustrated cytoplasmic MT1-MMP are packaged within the trans-Golgi network vesicles (TGN46) during proteolysis. Similar to these findings, *Wang et al.* also reported that the MT1-MMP, along with MT3-MMP, are observed to recycle through the trans-Golgi network (139). In addition, the study by Vivek and colleagues unveiling the newly discovered CARTS pathway demonstrated the involvement of Rab6 and Rab8 within the CARTS vesicles (137). Likewise, time-lapse microscopy of cancer cells co-transfected with GFP-Rab8 and RFP-MT1-MMP reveals the real-time transport of MT1-MMP and Rab8 containing vesicles to the cell periphery (133). Furthermore, our previous study has implicated the compressive traction stress as a modulator for protease dependent invasion of cancer cells into Matrigel network where the transport of MT1-MMP from the cytoplasm to the cell periphery occurs (35). Interestingly, the ability of the CARTS pathway to transport its cargo is dependent on non-muscle myosin II activity since the presence of blebbistatin inhibited the secretion of its cargo proteins such as Pancreatic Adenocarcinoma Upregulated Factor (PAUF) (137). Together, these findings further implicates the role of CARTS pathway in transporting MT1-MMP and the possibility that the traction stresses generated by the cells can be the regulatory signal required by CARTS.

3.5.2. Context specific use of CARTS during cancer cell invasion

The transport of MT1-MMP has been reported to occur from TGN to the plasma membrane for newly synthesized membrane bound MMPs or from the late endosomal vesicles to the plasma membrane for recycled MT1-MMPs (115, 136, 140). We have observed the use of CARTS pathway, which transport MT1-MMP from the TGN to the plasma membrane for cells that progressed from a non-adherent to adherent state as they invade into the matrix. The transition from a non-adherent state requires the mobilization of the actin and microtubule networks along with other cytoplasmic machinery required for transport mechanism indicative of booting an "offline" system. This specific context differs from other reported studies in which MT1-MMP transport was investigated in cancer cells that have adhered and engaged in the migration process. In these cells, the transport of MT1-MMP can drastically vary since the cellular infrastructure for golgi transport is already established. For these cases, the "front to back" recycling model of surface proteins that occurs for integrins is more likely plausible (141). To determine the generality of the CARTS pathway on the MT1-MMP transport, further studies are needed to analyze cells outside the context of invasion.

3.5.3. Invadopodia formation and CARTS inhibition

The disappearance of invadopodia amongst cancer cells knocked down for TGN46 and Eg5 implicates the inability of MT1-MMP to be transported from the cytoplasmic vesicles to these structures. This finding is further supported by studies showing the inability of actin and cortactin to cumulate and initiate the formation of invadopodia when cells were depleted for MT1-MMPs (142-144). Alternatively, the inhibition of CARTS pathway may hinder the transport of other essential proteins necessary for invadopodia formation and/or maturation such as formins. To address this possibility, additional analysis of whether these proteins are packaged within the CARTS vesicles must be further explored.

In this study, we illustrate the involvement of the CARTS pathway in a pathologically relevant model system of protease dependent invasion of cancer cells. These findings provide the necessary framework to investigate other unknown molecules that are potentially responsible for activation of MT1-MMP by exploring other whose proteins transport pathway intersects with CARTS.

3.6. Acknowledgements

AA acknowledges the support from ARCS foundation and the Ruth L. Kirschstein National Research Service Award NIH/NHLBI T32 HL 105373.

Chapter 3, in full, is currently being prepared for submission for publication of the material. “MT1-MMP trafficking in protease dependent invasion of cancer cells utilizes CARTS secretory pathway”. Aung, Aereas; Shih, Yu-Ru V.; Wakana, Yuichi; Malhotra, Vivek; Jamora, Colin; Varghese, Shyni. The dissertation author is the primary investigator and author of this material.

3.7. Conclusion

Cancer cell invading into Matrigel networks utilize protease dependent mode of migration. During this process, cancer cells employ CARTS pathway to transport MT1-MMP from the cell cytoplasm to the cell surface. Our data indicates that beyond an invasion depth of 2 µm, MT1-MMP is packaged within CARTs vesicle along with a known CARTS cargo, PAUF. We have shown the transport of MT1-MMP to the cell surface by monitoring the secretion of PAUF as a function of invasion depth. In addition, the disruption of the CARTS vesicle formation via inhibition of protein kinase D decreased the invasion depth of cancer cells. Similarly, down regulation of Eg5, kinesin motor shown to transport CARTS vesicles, and TGN46, a marker for CARTS vesicle, impeded the invasion of cancer cells into the Matrigel network. Moreover, we demonstrate the loss of invadopodia-like protrusions amongst cancer cells when CARTs pathway was disrupted.

3.7. Figures

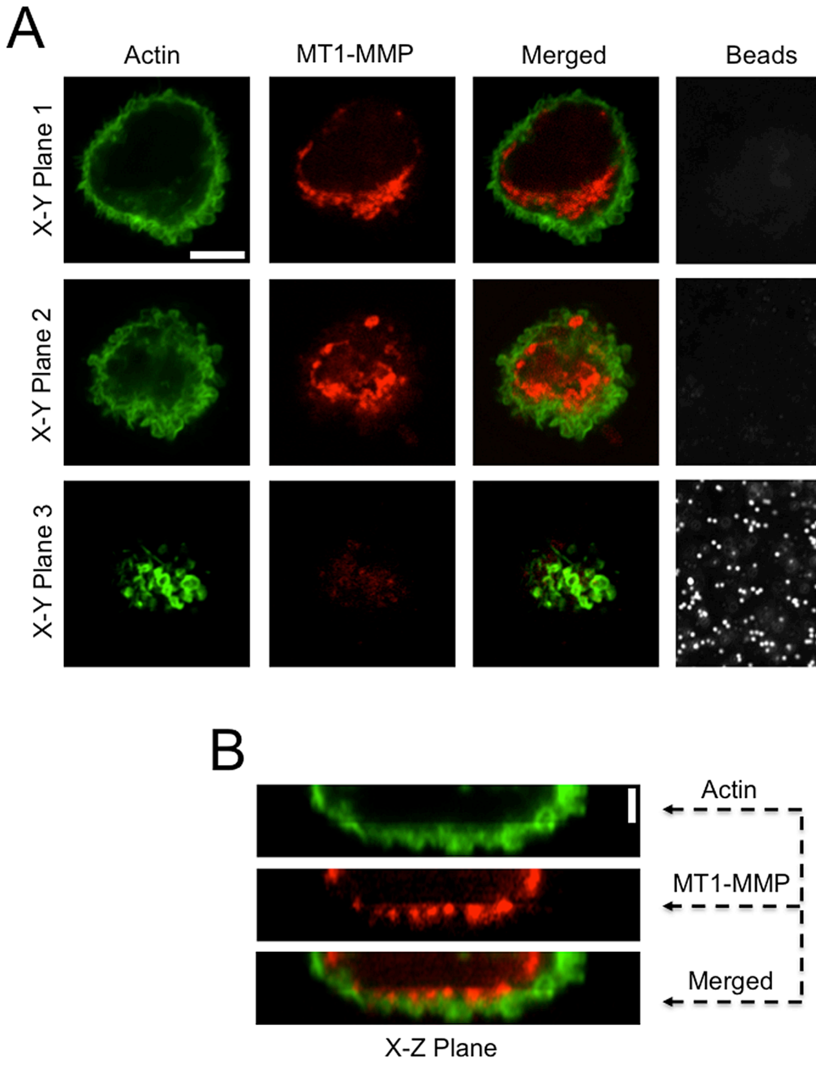

Figure 3.1: Protease independent invasion of MDA-MB-231 cells into 30 μm thick Matrigel networks.

(A) Confocal z-section images of an immunofluorescently stained cancer cell at invasion depths (h_{inv}) of less than 2 μm. Each row shows the X-Y planes of actin (green), MT1-MMP (red), merged images, and fluorescent particles embedded within the Matrigel (white). The z section images are shown from the mid-section to the leading edge of the cell as X-Y plane 1 approaches plane 3. (B) Corresponding X-Z plane reconstructed from confocal z-stack images. Both horizontal and vertical scale bar represent 10 μm.

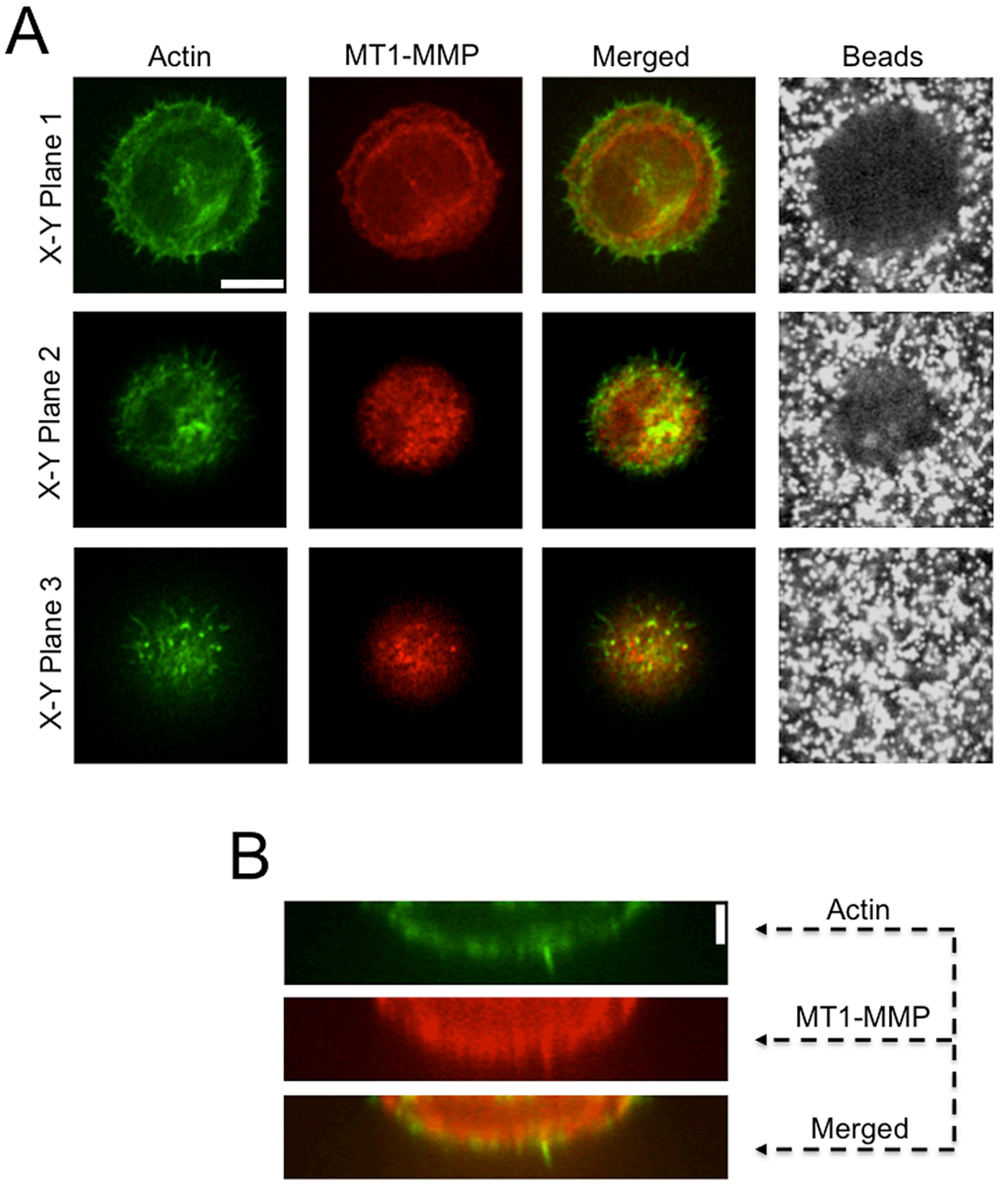

Figure 3.2: Protease dependent invasion of MDA-MB-231 cells into 30 μm thick Matrigel networks.

(A) Confocal z-section images of an immunofluorescently stained cancer cell at invasion depths (h_{inv}) of greater than 4 μm. Each row shows the X-Y planes of actin (green), MT1-MMP (red), merged images, and fluorescent particles embedded within the Matrigel (white). The z section images are shown from the mid-section to the leading edge of the cell as X-Y plane 1 approaches plane 3. (B) Corresponding X-Z plane reconstructed from confocal z-stack images. Both horizontal and vertical scale bar represent 10 μm.

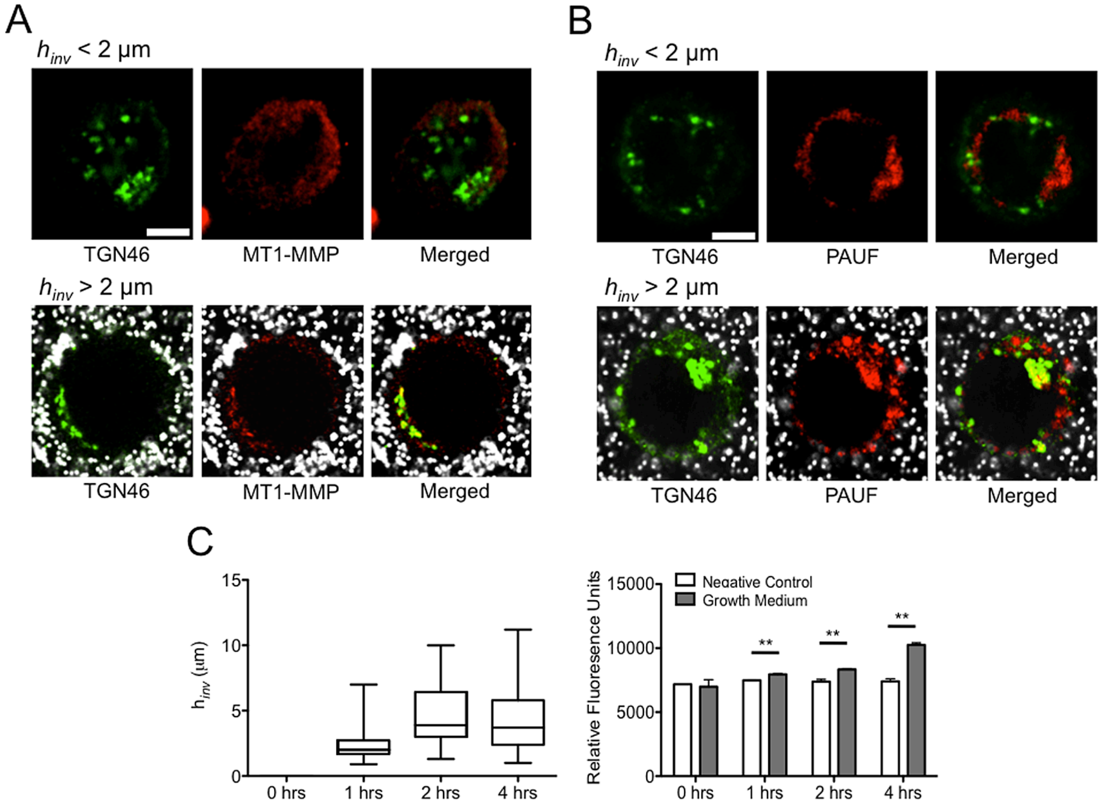

Figure 3.3: MT1-MMP transport through CARTS pathway during MDA-MB-231 cell invasion.

(A) Immunofluorescent staining for TGN46 (green) and MTI-MMP (red) of cancer cell invading into a 30 μm thick Matrigel network for $h_{inv} < 2$ μm (top panel) and $h_{inv} < 4$ μm (bottom panel). (B) Immunofluorescent staining for TGN46 (green) and PAUF (red) of cancer cell invading into a 30 μm thick Matrigel network for $h_{inv} < 2$ μm (top panel) and $h_{inv} < 4$ μm (bottom panel). Scale bars: 10 μm. (C) Effect of the extent of cell invasion (left panel) on mRFP-PAUF secretion (right panel) shows an increase in PAUF secretion with increasing invasion depth. Negative control and growth medium indicate media collected from acellular Matrigel and RFP-PAUF transfected cells invading into 30 μm thick Matrigel, respectively. ** denotes statistical significance between negative control and growth medium ($p < 0.005$) calculated based on t-test.

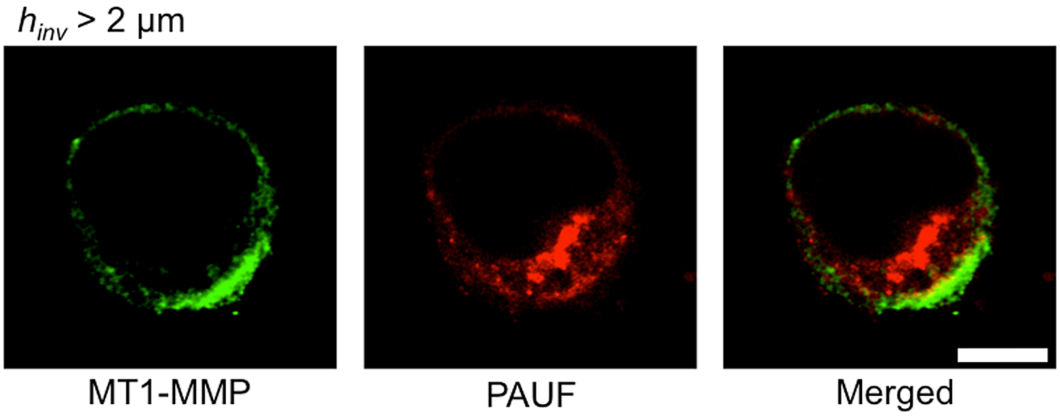

Figure 3.4: Colocalization of MT1-MMP and PAUF within MDA-MB-231 cells invading into 30 µm thick Matrigel network.

Confocal images of a representative cell invading into Matrigel network display colocalization of MT1-MMP (green) with PAUF (red) at h_{inv} < 4 µm. Scale bar: 10 µm.

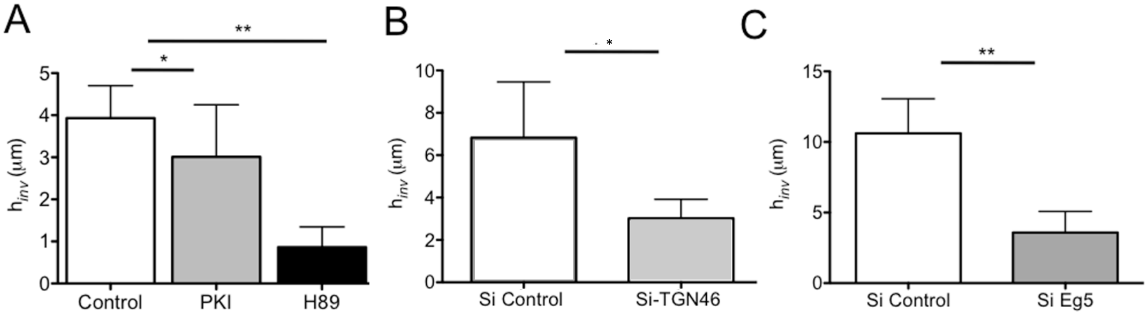

Figure 3.5: CARTS inhibition abrogates MDA-MB-231 invasion into 30 μm thick Matrigel network.

(A) Protein Kinase D (H89) inhibitor impedes the invasion of cancer cells into the Matrigel network while that of Protein Kinase A (PKI) have no significant effect on cell invasion under identical culture conditions. Stars denote statistical significance amongst groups (* and ** denotes $p < 0.05$ and $p < 0.005$, respectively) calculated based on one way analysis of variance (ANOVA) followed by Bonferroni post-test. Inhibition of TGN46 (B) and Eg5 (C) via Si-RNA also impairs the invasion of cancer cells into the Matrigel network. * and ** denotes $p < 0.05$ and $p < 0.005$, respectively, for statistical significance calculated from t-test.

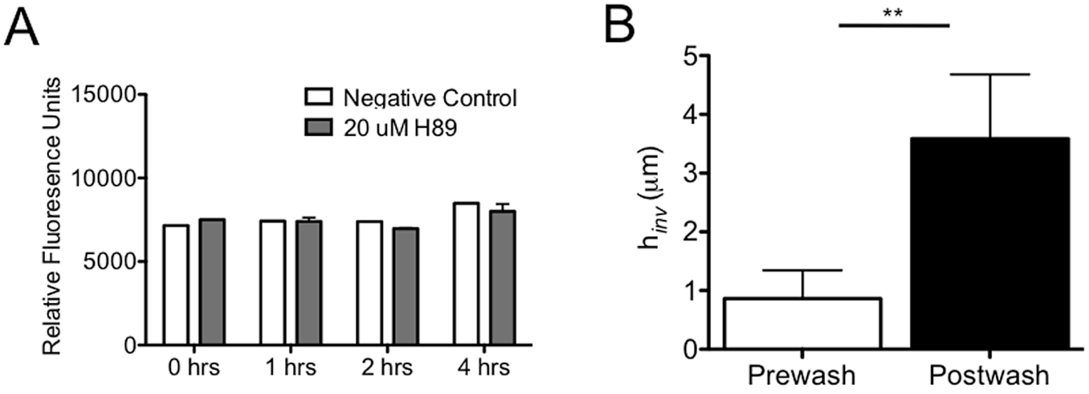

Figure 3.6: Effect of H89 on MDA-MB-231 cell invasion.

(A) Treatment with 20 µM H89 impedes the secretion of PAUF during invasion into 30 µm thick Matrigel. Negative control and 20 µM H89 indicate media collected from acellular Matrigel incubated with 20 µM H89 and RFP-PAUF transfected cells invading in the presence of 20 µM H89, respectively. (B) Invasion of cancer cells into 30 µm thick Matrigel can be reinstated upon removal of H89 indicating reversibility of the inhibitor.

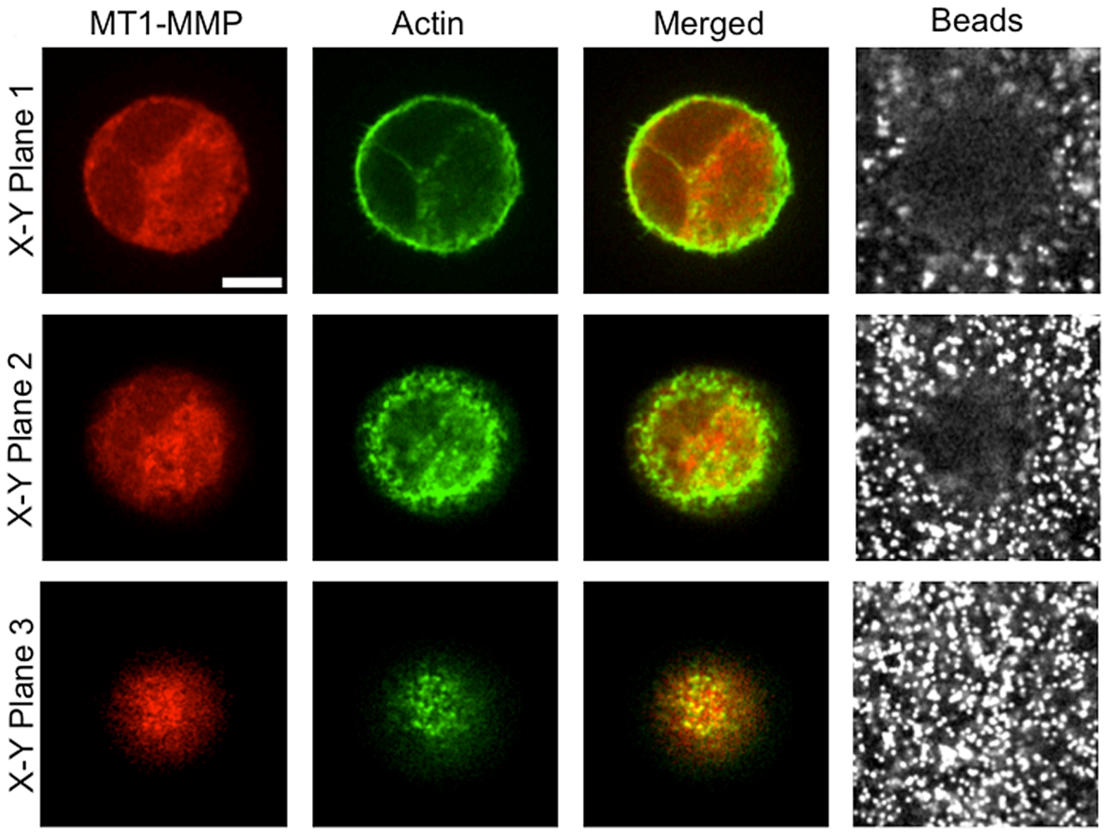

Figure 3.5: Downregulation of TGN46 inhibits the formation of invadopodia-like protrusions in MDA-MB-231 cells.

Confocal sections of immunofluorescently stained cancer cells treated with Si-TGN46 invading into a 30 μm thick Matrigel network. Each row shows the X-Y planes of actin (green), MT1-MMP (red), merged images, and embedded particles (white). The z section images are shown from the mid-section to the leading edge of the cell as X-Y plane 1 approaches plane 3. Scale bar: 10 μm.

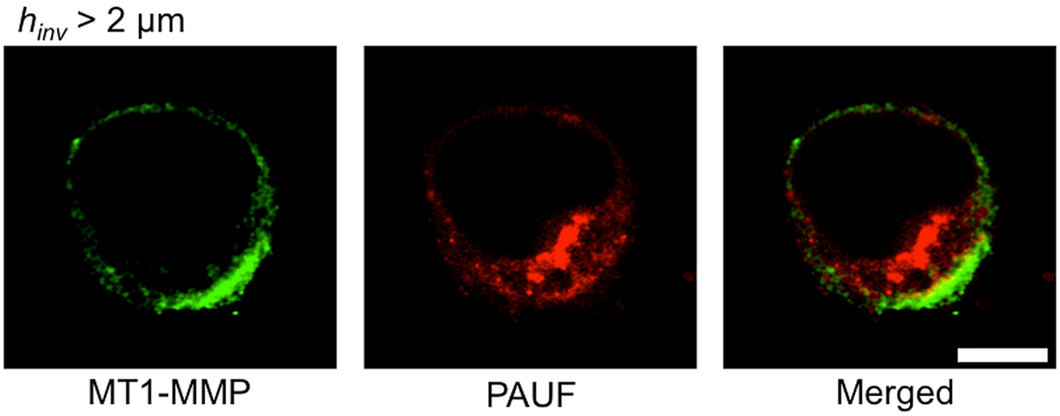

Figure 3.6: Colocalization of MT1-MMP and PAUF within MDA-MB-231 cells invading into 30 µm thick Matrigel network.

Confocal images of a representative cell invading into Matrigel network display colocalization of MT1-MMP (green) with PAUF (red) at $h_{inv} < 4$ µm. Scale bar: 10 µm.

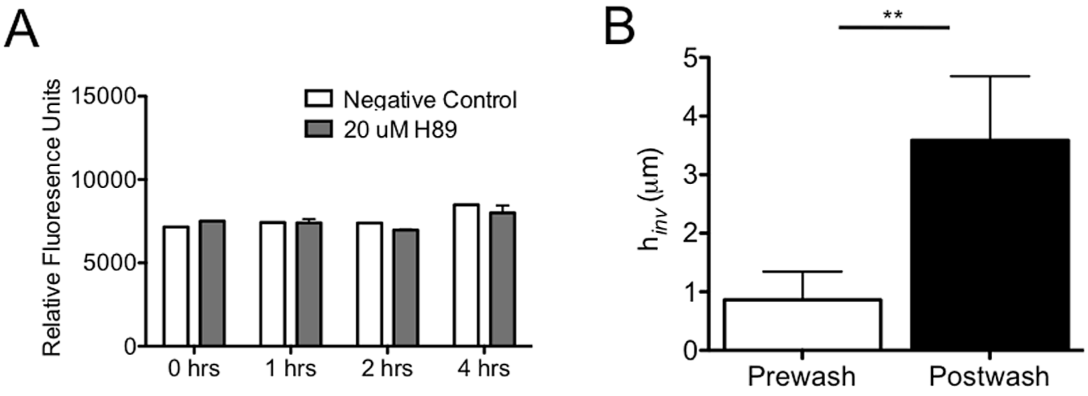

Figure 3.7: Effect of H89 on MDA-MB-231 cell invasion.

(A) Treatment with 20 µM H89 impedes the secretion of PAUF during invasion into 30 µm thick Matrigel. Negative control and 20 µM H89 indicate media collected from acellular Matrigel incubated with 20 µM H89 and RFP-PAUF transfected cells invading in the presence of 20 µM H89, respectively. (B) Invasion of cancer cells into 30 µm thick Matrigel can be reinstated upon removal of H89 indicating reversibility of the inhibitor.

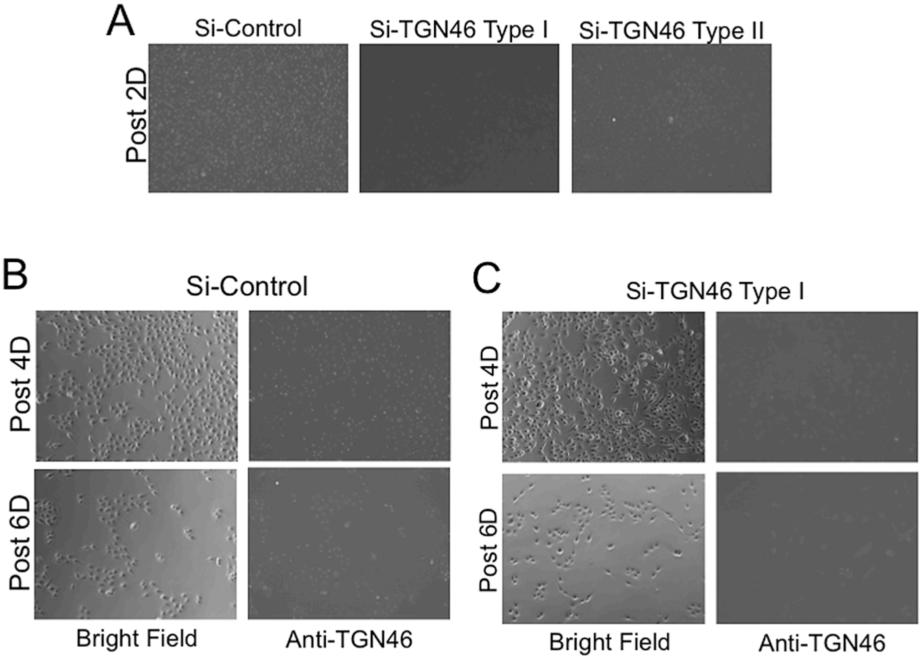

Figure 3.7: Validation of TGN46 downregulation in MDA-MB-231 subsequent to Si-RNA treatment.

(A) Bright field and fluorescent images of MDA-MB-231 cells immunostained for TGN46 post 2 days after treatment with Sham Si-RNA (Si-Control), Si-TGN 46 Type I, and Si-TGN46 Type II. The fluorescent images indicate that Si-TGN46 Type I achieves the highest downregulation. Therefore, Si-TGN46 Type I was only used within the study and it is referred to as Si-TGN46 within the text. Time dependent downregulation of TGN46 post 4 and 6 days treatment of cells with Si-Control (B) and Si-TGN46 (C). Scale Bar: 50 µm. (D) Invasion of MDA-MB-231 cells into 30 µm thick Matrigel post 4 days after treatment with Si-TGN46. * denotes statistical significance of $p < 0.05$ calculated from t-test.

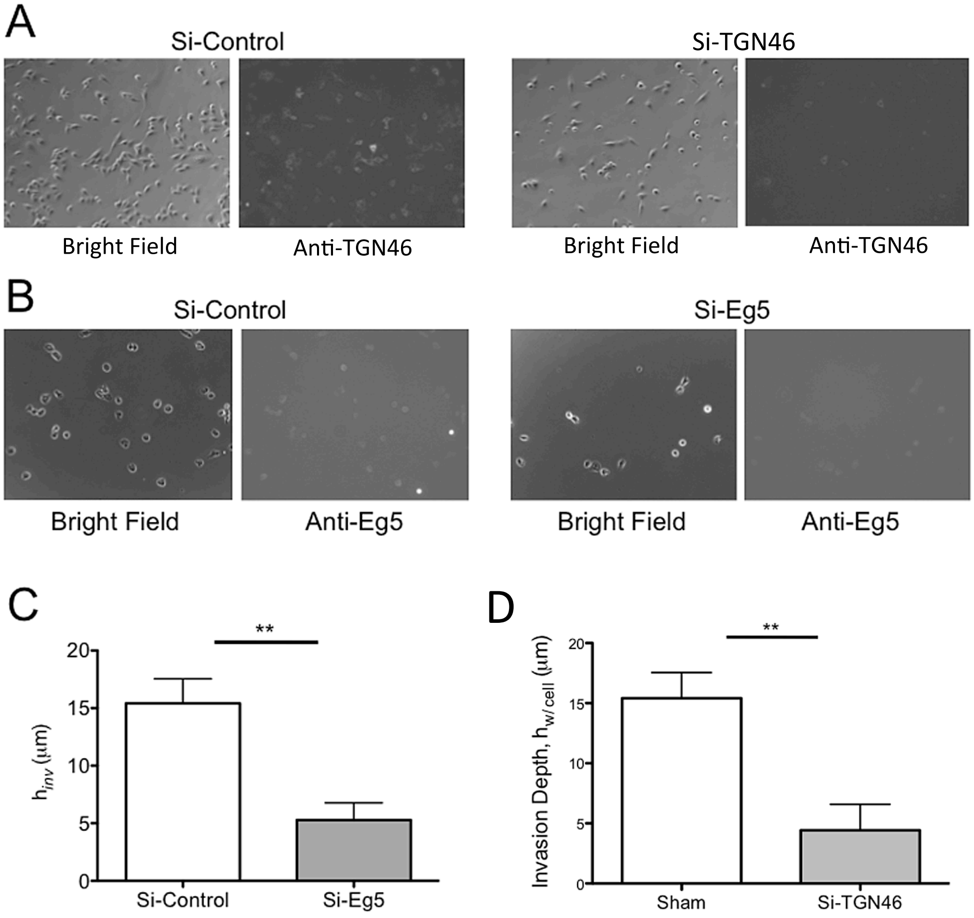

Figure 3.8: Validation of TGN46 downregulation in PC3 subsequent to Si-RNA treatment.

(A) Bright field and fluorescent images of PC3 cells immunostained for TGN46 post 2 days after treatment with Si-Control and Si-TGN46. Scale Bar: 50 µm. (B) Downregulation of TGN46 impairs the invasion of PC3 cells into 30 µm thick Matrigel post 2 days after treatment. ** denotes statistical significance of $p < 0.005$ calculated from t-test.

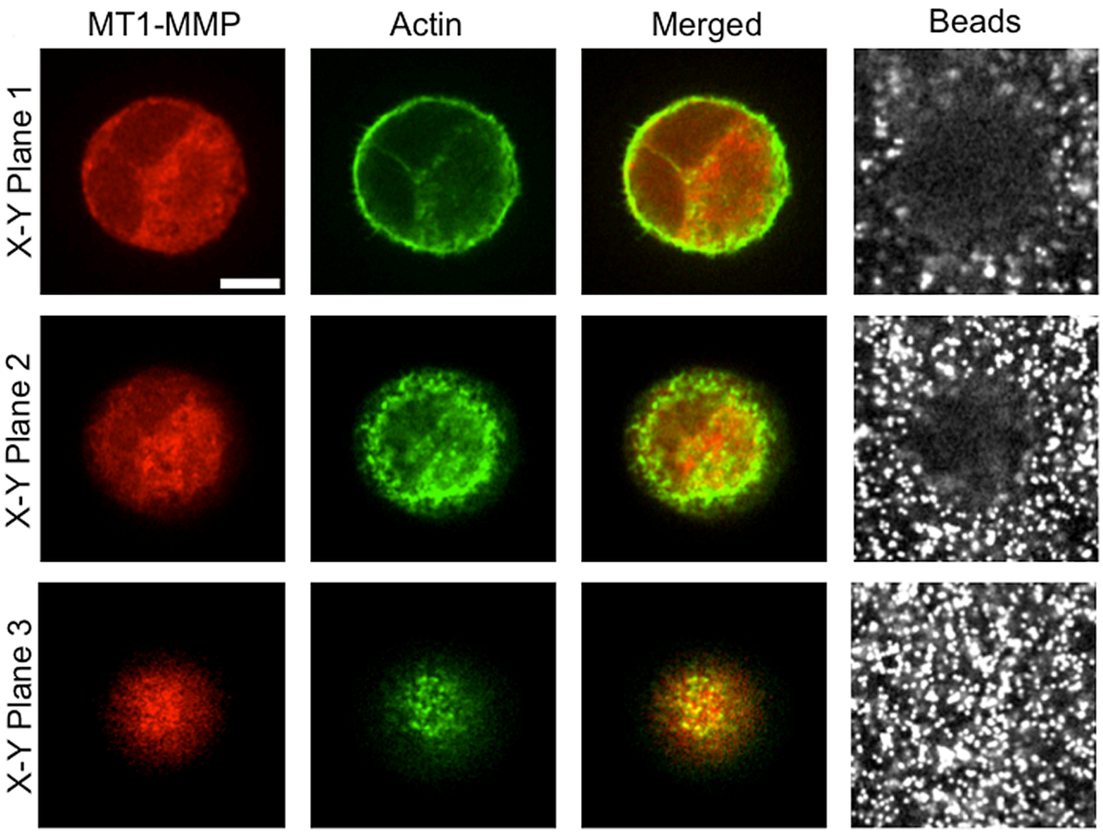

Figure 3.9: Downregulation of TGN46 inhibits the formation of invadopodia-like protrusions in MDA-MB-231 cells.

Confocal sections of immunofluorescently stained cancer cells treated with Si-TGN46 invading into a 30 μm thick Matrigel network. Each row shows the X-Y planes of actin (green), MT1-MMP (red), merged images, and embedded particles (white). The z section images are shown from the mid-section to the leading edge of the cell as X-Y plane 1 approaches plane 3. Scale bar: 10 μm.

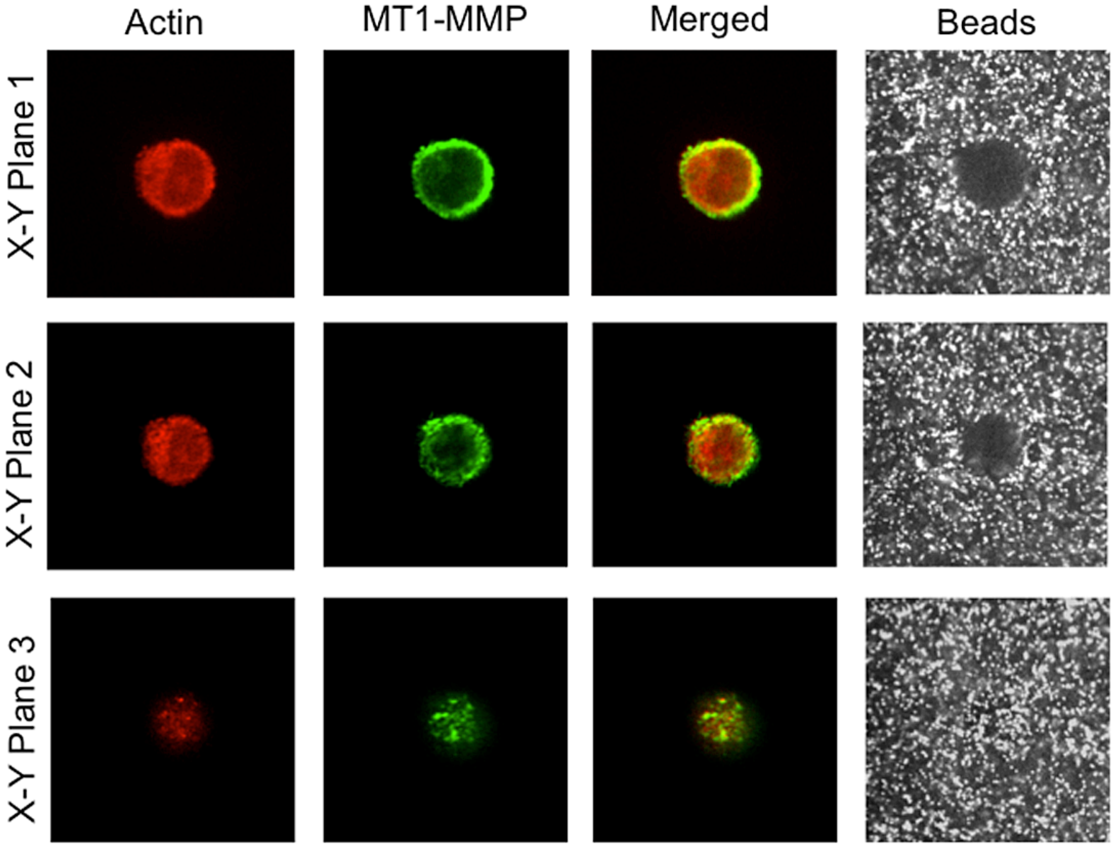

Figure 3.10: Downregulation of Eg5 inhibits the formation of invadopodia-like protrusions in MDA-MB-231 cells.

Confocal sections of immunofluorescently stained cancer cells treated with Si-TGN46 invading into a 30 μm thick Matrigel network. Each row shows the X-Y planes of actin (green), MT1-MMP (red), merged images, and embedded particles (white). The z section images are shown from the mid-section to the leading edge of the cell as X-Y plane 1 approaches plane 3. Scale bar: 10 μm.

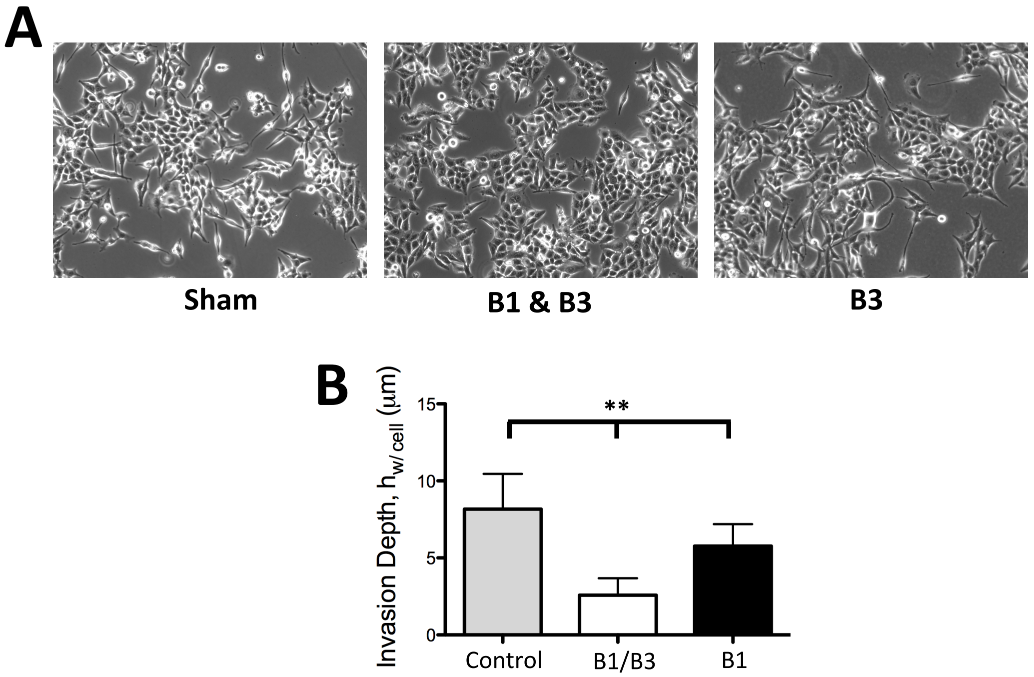

Figure 3.11: Down regulation of β1 and β3 integrin abrogates cancer cell invasion.

(A) Bright field images of MDA-MB-231 transfected with control and si-RNA for β1 and/or β3 integrin. (B) Quantification of invasion depth into Matrigel network for cells treated with control, β1 integrin alone, and both β1 and β3 integrin.

Chapter 4: Chemotaxis-driven assembly of endothelial barrier in a tumor-on-a-chip platform

4.1. Abstract

The integration of three-dimensional micropatterning with microfluidics provides a unique opportunity to create perfusable tissue constructs *in vitro*. Herein, we have used this approach to create a tumor-on-chip with endothelial barrier. Specifically, we photopatterned a mixture of endothelial cells and cancer spheroids within a gelatin methacrylate (GelMA) hydrogel inside of a microfluidic device. The differential motility of endothelial and cancer cells in response to a controlled morphogen gradient across the cell-laden network drove the migration of endothelial cells to the periphery while maintaining the cancer cells within the interior of the hydrogel. The resultant endothelial cell layer forming cell-cell contact via VE-Cadherin junctions was found to encompass the entire the GelMA hydrogel structure. Furthermore, we have also examined the potential of such tumor-on-a-chip system as a drug screening platform using Doxorubicin, a model cancer drug.

4.2. Introduction

According to the American Cancer Society, cancer is the second leading cause of death in the United States where one in four deaths in 2015 were cancer-related (1). Despite such grim outlooks, survival rate amongst cancer patients has steadily increased from 49% to 68% over the past decade due to the increase in our fundamental understanding of this disease and technological advances (1). Some of these technological advances include the development of three-dimensional (3D) *in vitro* models recapitulating various complexities of the disease. For instance, multicellular tumor spheroids, consisting of cancer cells or multiple cell types, have been developed to study cancer progression and drug efficacy (40, 41, 145-148). Other efforts in the area include encapsulation of tumor spheroids within biomaterials to mimic the extracellular matrix environment (149-152). 3D *in vitro* systems incorporating stromal and vascular cells have also been developed (153-155). In a recent study, George and colleagues have created vascularized tumor spheroids where the endothelial cells incorporated within the spheroids formed vascular networks in presence of stromal fibroblasts (45).

The integration of 3D cell cultures with microfluidics technology can be used to create tumor models with perfusion to facilitate mass transport (156), (82). Such microfluidic devices have been used to study various aspects of cancer progression such as tumor growth, presence of high interstitial fluid pressure, and cancer cell extravasation (38, 42, 48, 49, 157-159). Such technological platforms have also been used to understand drug-tumor interactions such as drug specificity, penetration into cancer spheroids, and efficacy towards repressing cancer growth (42, 49, 160, 161). Many of these platforms employ multi-layered or multi-channel devices to create a perfused tumor-a-on-chip system (48, 158, 160). Generation of such integrative fluidic system often requires multiple steps and complex fabrication processes.

In this study, we describe a novel yet simple approach to create a tumor-on-a-chip (TOC) device that contains tumor spheroids within an artificial extracellular matrix surrounded by a single-celled endothelial barrier that is assembled through vascular endothelial (VE)-cadherin junctions. Specifically, cancer spheroids along with human umbilical vein endothelial cells (HUVECs) were confined within gelatin methacrylate (GelMA) hydrogel structures through 3D photopatterning and integrated into a microfluidic device (162). The differential motility of cancer spheroids and endothelial cells in response to chemotactic gradients generated within the 3D environment was harnessed to drive the migration of endothelial cells to the periphery to form a barrier surrounding the cell-laden GelMA structures. We further validated the potential of this tumor-on-a-chip device as a drug-screening platform by using Doxorubicin, a commonly used anti-cancer drug, as a model compound.

4.3 Materials and Methods

4.3.1. Cell culture

MCF7 and HUVECs were obtained from ATCC. MCF7 cells were cultured in growth media (GM) comprised of Dulbecco Modified Eagle’s high glucose media (Hyclone), 10% fetal bovine serum (FBS, Gibco), and 1% Penicillin/Streptomycin (Gibco). HUVECs were cultured in HUVEC Media (HM) containing 79% M199 media

(Gibco), 10% FBS (Gibco), 10% endothelial cell growth media (Cell Application, Inc.), and 1% Penicillin/Streptomycin. HUVECs used in this study were limited to cells between passage 6 and 8.

4.3.2 MCF7 Spheroid Formation

MCF7 cells were cultured to about 80% confluency prior to trypsinization. To create spheroids, 1 million MCF7 cells in 4 mL GM were plated in a 60 mm diameter petri dish and cultured on an orbital shaker (VWR, Model No. DS-500E) at 45 rpm in a humidified incubator maintained at 37 °C and 5% CO_2. The cultures were maintained for ~20 hours to form spheroids. The average diameter of the spheroids were found to be ~200 μm.

4.3.3. Fabrication of Silicon Mold

Micropatterned silicon molds were fabricated according to the protocol as described previously(163). In brief, microfluidic channels were photolithographically defined using NR9-1500PY negative photoresist (Futurrex, Frankling, NJ, USA) on a 4-inch diameter Si wafer. The Si wafer with the photoresist defined was then etched using the deep reactive ion etching (DRIE) process. In the DRIE process, SF6 gas was flowed at 100 sccm throughout the 11 seconds of reaction time, followed by a passivation cycle when C4F8 gas was flowed at 80 sccm for 7 s. A 75 μm of etching depth was achieved under the etching rate of about 0.7 μm per cycle. After the DRIE process, the NR9-1500PY photoresist was removed by immersing in acetone for 4 hours before rinsing with methanol, isopropanol, and deionized water. The Si mold was then dried under compressed nitrogen gas and silanized by vapor deposition of trichlorosilane (TCI Inc, Portland, OR, USA) to facilitate PDMS molding and removal.

4.3.4. Synthesis of lithium phenyl-2,4,6-trimethylbenzoylphosphinate (LAP) as a photoinitiator

First, 2,4,6-trimethylbenzoyl chloride was added drop wise to an equal molar quantity of dimethyl phenylphosphonite under argon while stirring at room temperature(164). This mixture was allowed to react for 18 hours. Next, the temperature of the reaction mixture was increased to 50 °C while 4 molar excess of lithium bromide mixed with 2-butanone was added to the reaction mixture. resulting in precipitation to form within 10 minutes. After precipitation, the temperature was cooled to room temperature and allowed to rest for 4 hours. Next, to ensure complete removal of excess lithium bromide, the precipitate was collected by filtration and washed three times using 2-butanone. Finally, the product was dried using a vacuum to remove excess 2-butanone, yielding LAP.

4.3.5. Synthesis of Gelatin Methacrylate (GelMA)

Gelatin was methacrylated in accordance with the protocol described elsewhere (165, 166). In brief, 10g of bovine skin gelatin (Sigma Aldrich, St. Louis, MO, USA) was dissolved in 100 mL of PBS and stirred at 60 °C for roughly 1 hour to achieve complete solvation. Next the solution was lowered to 50°C, after which, 8mL of methacrylic anhydride (cat no.: 276685; Sigma Aldrich) was added to the solution drop wise with vigorous stirring. The solution was kept at 50°C with vigorous stirring for an hour after the addition was complete, after which, it is quenched with 2x the volume of PBS (200 mL). The solution was then dialyzed against milliQ water using 12–14 kDa cutoff dialysis tubing (Spectrum Laboratories, Rancho Dominguez, CA, USA) for one week (3 times per day water change) at 40 °C to remove trace contaminants. Next, the GelMA solution was frozen in liquid nitrogen and lyophilized in a freeze dryer for 4 days before being stored at −20 °C until usage.

4.3.6. Fabrication of Tumor-on-a-Chip Device

The tumor-on-a-chip device was fabricated with slight modifications of a device described previously(163). The device includes a trilayer hydrogel system where cell-laden GelMA hydrogels were sandwiched between two polyacrylamide (PAm) hydrogels. The fabrication of the device involves the following steps:

Methacrylation of glass surfaces: To achieve the chemical tethering of PAm hydrogels, glass coverslips were methacrylated as described elsewhere (162, 163). Briefly, glass coverslips were cleaned with 1.5 M NaOH for 30 minutes followed by rinsing with DI water and drying with air. The cleaned coverslips were treated with 2% (v/v) 3-(Trimethoxysilyl)propyl methacrylate solution diluted in 0.54% glacial acetic acid and 99.46% ethanol for 5 minutes at room temperature to immobilize methacrylate groups onto the surfaces. Care was taken to aliquot sufficient volume of the reacting solution onto the coverslips to eliminate artifacts associated with their evaporation. The surface modified coverslips were washed with pure ethanol for 10 minutes under gentle stirring to remove excess reactants. The above step was repeated twice, rinsed with DI water, and dried at 50 °C for 30 minutes. The coverslips were used immediately.

Trilayer hydrogel formation: Methacrylated coverslips of 22x60 mm rectangular and 12 mm diameter were used. 3 μL of a polyacrylamide hydrogel precursor solution comprised of 5% (w/v) acrylamide (Am), 0.2% (w/v) Bis-Acrylamide (BisAm), 0.1% (w/v) Ammonium Persulfate (APS), and 0.01% (w/v) *N*,*N*,*N'*,*N'*-Tetramethylethylenediamine (Sigma-Aldrich) in PBS, was placed in the center of the methacrylated 22x60 mm rectangular coverslip and the droplet was covered with a non-methacrylated 15 mm diameter coverslip. This would result in the bottom layer of the device (Fig. 4.1A, B). This process was repeated with a methacrylated 15mm circular coverslip and non-methacrylated square coverslip to fabricate the top layer (Fig. 4.1A**,** B). The precursor solution was left to polymerize for 20 minutes prior to gently removing the non-methacrylated coverslips. The resulting structures containing PAm hydrogels tethered to the circular and rectangular coverslips were allowed to equilibrate in PBS overnight at room temperature to remove trace amounts of unreacted monomers.

Around 5 μL of DI water was placed onto a circular region of the fabricated silicon mold before covering the droplet with PAm hydrogel tethered-15 mm diameter circular coverslip (Fig. 4.1C). Polydimethylsiloxane (PDMS, Sylgard 184) base solution was mixed with its curing agent at a weight ratio of 10:1 and degassed to remove air bubbles if any (Fig. 4.1D). This mixture was gently poured onto the silicon wafer containing the PAm hydrogel and baked at 60 °C for 2 hours (Fig. 4.1E). The PDMS mold containing the hydrogel was detached from the silicon wafer and bonded to the rectangular coverslips containing a PAm hydrogel using UV-Ozone treatment (Fig. 4.1F). Care was taken to prevent direct exposure of the PAm hydrogel to deep UV.

The PDMS mold and the glass coverslips were immediately attached to each other while maintaining the alignment between the hydrogels on their respective surfaces. This ensures that the top and bottom of the microfluidics chamber are comprised of PAm hydrogels. The fabrication process was completed by bonding the PDMS mold and glass coverslips at 60 °C. The device was equilibrated in PBS and UV sterilized for 45 minutes prior to using it for cell culture.

Preparation of GelMA solution: Gelatin methacrylate was dissolved in PBS to achieve a 10% wt/v precursor solution. To ensure complete dissolution, the GelMA dispersed PBS was incubated at 60 °C in a water bath for 20 minutes. The GelMA solution was syringe filtered (pore size of 0.22 μm) to remove any insoluble residues and maintained at 37 °C until use.

Encapsulation of cells within GelMA structures in microfluidic device: HUVECs and MCF7 spheroids were encapsulated within GelMA hydrogels. The MCF spheroids were passed through a cell strainer having 100 μm pore size (Corning) to eliminate single cells and small spheroids. Around 50 spheroids with a diameter of ~ 200 μm were dispersed in 5 mL of PBS containing 2 million HUVEC cells. The mixture was centrifuged for 3 minutes at 800 rpm. The supernatant was aspirated and 100 μL of 10% GelMA solution was added to the cell pellet. The cells were resuspended gently using a pipette before the addition of 0.01% ascorbic acid (antioxidant) and 2 μM LAP (photoinitiator) to the solution. This solution was again mixed gently, drawn into a syringe, and injected into the microfluidic device (Fig. 4.1G).

This device was placed onto a transparency film photomask containing an ellipse pattern and mounted onto a microscope stage (Fig. 4.1H-I). Using the stage controller of the microscope, the position of the fluidic device was moved to locate individual MCF7 spheroids surrounded by HUVECs under brightfield illumination. Each location was exposed to UV light with an excitation and emission wavelengths of approximately 358 and 463 nm, respectively, for 18 seconds. Several locations were photopolymerized before flushing the device with PBS containing 4% Penicillin/Streptomycin. Mixed Media (MM) containing 50% GM and 50% HM was subsequently injected into the device and the GelMA structures containing MCF7 spheroids and HUVECs were cultured at 37 °C and 10% CO_2.

4.3.7. Quantification of cell motility within the cell-laden GelMA hydrogel structures

The motility of HUVEC cells and MCF7 spheroids was determined by examining the changes in their local cell density within the GelMA hydrogel as a function of culture time. Brightfield images of the cell-laden GelMA hydrogels were taken for up to 5 days. A custom Matlab software was used to process the brightfield images of the cell-laden GelMA hydrogel by identifying the boundary of the hydrogel structure and partitioning it into smaller zones of Z1 to Z6 as indicated in Figure 4.2B inset. In order to partition the structure into smaller zones, a Sobel filter was applied to the bright field image of the cell-laden GelMA hydrogel to identify its boundaries. High-pass filter was applied to remove random non-zero values outside the GelMA hydrogel structure. A distance transform was applied to the filtered image resulting in small and large values within the interior and exterior of the ellipse GelMA hydrogel, respectively. The ellipse structure of the cell-laden GelMA hydrogel was identified by applying a low-pass filter onto the distance transform image and converting the filtered results into a binary image. Finally, a built-in Matlab function, Regionprops, was used to identify the centroid, major, and minor axes lengths of the ellipse hydrogel structures. We further created smaller ellipses by reducing the major and minor axes of the outer ellipse structure to create multiple zones as in Fig. 4.2C.

The local cell density was obtained by counting the number of cells divided by the area of each zone. Zone 6 was excluded from all analysis since the number of cells at the perimeter of the ellipse cannot be accurately counted. For quantifying the flow-rate dependent migration of cells in Figure 4.3B, zones 1 through 5 were merged to form a single area.

4.3.8. Quantification of MCF7 spheroids growth within GelMA hydrogel structures

Brightfield images of the GelMA hydrogels containing the spheroids and HUVECs were recorded as a function of culture time (1-5 days) to examine their growth post-encapsulation. The area of the spheroid was quantified by tracing the boundary of the spheroid using the free-hand selection tool on ImageJ.

4.3.9. FITC-Dextran diffusion into cell-laden GelMA hydrogel

GelMA hydrogels containing MCF7 spheroids and endothelial cells were cultured within our microfluidics device for 4 days in MM. PBS containing 10 μg/mL 10 kDa Dextran (Sigma-Aldrich) or 100 μg/mL 150 kDa Dextran was introduced into the device and the diffusion of these molecules into the GelMA hydrogels was monitored by recording the epi-fluoresence images at specified time intervals for 30 minutes. Prior to post processing, the fluorescence intensity within the hydrogel was normalized to the mean intensity outside of the hydrogel. This normalized intensity was used in all of the analysis. To quantify the diffusion process, the intensity of the normalized fluorescent signal at the central region of the ellipse was used for both the time plots and steady state analysis. The central region consist of a small "zone 1" ellipse as shown in Figure 4.2B. The region within this small ellipse that overlaps with the cancer spheroid was excluded from the analysis.

4.3.10. Immunofluorescence staining of HUVECs

Cells within the device were fixed in 10% Paraformaldehyde (PFA) solution for 10 minutes at room temperature followed by infusing the device with PBS to remove the excess PFA. Blocking buffer, comprised of 0.1% Triton-X100 and 3% Bovine Serum Albumin (BSA), was added and the cells were incubated in this solution for 30 minutes at room temperature. The device was washed with PBS after each step to remove the residual solutions. The fixed cells were treated overnight with rabbit polyclonal VE-Cadherin antibody (Cat. No. D87F2, Cell Signaling) diluted in blocking buffer at 4 °C. The primary antibody solution was removed by washing with PBS. The device was incubated in blocking buffer containing Alexafluor 488 goat anti-rabbit secondary antibody (Cat. No. A-11008, ThermoFisher Scientific) and Rhodamine-conjugated Phalloidin (Cat. No. R415, ThermoFisher Scientific) for 70 minutes at room temperature. The cells were subsequently washed with PBS and stained with 20 μg/mL DAPI solution for 20 minutes to visualize the nuclei. The device was rinsed several times with PBS and imaged using a confocal microscope.

4.3.11. Doxorubicin solution

Doxorubicin (Cat. No. D1515, Sigma-Aldrich) was weighed and dissolved in DMSO to achieve a concentration of 100 mg/mL. This solutions was distributed into small aliquots and stored in -20 °C. The stock solution was thawed and diluted to 100 μg/mL in prewarmed MM (~ 37 °C) and sterilized using a DMSO-resistant syringe filter (Pall Corporations). This 100 μg/mL solution was further diluted in MM to acquire doxorubicin concentrations of 1 and 10 μg/mL used in the study.

4.3.12. Penetration of Doxorubicin into spheroid-laden GelMA structures

The cell-laden GelMA hydrogels were exposed to MM containing 1, 10, and 100 μg/mL Doxorubicin. The presence of Doxorubicin within the spheroids was detected using a Zeiss Observer A1 Microscope with a 10x A-Plan lens after 3 days of incubation on the red fluorescent channel. An exposure time of 700 ms was used for all samples.

4.3.13. Confocal microscopy for imaging immunofluorescently stained cells

Laser scanning confocal microscope was used to obtain Z-stack images of cells stained for nuclei, F-Actin, and VE-Cadherin as well as for the PAm hydrogels embedded with fluorescent beads. A vertical step size of 1 μm was used to acquire the Z-stack images.

4.3.14. Effect of flow rates on mechanical compression of the GelMA hydrogels

To determine whether the GelMA structures are differentially compressed at different flow rates, acellular structures containing 2% (v/v) fluorescent beads of 200 nm diameter (Cat. No. F8782, ThermoFisher Scientific) were used. The fluorescent bead laden-GelMA hydrogels were perfused with MM and allowed to equilibrate for 6 hours at 37 °C. The equilibrated structures were subjected to different flow rates of 10, 20, 40, and 1000 μL/hr. The X-Y images of the hydrogels subjected to different flow rates at 37 °C were acquired by using a spinning disk confocal microscope. The reference state was generated by recording the X-Y section of the ellipse hydrogel structure at a z-position that bisects the top and bottom of the chamber in the absence of any flow. The samples were then exposed to different flow rates and the X-Y images were recorded at the same z-position that was used for the reference state. The 2-D displacement fields, u and v, were obtained by comparing the reference image to the images recorded under different flow rates using Particle Image Velocimetry (PIV). The area strain, A_{strain}, was calculated by using the following equation:

$$A_{strain} = \frac{\partial u}{\partial x} + \frac{\partial v}{\partial y} \qquad \textbf{(Eq. 7)}$$

4.3.15. Modeling of mass transfer within the cell-laden GelMA hydrogel structures

COMSOL Version 4.2 was used to solve the 2-D diffusion-reaction equation (**Eq. 1, 6**) with a convective boundary condition (**Eq. 3**). The domain of the system was comprised of an ellipse structure with major and minor axes lengths of 1.2 and 0.45 mm, respectively.

4.4. Results

4.4.1. Formation and characterization of trilayer hydrogel-based device

GelMA hydrogels were photopatterned within a microfluidics device to achieve an ellipse structure with major and minor axes lengths of 1.2 mm and 0.45 mm, respectively. A X-Z confocal section of the fluidic chamber depicts a structure embedded with green fluorescent particles sandwiched between two PAm hydrogels containing far red particles (Fig. 4.4A). The non-adhesive PAm hydrogels were used to eliminate the adhesion (if any) of the encapsulated cells to the surfaces outside GelMA structures. The X-Y confocal sections showed the presence of a tri-layer hydrogel as sections at Z1 and Z3 show both the GelMA and PAm hydrogels while Z2 only shows the GelMA hydrogel (Fig. 4.4B). The time-lapse recording of the perfused device (visualized by addition of

0.1% green fluorescent beads) shows the robustness of the PAm-GelMA interface, which do not dislodge from shear forces caused by flow rates up to 80 μL/hr. Furthermore, visualization of the flow field around various portions of the GelMA structure illustrates the convective mass transport reminiscent of blood flow *in vivo*.

4.4.2. Flow induces concentration gradient within GelMA structures

Fluid flow within the device containing cell-laden hydrogels can impart two effects—(i) compression of the GelMA structures due to increased fluid pressure and (ii) steady state concentration gradient of chemoattractants within the GelMA structures (due to their consumption by the entrapped cells) (167). Quantification of flow rate induced changes of the GelMA hydrogels exposed to various flow rates showed no differences in their area strain up to a flow rate of 40 μL/hr (Fig. 4.5). However, a significant change in the area strain was observed at 1000 μL/hr, which was used as a positive control (Fig. 4.5). Area strain instead of volumetric strain was used to assess the flow induced mechanical compression because the GelMA hydrogels were confined within the fluidics channel that does not allow any vertical displacements.

Next we assessed the presence of a chemotactic gradient within the GelMA hydrogel exposed to different flow rates (10, 20, and 40 μL/hr). To model the concentration gradient, we simulated the convective mass transfer of an arbitrary solute from the medium (C) capable of binding to its target enzyme/receptor through a Michaelis-Menten based consumption reaction (R_C) (Fig. 4.6A, **Eq. 1**).

$$\frac{\partial C}{\partial t} = D_C(\boldsymbol{\nabla} \cdot \boldsymbol{\nabla}\mathbf{C}) + R_C \qquad \textbf{(Eq. 1)}$$

Here, D_C is the diffusion coefficient of solute within the GelMA hydrogel. As indicated in Figure 4.6A, the domain, $\boldsymbol{\Omega}$, of the system is a 2-dimensional ellipse where the consumption of solute occurs via Michaelis-Menten kinetics (**Eq. 2**) while the perimeter, $\boldsymbol{\Gamma}$, of the GelMA hydrogel is governed by convective flux boundary condition (**Eq. 3**) where the Mass Transfer Coefficient (H) is approximated from the laminar flow over a plate (**Eq. 4**).

$$R_C = \frac{k_{cat}E_0C}{K_M + C} \qquad \textbf{(Eq. 2)}$$

$$\boldsymbol{n} \cdot \boldsymbol{J_C} = H(C(\boldsymbol{x}) - C_{Bulk}), \quad \text{for } \boldsymbol{x} \in \boldsymbol{\Gamma} \qquad \textbf{(Eq. 3)}$$

$$H = \frac{2D_C Sc^{1/3} Re^{1/2}}{3L} \qquad \textbf{(Eq. 4)}$$

$$Sc = \frac{\mu}{\rho D_C} \quad , \quad Re = \frac{\rho v l}{\mu} \qquad \textbf{(Eq. 5)}$$

In the above equations, k_{cat} is the catalytic coefficient, E_0 is the enzyme concentration, K_M is the Michaelis constant, L is the characteristic length, and C_{Bulk} is the concentration of solute in the bulk solution. Furthermore, we linearized the Michaelis-Menten reaction by assuming that the substrate concentration is much less than K_M since high cell density within the hydrogels would increase the consumption rate of solutes such that their concentration remains substantially low. With this assumption, Equation 2 can be simplified as follows:

$$R_C = (k_{cat}/K_M)\,E_0C \qquad \textbf{(Eq. 6)}$$

Based on this theoretical framework, we modeled the mass transfer of an arbitrary solute of molecular weight (MW) 75 kDa, more common for serum proteins, whose D_C within the GelMA hydrogel was approximated to be 10 μm^2/s (168). The concentration and the catalytic efficiency of the enzyme consuming this soluble factor was designated to be 100 nM and 10 mM^{-1}min^{-1}, respectively, based on common enzymes found within the cytosol(169, 170). In addition, the resulting concentration profile as a function of time is shown as 2-D heat maps and concentration profiles along the minor axis in Figures 4.6B and 2C, respectively. These plots suggest that the concentration of solute was substantially higher at the periphery than at the center of the GelMA structure at all time points. This is mainly due to the consumption of the solute by the encapsulated cells. Therefore, at steady state (at 10000s), a large concentration gradient was established within the GelMA structure indicating the presence of a chemotactic gradient (Fig. 4.6C).

To generalize this model to any proteins or biomolecules, we further examined how the concentration profile changes as a function of ϕ, which is defined as a ratio of D_C/A_E to $(k_{cat}/K_M)E_0$, where A_E is the perimeter of the ellipse multiplied by the height of the fluidics chamber. Here, ϕ is a non-dimensionalized parameter that compares the diffusion of a solute to its consumption rate. Our results indicate that increasing flow rates (X-Y) reduces the time required to reach steady state concentration profile at all ϕ

values (Fig. 4.6D and Fig. 4.7). The examination of steady state concentration profile indicates increase in concentration gradient throughout the entire ellipse structure with increase in flow rates (Fig. 4.6E and Fig. 4.8). On the other hand, the concentration gradient decreases in the ellipse structure with decreasing ϕ value. Our results indicate that the increase in flow rate exposes the cells within the GelMA hydrogels to greater concentration gradients even at an early time point after encapsulation.

4.4.3. Migration of HUVECs to the periphery of 3D GelMA structures

The above-discussed theoretical analysis predicts the existence of a chemotactic gradient that could drive the migration of HUVECs encapsulated within the GelMA hydrogels. The cell-laden structures were subjected to varying flow rates (10, 20, and 40 μL/hr) for three days post-encapsulation. Brightfield images at 3 days post-encapsulation show that the cell density at the interior of the GelMA structures decreases irrespective of the flow rates with large decrease in cell density with higher flow rates (Fig. 4.3A 1st and 2nd column). The quantitative analysis of cell density across the GelMA hydrogel as a function of culture time for different flow rates supports the above observation (Fig. 4.3B). We also observed differences in the spatial distribution of cells within the GelMA hydrogel under different flow rates. At 10 μL/hr, the cells within the GelMA structures were uniformly distributed at day 3 (Fig. 4.3A 2nd column). On the other hand, flow rates of 20 and 40 μL/hr resulted in the migration of most of the HUVECs to the periphery of the GelMA hydrogel structure (Fig. 4.3A 1st and 2nd column, 3B). The thickness of the HUVEC layer at the periphery of the GelMA hydrogel was found to be decreased for 40 compared to 20 μL/hr flow rate (Figure 4.3B 3rd column). For the remainder of the studies, we used cultures exposed to a flow rate of 40 μL/hr.

4.4.4. Co-Culture of HUVECs and cancer cell spheroids

We examined whether the migration of encapsulated HUVECs to the periphery of the GelMA hydrogel will persist in the presence of cancer spheroids. Brightfield images of the encapsulated cells at days 0, 3, and 5 reveal that the HUVECs indeed migrate to the periphery of the GelMA structures even in the presence of MCF7 spheroids (Fig. 4.2A).

We investigated the migration of HUVECs at smaller time increments by quantifying the changes in the local cell density as a function of time. To this end, we partitioned the ellipse structure into different zones, and quantified the cell density in each zone as a function of culture time. Immediately after encapsulation, the density of the encapsulated HUVECs across Z1 to Z5 was found to be uniform, suggesting a homogenous distribution of cells within the GelMA hydrogel structures (Fig. 4.2B). During days 1 to 3, a large number of HUVECs migrated to the periphery of the hydrogel with a decrease of 30-40% in cell density was observed within the GelMA hydrogel. This initial migration of HUVECs to the periphery substantially declined from day 4 and onwards (only 7-10% cell density decrease was observed from day 4 onwards) (Fig. 4.2C).

On the contrary, encapsulated MCF7 cell clusters remained intact and we did not observe migration of the spheroids or any individual cells migrating away from the spheroid. This observation was validated using labeled MCF7 cells (Fig. 4.9). The encapsulated cancer spheroids exhibited a gradual growth as a function of culture time (Fig. 4.2D). The spheroids were found to grow to approximately twice its size between days 0 and 5.

4.4.5. Characterization of the HUVEC layer at the periphery of the hydrogel structure

We next investigated whether the assembly of HUVECs around the GelMA structure forms an endothelial barrier. The cell-laden GelMA structures grown for 5 days were used to characterize the HUVEC structure. Confocal images of F-Actin and DAPI stained structures revealed the presence of HUVECs along the entire periphery (observed along the lateral and vertical directions) of the GelMA hydrogel (Fig. 4.10A). The HUVECs were also observed at both the GelMA-PAm interface (Fig. 4.10A). Interestingly, the HUVECs were found to be of single cell thickness as illustrated by the nuclei staining of the HUVECs around the ellipse (Fig 4.10A, DAPI column). In addition, the presence of continuous F-actin indicates that the HUVECs form a continuous monolayer sheet along the periphery (Fig 4.10A, Phalloidin column). Furthermore, to determine if cell-cell junctions are present within the monolayer sheet, the cell-laden GelMA structures were stained for VE-cadherin. Confocal images of the structures showed the presence of VE-cadherin that connects the neighboring HUVECs to form a single layer along the GelMA structure (Fig. 4.10B). In addition to presence of cell-cell junctions, we assessed the capacity of the endothelial sheet to serve as barrier to fluxes of molecules within the media by analyzing the diffusion of FITC-Dextran with MW of 10 and 150 kDa. The diffusion of Dextran into the cell-laden GelMa hydrogel was observed as the fluorescent signal within the ellipse increased with time (Fig. 4.11A). This process was quantified by plotting the mean normalized intensity within the central region of the ellipse (Fig. 4.11B). As expected, the 10 kDa Dextran achieved steady state after ~ 15 minutes while 150 kDa required ~ 30 minutes. At steady state, the larger MW dextran could not achieve nearly the same intensity as that of its smaller MW counter part suggesting the hindrance by the endothelial barrier towards allowing high MW molecules to diffuse into the hydrogel (Fig. 4.11C).

4.4.6. Dose dependent response of cells within the GelMA hydrogel to Doxorubicin

We assessed the potential of our device as a drug screening platform by analyzing the effects of Doxorubicin on HUVEC barrier and the tumor spheroids. Cell laden GelMA structures, cultured for 5 days, were exposed to different concentrations of Doxorubicin (1, 10, and 100 μg/mL) for 3 days. We investigated the penetration of Doxorubicin into the cancer spheroids by using fluorescent imaging. Our results indicate an increased accumulation of Doxorubicin in samples treated with 10 and 100 μg/mL of drugs (Fig. 4.12A). However, minimal accumulation of Doxorubicin was observed in samples treated with 1 μg/mL concentration (Fig. 4.12A). Brightfield images of cancer spheroids before and after 3 days of Doxorubicin exposure suggested a decrease in spheroid size and the darkening of the MCF7 spheroids exposed to 10 and 100 μg/mL Doxorubicin (Fig. 4.12B). To quantify the effects of Doxorubicin, we analyzed the changes in spheroid size before and after treatment with varying concentrations of the drug. MCF7 spheroids exposed to 10 and 100 μg/mL Doxorubicin experienced ~7 and ~15% decrease in spheroid area. On the other hand, the growth of the cancer spheroid was still observed at 1 μg/mL although the growth was ~ 20% less than those cultured in the absence of the drug (Fig. 4.12C). In addition to cancer spheroids, the drug was also found to be cytotoxic to HUVECs cells as the endothelial barrier was found to have disappeared upon exposure to Doxorubicin. This finding is consistent with other reports, which showed the cytotoxic effect of Doxorubicin on endothelial cells (171).

4.5. Discussion

This study describes the development of a tumor-on-a-chip platform comprised of cancer spheroid encapsulated within a GelMA hydrogel and surrounded by an endothelial barrier. Using a single step process, we simultaneously encapsulated HUVECs and MCF7 spheroids within our device. In addition, we harnessed the differential chemoattractant-induced motility of HUVECs and cancer spheroids to control their confinement and organization within the device.

Our results show the effect of flow rates on the generation of concentration gradient of soluble factors within the cell-laden GelMA structures. Our theoretical analysis does not specify a molecule or protein as a chemoattractant. Instead we used a range of ϕ values, the ratio of the diffusion to the consumption rate of a solute, to generalize the model to encompass the range of biomacromolecules present in the culture media. Specifically, we employed ϕ ranging from 1 to 1000 to account for (i) proteins or molecules with large differences MW which affects the diffusion coefficient and (ii) their specific receptors on the cell surface will vary in their catalytic efficiency (172).

Within the GelMA hydrogel containing both HUVECs and MCF7 spheroids, the cancer cells did not migrate in response to the gradient of soluble factors as they were confined to the center of the hydrogel. This lack of motility could be attributed to insufficient strength of the chemotactic gradient to cause the migration of cancer spheroids and/or cancer cells from the spheroids. In addition, the cell-cell contact mediated by the cadherin junctions within the cancer spheroid may also mitigate migration of cancer cells away from the spheres and within the GelMA hydrogel.

The Doxorubicin studies showed the potential of this tumor-on-a-chip platform to assess the response of cells to oncologic drugs. We have assessed the penetration of Doxorubicin into the tumor spheroid and its quantifiable cytotoxic effect on the cancer spheroid. Additionally, the loss of the endothelial barrier in devices exposed to high doses of Doxorubicin (> 10 μg/mL) suggests the lack of target specificity of this oncologic drug. This tumor-on-a-chip device can be translated to assess the efficacy of other cancer therapeutics in a physiologically relevant system that provides a co-culture system to test drug specificity, cancer spheroid in a 3-D environment, as well as an endothelial barrier that can potentially resist drug penetration especially for higher MW compounds (48).

Although the platform described here utilizes endothelial and cancer cell co-cultures, our approach provides a versatile framework for establishing systems with increased complexity observed in physiological tumors. *In vivo* tumor microenvironments are comprised of a variety of resident cells ranging from stromal cells to immune cells (173). The incorporation of supporting cells into the device can be accomplished by incorporating these cells into the GelMA structures along with HUVECs and cancer spheroid. The 3D pattern mediated confinement of cells within the device allows the compartmentalization of various cell populations to dissect the interaction and contribution of various cellular populations towards cancer growth individually and in concert. Such an in vitro platform recapitulating various attributes of in vivo tumor microenvironment could not only offers new insights but could also be used as a drug-screening platform. The presence of an encompassing endothelium closely mimics the vasculature present within actual tumors by allowing the circulating cells to attach, roll, and transmigrate. This could provide an additional perspective for analyzing the extravasation of circulating cells into the tumor site, which can be achieved by introducing suspended single cells into the injected media or intravasation of cancer cells into the circulating system.

4.6. Acknowledgements

The authors acknowledge that this study was supported by the National Institute of Arthritis and Musculoskeletal and Skin Diseases of the National Institutes of Health under Award Number R01 AR063184-02. The authors also acknowledge the University of California San Diego Neuroscience Microscopy Shared Facility funded through NS047101. AA acknowledges the support from ARCS foundation and the Ruth L. Kirschstein National Research Service Award NIH/NHLBI T32 HL 105373.

Chapter 4, in full, is a reprint of the material as it appears in Lab on a Chip, vol. 16, 2016. “Chemotaxis-driven assembly of endothelial barrier in a tumor-on-a-chip platform”. Aung, Aereas; Theprungsirikul, Jomkuan; Lim, Han L; Varghese, Shyni. The dissertation author was the primary investigator and author of this paper.

4.7. Figure

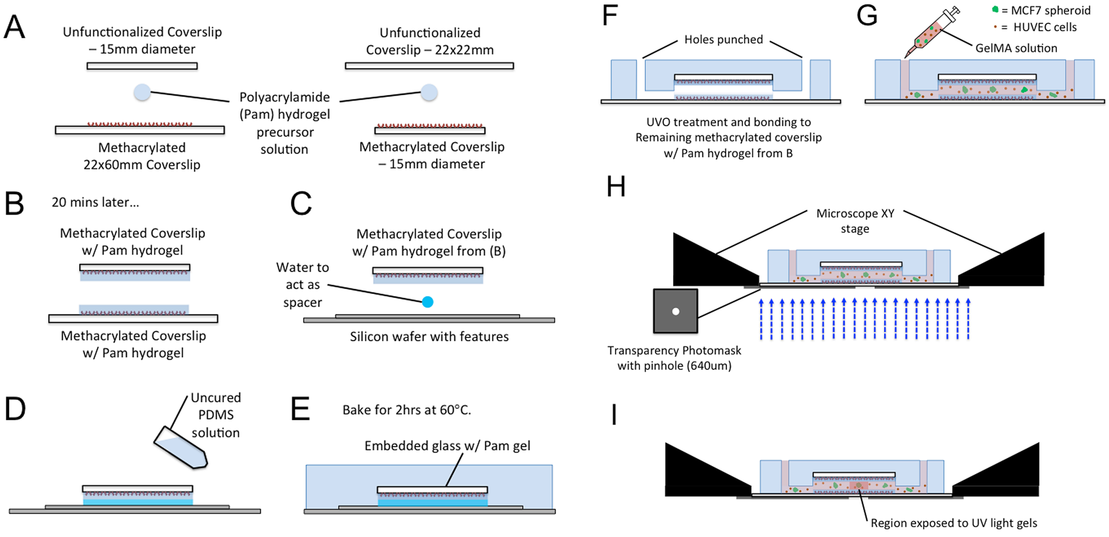

Figure 4.1: Schematic of fabrication of tumor-on-a-chip devices.

(A-B) Synthesis of thin PAm hydrogels tethered to the methacrylated coverslips is done by sandwiching 3 µL of polymer precursor solution between a methacrylated coverslip and a non-treated coverslip. (C-E) 5 µL of deionized water is sandwiched between the Si wafer mold and PAm hydrogel tethered to the methacrylated coverslip to act as a spacer as the uncured PDMS solution is poured on top of the wafer slowly and casted in the oven for 2 hours at 60°C. (F) Holes were punched on the cured PDMS after detachment from the Si wafer prior UVO treatment and bonding. (G) MCF7 spheroids and HUVECs were suspended gently in GelMA solution, drawn into a syringe before injecting into the microfluidic chip. (H-I) The chip is then mounted onto the movable microscope stage mount, on a transparency photomask. This allows us to see the MCF7 spheroids through the photomask on the microscope. After centering a spheroid in the middle of the transparency hole, collimated UV light is reflected via the DAPI filter cube through the transparency, gelling only the selected region of within the microfluidic chamber.

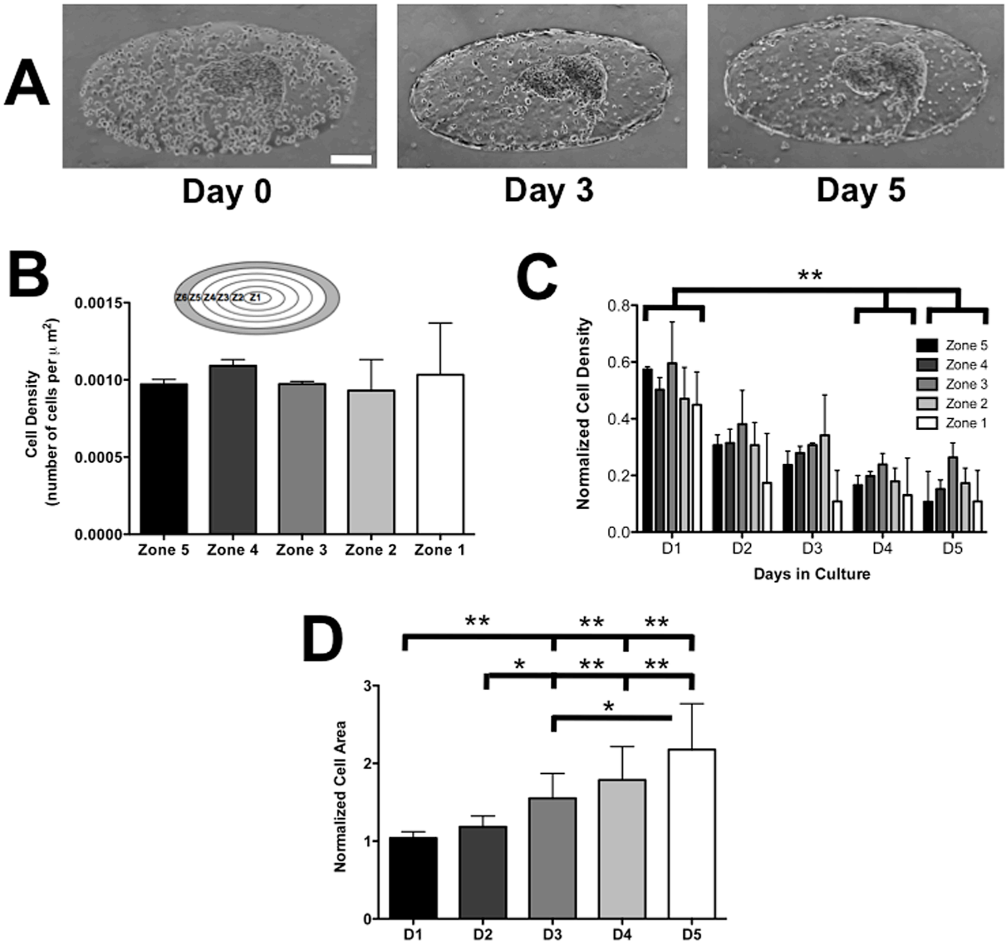

Figure 4.2: Co-culture of HUVECs and MCF7 spheroids within GelMA structures.

(A) Brightfield images of HUVECs co-cultured with MCF7 spheroids at immediately after encapsulation (D0), Day 3 (D3), and Day 5 (D5). Scale bar: 200 μm. (B) Cell density within Zones 1 through 5 on D0 within the GelMA hydrogel. Different zones are indicated within the inset. The shaded peripheral region in the diagram, Zone 6, is excluded from the quantification. (C) Changes in the normalized zonal density of HUVECs with culture time. Within each zone, the cell density monitored as a function of culture time was normalized to D0 density and was plotted in the bar graph. (D) Spheroid size, quantified by 2-D area and normalized to D0 size, as a function of culture time. * and ** indicate statistically significant differences of $p < 0.05$ and 0.01, respectively, as obtained from pair wise t-test. In (C), differences were reported only if the changes in normalized cell density were statistically significant in all zones (Zone 1-5) between different culture days.

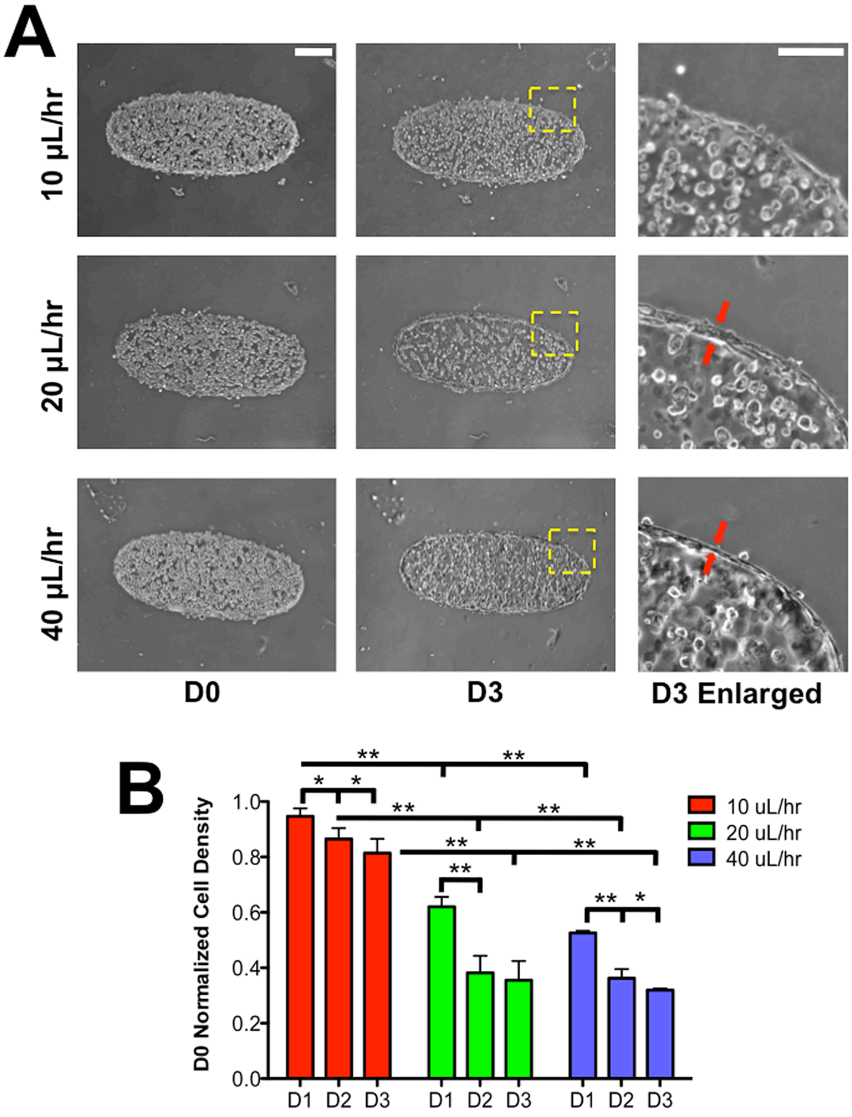

Figure 4.3: Flow-induced migration of encapsulated HUVECs.

(A) Brightfield images of HUVECs within GelMA hydrogels as a function of culture time. Each row represents different flow rates while the 1st and 2nd column represent different culture days —day 0 (D0) indicates the day of encapsulation. Scale bar: 200 µm. The 3rd column represents a magnified image of the region identified by a square window with yellow dashed lines in each row of day 3 (D3) images. The red arrows indicate the HUVECs at the periphery of GelMA structure. Scale bar: 30 µm. (B) The change in local density of HUVECs at different culture times for flow rates of 10, 20, and 40 µL/hr. The y-axis represents the local cell density quantified at specified culture day normalized to D0 cell density. * and ** indicate statistically significant differences of $p < 0.05$ and 0.01, respectively, as obtained from pair wise t-test.

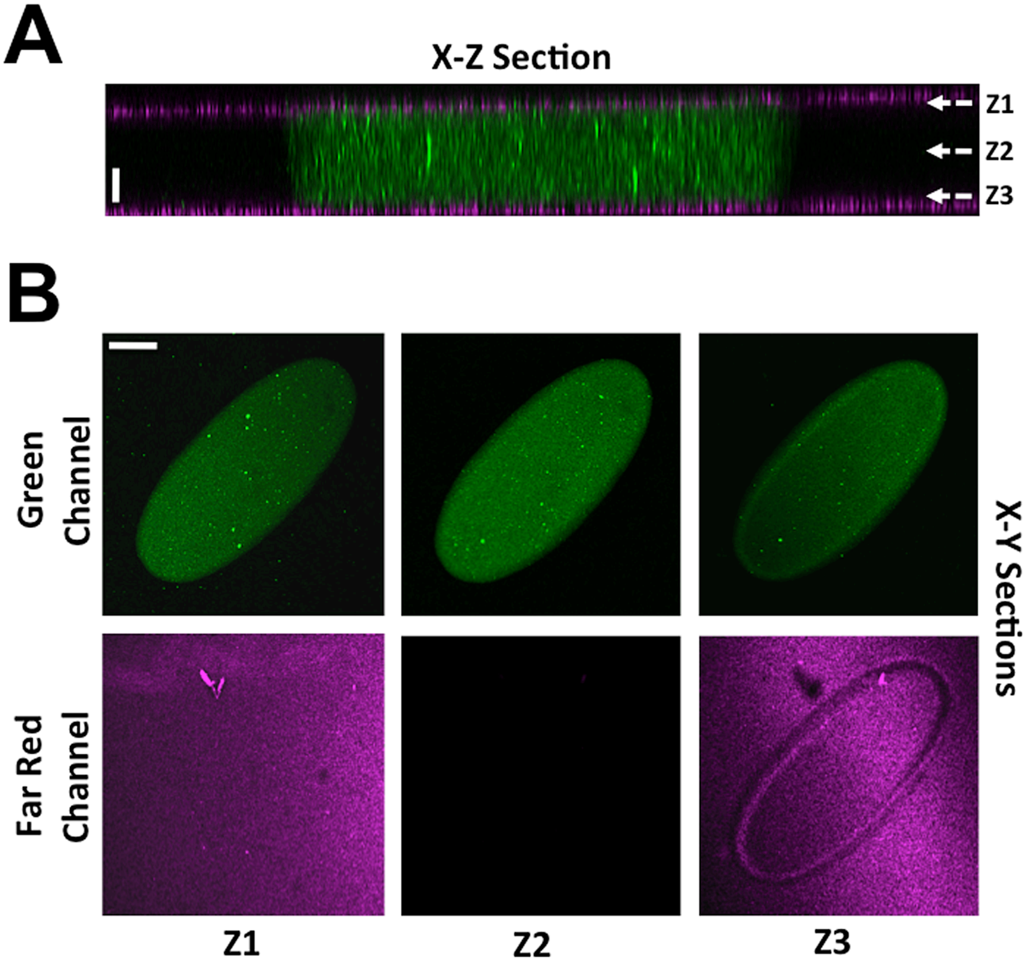

Figure 4.4: Characterization of the device.

(A) X-Z confocal sections of a photo-patterned GelMA hydrogel sandwiched between two PAm hydrogels. Far red and green fluorescent beads are used to visualize the PAm and GelMA hydrogels, respectively. Scale bar: 50 µm. (B) X-Y confocal sections of the green and far-red channels at Z positions—Z1, Z2, and Z3—listed in (A). Scale bar: 200 µm.

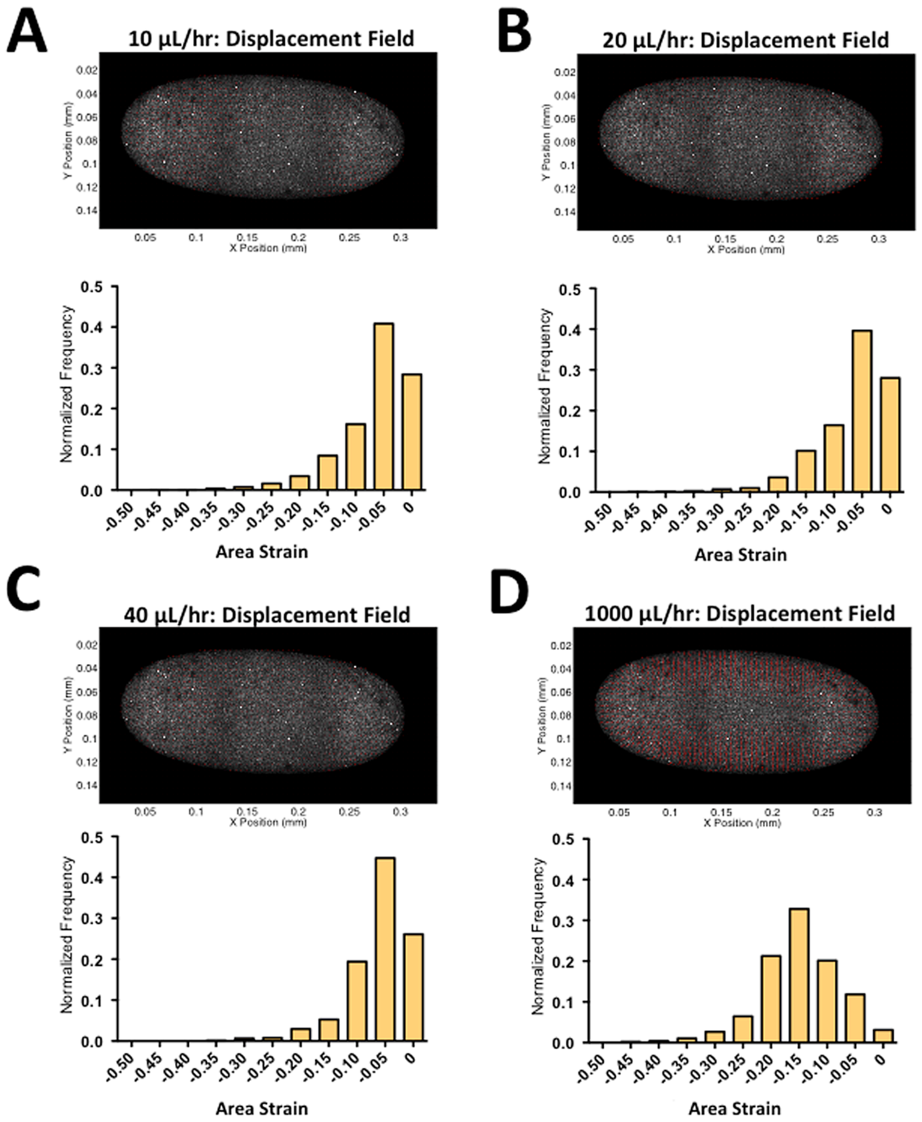

Figure 4.5: Flow induced compression of GelMA hydrogels.

(A-D) The deformation of the GelMA hydrogel at different flow rates of 10, 20, 40, and 1000 μL/hr. The deformation of the hydrogel is depicted by (i) 2D displacement vectors overlaid onto the fluorescent images and (ii) distribution of area strain, shown as a histogram, to assess the extent of mechanical compression.

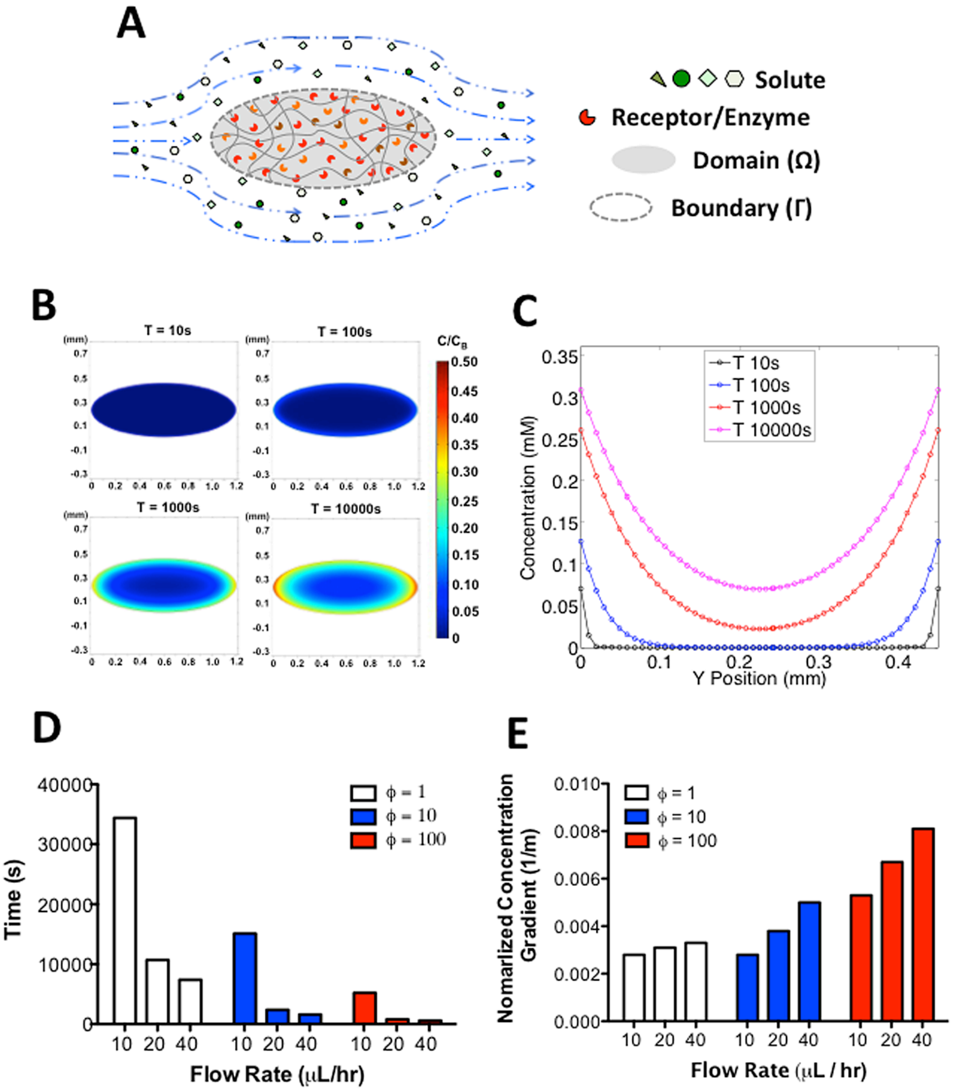

Figure 4.6: Concentration gradient within GelMA hydrogels.

(A) Illustration of the diffusion-reaction mass transfer system with convective boundary condition. The interior of the ellipse contains encapsulated cells that consume the soluble factors supplied across the boundary of the ellipse via convection. (B) Heat map of the changes in the normalized concentration (concentration within the GelMA normalized to the bulk concentration in the media) with time. (C) Changes in the normalized concentration profile with time along the minor axis of the ellipse. Time required to reach steady state (D) and maximum normalized concentration gradient at steady state (E) for different flow rates at $\phi = 1, 10, 100$.

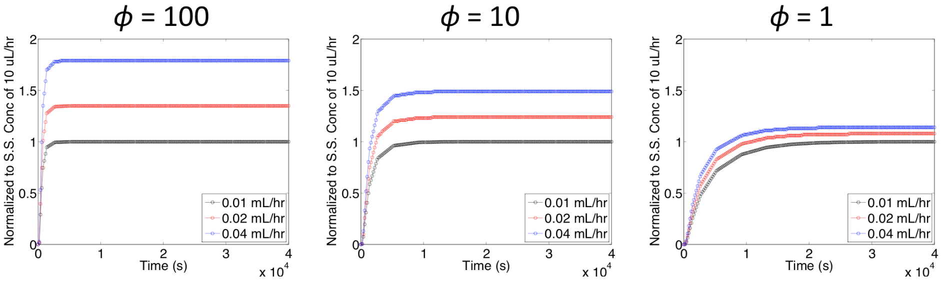

Figure 4.7: Transient concentration changes within the GelMA hydrogel.

The normalized concentration, defined as the ratio of the concentration within the hydrogel to the bulk concentration, at the center of the ellipse as function of time for different flow rates and ϕ values. Here, ϕ is a non-dimensionalized parameter that compares the diffusion to the consumption of a solute.

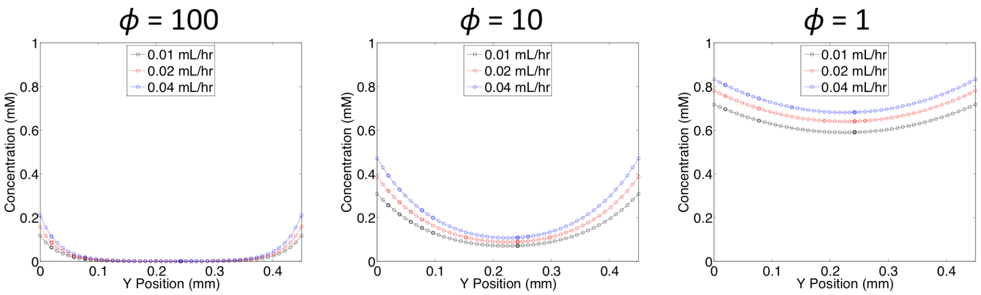

Figure 4.8: Steady state profile within the GelMA hydrogel.

The normalized concentration (the ratio of the concentration within the hydrogel to the bulk concentration) profile along the minor axis of the ellipse structure for different flow rates and ϕ values.

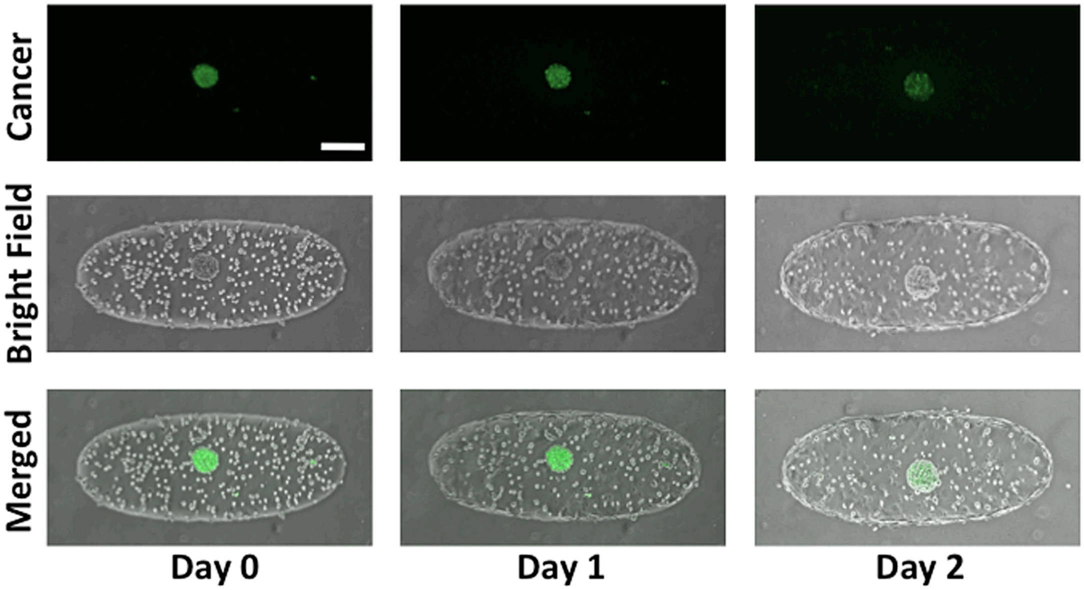

Figure 4.9: Cancer spheroids remain clustered within the GelMA hydrogel with culture time.

Brightfield and fluorescent images of HUVECs and cancer spheroid (labeled with green dye) within GelMA structures at immediately after encapsulation and after 1, 2, and 3 days in culture. Scale bar: 200 µm.

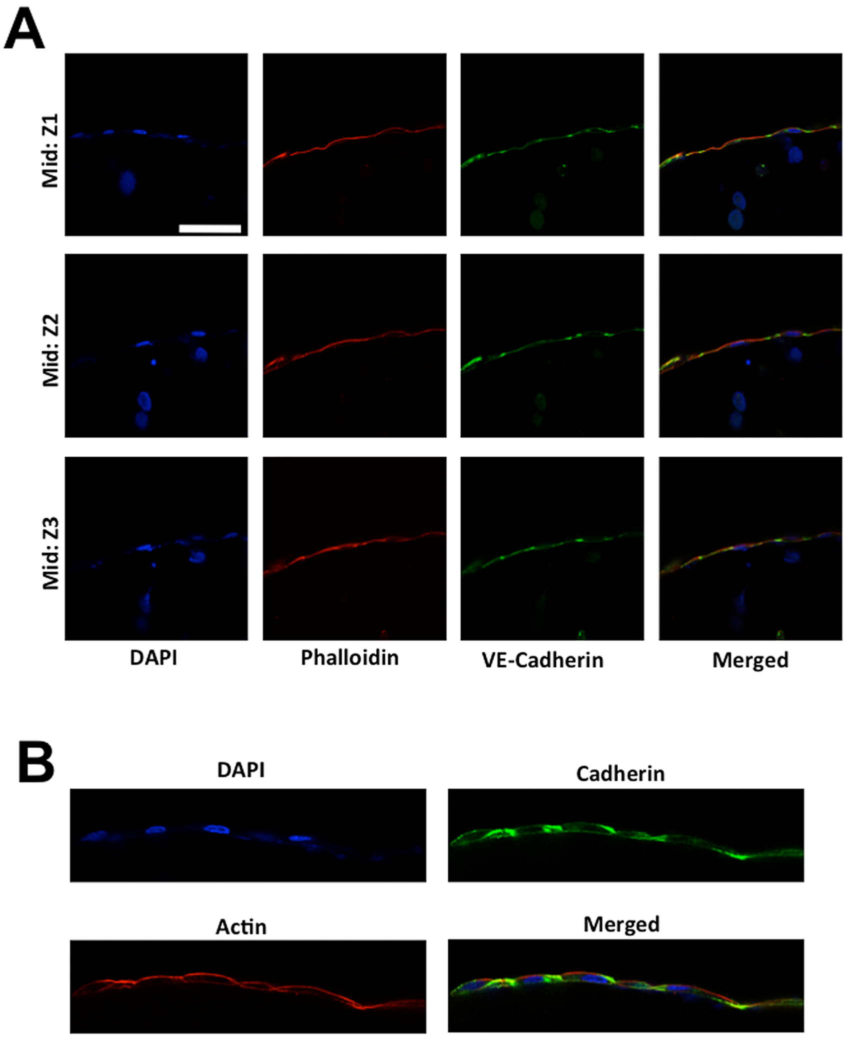

Figure 4.10: Immunostaining of HUVECs cells migrated to the periphery of the GelMA structure.

(A) X-Y confocal sections of HUVECs cells stained for F-Actin (red) and nuclei (blue) at different Z positions: GelMA-PAm interface (labeled as Top and Bottom) and middle of the GelMA hydrogel (labeled as Mid). Green fluorescent beads were embedded within the PAm hydrogels to visualize the presence of the hydrogels. The rows indicate the specified Z positions. The columns 1-3 indicate the specific color channel while column 4 displays the merged image from other channels. Scale bar: 100 µm. (B) High magnification X-Y sections of HUVECs stained for VE-Cadherin (green), F-Actin (red), and nuclei (blue) at the midsection of the GelMA hydrogel. Scale bar: 10 µm. The HUVECs in both images were cultured with MCF7 spheroids for 5 days within the fluidics device prior to staining.

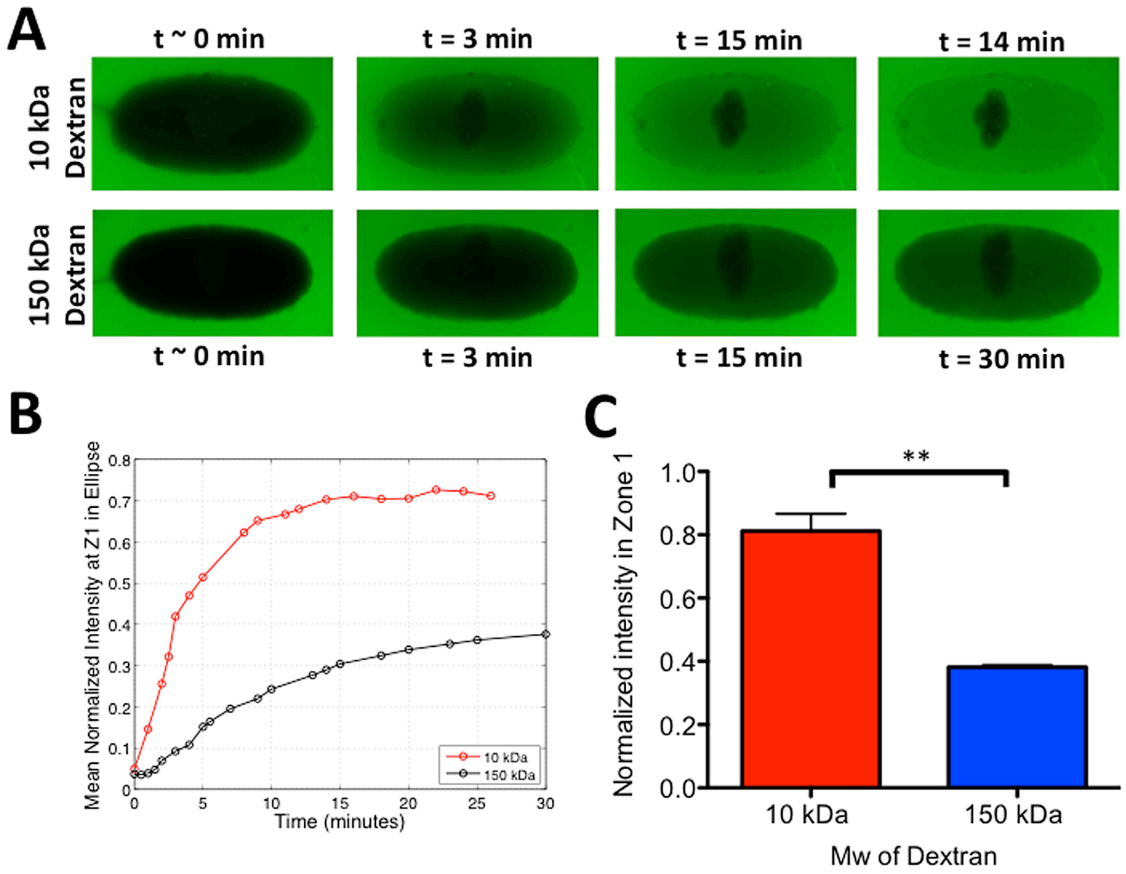

Figure 4.11: Diffusion of FITC-Dextran into cell-laden GelMA hydrogels.

(A) Fluorescent images of 10 µg/mL 10 kDa and 100 µg/mL 150 kDa FITC-Dextran (top and bottom row, respectively) diffusing into the ellipse-shaped GelMA hydrogels at the specified time points. The mean normalized intensity with zone 1 or Z1 ellipse for 10 and 150 kDa Dextran as a function of time (B) and at steady state (C). Zone 1 or Z1 ellipse is the small ellipse shown in Figure 3B. ** indicates a statistically significant difference of $p < 0.01$ as obtained from t-test.

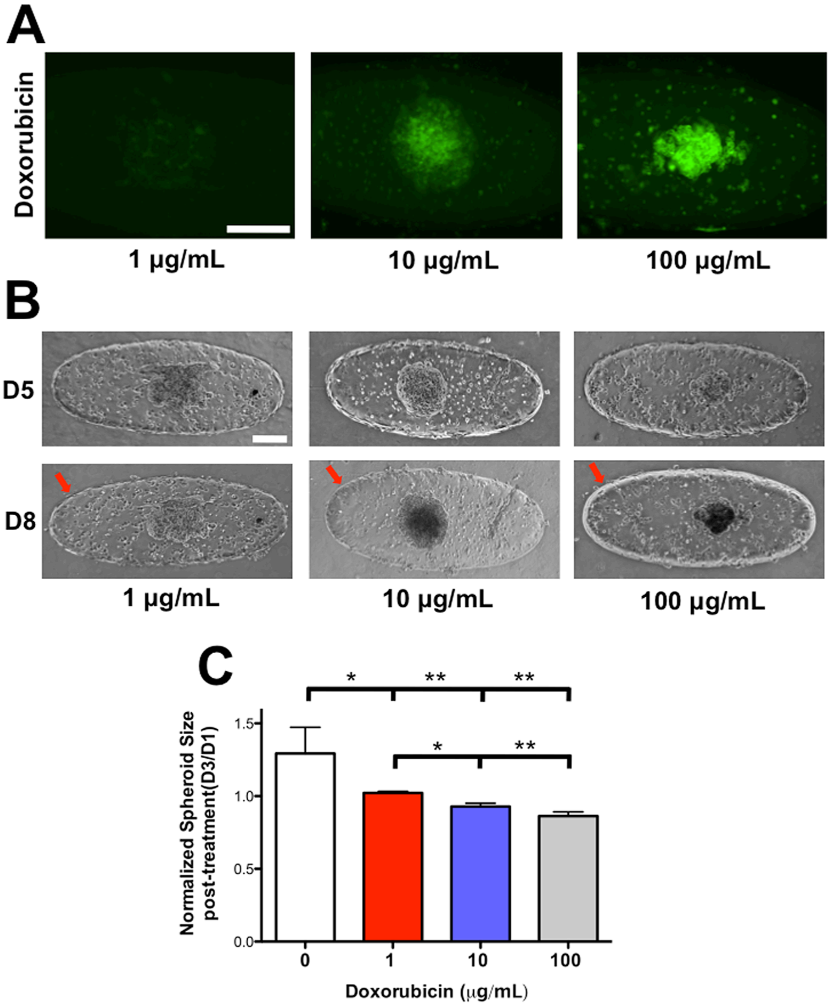

Figure 4.12: Dose-dependent response of encapsulated tumor spheroids to Doxorubicin.

(A) Fluorescent images to identify Doxorubicin penetration into the cancer spheroids at D8. Increased penetration of Doxorubicin into the MCF7 spheroid is observed at higher dosages. Scale bar: 200 µm. (B) Brightfield images of HUVECs and MCF7 spheroids prior to (D5) and 3days after Doxorubicin treatment (D8). Red arrow points towards the presence of endothelial barrier and the lack thereof at and above 10 µg/mL of Doxorubicin, respectively. Scale Bar: 200 µm. (C) Change in spheroid size of MCF7 after Doxorubicin treatment for different dosages of Doxorubicin. The spheroid area, obtained from 2-D brightfield images, at D8 is normalized to the area at D5. * and ** indicate statistically significant differences of $p < 0.05$ and 0.01, respectively, as obtained from pair wise t-test.

Chapter 5: Engineered tumor-on-a-chip device with cancer immune interactions for assessing T-cell recruitment

5.1. Abstract

Cancer is touted to be the 2nd leading cause of death in the United States only to be superseded by heart disease. Despite the outbreak of this epidemic, the increased understanding of the disease has lead to the development of novel and effective treatments such as immunotherapy that mobilizes patients' immune cells to eliminate cancer. Specifically, these therapies rely on the presence of cytotoxic T-cells within the tumor to achieve an efficacious outcome. The current understanding of cytotoxic T-cell trafficking into the tumor microenvironment utilizes animal models to identify specific immune cells and their interactions that result in the secretion of chemokines. The complexity of these *in vivo* systems hinders further investigation into cancer-immune interactions that may abrogate or promote T-cell recruitment. To this end, we have utilized a 3D photopatterning and microfluidics technology to create bilayer cylindrical hydrogels with the interior compartments containing cancer cells and monocytes and exterior compartment containing endothelial cells encompassing the periphery of the entire structure. Furthermore, we have created two distinct morphologies of the cancer cells, dispersed single cells and a spheroid, to determine the effect of not only the co-culture system but of cancer cell morphology on the extravasation of T-cells from the surrounding media. Our results indicate that cancer spheroids recruit T-cells into the GelMA hydrogels in contrast to dispersed cancer cells. Furthermore, the presence of monocytes along with dispersed cancer cell or cancer spheroid increased the recruitment

capacity. Interestingly, monocytes alone were observed to not recruit T-cells into the cell-laden hydrogel. These results highlights the capacity of this platform to create co-cultures that controllably recapitulate cancer-immune interactions and assess how such cross talk can recruit T-cells.

5.2. Introduction

Within the United States alone, approximately 0.6 million individuals are estimated to die from cancer in 2016 (1). The lives claimed by this disease is second only to heart diseases as the number of new caner patients continue to steadily increase with each successive year (1). However, tremendous progress has been made to curb this epidemic due to the novel treatments that capitalize on the increased understanding of cancer biology and cancer-stromal interactions. As such, the use of immunotherapies that deploy patients' own immune cells to eliminate cancer cells has shown tremendous potential as a cure for cancer (77, 174, 175).

Current approaches focus on using cytotoxic T-cells that are touted as the primary immune cells capable of efficiently eliminating cancer cells. These treatments range from using engineered T-cells such Chimeric Antigen Receptor (CAR) T-cells for targeted therapy to immune checkpoint inhibitors to overcome cytotoxic T-cell suppression by cancer cells (174-177). Moreover, the efficacious result from using T-cells is highlighted by having 19 out of 27 patients with acute lymphoblastic leukemia (ALL) remain in remission after CAR T-cell therapy (174). Despite the potential use of T-cells for liquid cancers, the use of T-cells for eliminating solid tumors has yet come to fruition due to the lack of understanding of key mechanisms that underlies cytotoxic T-cell recruitment into the tumor stroma (178-180).

The infiltration of cytotoxic T-cells into solid tumors is dependent on cancer-stromal interactions that modulate the local immune microenvironment (68, 181). These interactions can result in selective recruitment of inflammatory cells such as classically activated macrophages that secrete potent chemokines such as CXCL9 and CXCL10 which in turn recruit activated immune cells such as cytotoxic T-cells (182-184). Conversely, the shift in interactions between cancer and immune cells may skew the recruitment towards alternatively activated macrophages, which attract regulatory T-cells via CCL5 and CCL20 to suppress the inflammatory responses (68, 185-187). These interactions are only a minute display of the cross talks occurring between cancer and stromal cells while a plethora of other unknown interactions that modulate cytotoxic T-cell recruitment has yet to be identified. The shear complexity of the cancer microenvironment involving numerous cell types each affected by physicochemical cues renders the elucidation of novel interactions to be a daunting task.

In addition to the role of stromal cells in shaping the cancer microenvironment, the morphology of the cancer cells modulates their behavior. Studies have indicated the crucial differences between cancer cells on 2D surfaces and within 3D environment where their migration and proliferation are altered (81, 188). Cancer cells in particular further exhibit drastic changes by residing within a 3D microenvironment or within a 3D cellular aggregate (189-191). The compact nature of cells within an aggregate results in the depravation of nutrients in the interior thereby causing gradients in oxygen, glucose, lactate, and ATP to form within the cell mass (41, 192-194). More importantly, these gradients lead to hypoxic conditions within the spheroid reflecting the tumor microenvironment observed *in vivo*.

To accurately investigate the role of cancer-immune interactions on T-cell recruitment, the morphology of the cancer cells and the presence of immune cells must be recapitulated. We have adapted our microfluidics-based 3D photopatterning approach to recreate the cancer stroma containing immune cells (162, 163, 195). Specifically, we used an additive approach to photopattern a bilayer cylindrical GelMA hydrogel where the interior scaffold contains cancer cells (MCF7) and monocytes (THP-1) while the exterior contains endothelial cells (HuVECs). The endothelial cells were found to create a layer encasing the periphery of the GelMA hydrogel. With this approach, hydrogels were created containing cancer spheroids or dispersed cancer cells, monocytes, and endothelial cells. Furthermore, we have used these cell-laden constructs to analyze the extravasation of T-cells (TALL-104) from the surrounding media into the GelMA hydrogels. Our results indicate that the cancer spheroid better recruits T-cells compared to dispersed cancer cells. In addition, monocytes together with cancer cells synergistically recruit T-cells into the GelMA hydrogel.

5.3. Materials and Methods

5.3.1. Cell Culture

Human vascular endothelial cells (HuVECs), MCF7 cells, THP-1 cells, and TALL-104 cells were obtained from ATCC and cultured according to their protocol. HuVECs were cultured in HuVEC media (HM) comprised of 78% Medium 199 media (Gibco), 10% fetal bovine serum (FBS) (Gibco), 10% endothelial cell growth media (Cell Application, Inc.), 1% sodium pyruvate (Gibco), and 1% Penicillin/Streptomycin (P/S). The HuVECs used in this study did not exceed passage 6. MCF7 cells were cultured in growth medium (GM) containing 89% Dulbecco Modified Eagle's high glucose media, 10% FBS, and 1% P/S. THP-1 cells were cultured in monocyte media (MoM) supplemented with ~ 79% RPMI-1640 media (Gibco), 10% FBS, 1% P/S, and 5 μM 2-

Mercaptoethanol. TALL-104 cells were cultured in T-cell media (TM) comprised of 20% FBS and 80% Iscove's Modified Dulbecco's Medium (ATCC). This mixture was further supplemented with 75 units/mL recombinant human IL-2 (Peprotech), 2.5 µg/mL human albumin (Sigma-Aldrich), 0.5 µg/mL D-Mannitrol (Sigma-Aldrich). Cell laden hydrogels were cultured in mixed media (MM) comprised of 50% HM and 50% MoM.

5.3.2. MCF7 spheroid formation

MCF7 cells were trypsinized from tissue culture dish and 1 million cells were resuspended in 4.5 mL of GM. This mixture was added to a 60 mm diameter petri dish and cultured on an orbital shaker (VWR, Model No. DS-500E) rotating at 45 rpm in a cell culture incubator kept at 37 °C and 5% CO_2. The spheroids were used after being cultured for 2 days.

5.3.3. Fluorescent labeling of cells

THP-1 or TALL-104 cells grown in their respective culture media were collected into 15 mL conical centrifuge tubes and pelleted by centrifugation at ~ 800 RCF for 4 minutes. The culture media was aspirated and the pellet was resuspended in 1 mL of Opti-MEM (Gibco) containing 5 µM Green Cell Tracker or Red Cell Tracker. This mixture was incubated at 37°C and 5% CO_2 for 15 minutes. The cell labeling process was stopped by adding 9 mL of PBS followed by centrifugation and aspiration of PBS containing excess fluorescent dye. The pellet was resuspended and maintained in 1 mL of culture media.

5.3.4. Preparation of GelMA hydrogel precursor solution

Different amounts of GelMA were dissolved in PBS to create a 7, 8.5, or 10% wt/v solution and incubated in a 60°C water bath for 20 minutes. The solution was immediately syringe filtered with a pore size of 0.22 μm to avoid possible contamination during cell culture. The filtered solution was kept at 37 °C until use.

5.3.5. Fabrication of tumor-on-a-chip device for additive photopatterning

We have previously described the fabrication process for tumor-on-chip device (195). In brief, the process can be generalized into the following steps: methacrylation of glass surfaces, fabrication of microfluidics device containing polyacrylamide (PAm) hydrogels, and photopatterning of cell-laden GelMA hydrogels within the fluidics device.

Methacrylation of glass surfaces

25 x 50 mm rectangular and 15 mm diameter glass coverslips were cleaned using 1.5 M NaOH for 30 minutes and rinsed in DI water. The coverslips were air dried and incubated with 2% (v/v) 3-(Trimethoxysilyl)propyl methacrylate solution diluted in 0.55% glacial acetic acid and 99.5% ethanol for 5 minutes. After the reaction was completed, the glass surfaces were thoroughly rinsed with pure ethanol and dried in an oven at 60 °C for 30 minutes. The coverslips were used immediately.

Fabrication of microfluidics device containing PAm hydrogels

PAm hydrogels were formed on methacrylated glass surfaces by sandwiching 1.75 μL of hydrogel precursor solution containing 5% wt/v acrylamide, 0.2% wt/v bis-acrylamide, 0.1% wt/v ammonium persulfate, and 0.01% wt/v *N*,*N*,*N′*,*N′*-Tetramethylethylenediamine between a methacrylated and a non-methacrylated coverslip. Specifically, the precursor solution was added to the center of a methacrylated rectangular coverslip and a non-methacrylated 15 mm diameter coverslip was placed on top of the droplet to form a hydrogel layer at the bottom of the fluidics device. This procedure was repeated for a methacrylated circular coverslip and a non-methacrylated square coverslip to form the top layer of the device. After 30 minutes of polymerization, the hydrogels were incubated in DI water for 20 minutes before carefully removing the non-methacrylated coverslips. The resulting hydrogels were equilibrated overnight in DI water prior to use.

5 μL of DI water was added to the center of the mold for the flow chamber patterned on a silicon wafer. PAm hydrogel attached to a 15 mm diameter coverslip was placed onto the drop and PDMS solution, made from a degassed mixture of Sylgard 184 base and catalyst at weight ratio of 10:1, was carefully poured onto the silicon wafer until the entire surface was covered. The silicon wafer containing the PAm hydrogel was baked in the oven at 60 °C for 2 hours before removing the polymerized PDMS mold along with the attached hydrogel. The hydrogel tethered to the PDMS mold was re-equilibrated in a large droplet of DI water for 2 hours.

The rectangular coverslip and PDMS mold containing PAm hydrogels were placed in an UV-Ozone chamber under oxygen flow for 5 minutes. Care was taken to prevent the direct exposure of the PAm hydrogels to deep UV light. After the UV-Ozone treatment, the rectangular coverslip and PDMS mold were bonded together by bringing them into contact while maintaining the alignment between the PAm hydrogels attached to their surfaces. The microfluidics device was placed in a 60 °C oven overnight to complete the bonding process. To culture cells within the microfluidics device, the PAm hydrogels were equilibrated in PBS and the flow chamber was UV-sterilized for 45 minutes.

Photopatterning of cell-laden GelMA hydrogels within the fluidics device

For the additive photoencapsulation process, 1 mL of MoM containing 5 million fluorescently labeled THP-1 cells were mixed with 1 mL of GM containing MCF7 spheroids. 6 mL of PBS was added to the mixture before recovering the cells via centrifugation and removal of the supernatant. The cell pellet was resuspended in GelMA precursor solution containing 0.01% wt/v ascorbic acid and 2.0 μM LAP before adding the solution into a microfluidics device containing PAm hydrogels. The cell-laden device was placed on a microscope stage mounted with a transparency film containing a 350 μm diameter circle pattern and single MCF7 spheroids surrounded by fluorescently labeled THP-1 cells were located. This region was exposed to UV light (365 nm ± 15 nm wavelength) for 20 seconds to form cylindrical GelMA hydrogels laden with cells. The unpolymerized solution was removed by adding PBS containing 5% P/S. The resultant hydrogels were maintained in PBS with 5% P/S for 5 minutes before adding a GelMA precursor solution containing 2 million HuVECs, 0.01% wt/v ascorbic acid, and 2.0 μM LAP. The fluidics device was placed on a transparency film containing 1000 μm diameter circle and mounted onto a microscope. The cancer and monocyte laden cylindrical hydrogels were located and positioned to be at the center of the circular pattern prior to exposing the region to UV light for 20 seconds to form the annular GelMA structure laden with HuVECs. Unpolymerized solution was removed by the addition of PBS with 5% P/S and the encapsulated cells within the microfluidics device was maintained in MM and cultured in a humidified incubator kept at 37°C and 5% CO_2.

To photopattern bilayered GelMA hydrogels with dispersed cancer cells and monocytes in the interior cylinder, 6 million cancer cells were used in the encapsulation process instead of cancer spheroids. After injection of cancer cells and monocytes suspended in GelMA precursor solution, arbitrary areas were chosen to photopolymerize 350 μm diameter cylindrical hydrogels laden with dispersed cancer cells and monocytes.

For the single step encapsulation process, 2 million HuVECs, 5 million THP-1 cells, and 1 mL of GM containing MCF7 spheroids were diluted in PBS and pelleted via centrifugation. The supernatant was removed and the cells were resuspended in GelMA precursor solution containing 0.01% wt/v ascorbic acid, and 2.0 μM LAP. This mixture was added to the microfluidics device and photopolymerized using a transparency film containing a 1000 μm diameter circle pattern.

5.3.6. TALL-104 cell infiltration assay

GelMA hydrogel composite structures (cylinder and annulus) laden with cells were cultured within the microfluidics device for 4 days. 6 million TALL-104 cells were suspended in 100 μL of MM, added into the fluidics device, and incubated at 37 °C and 5% CO_2 for 40 minutes. Excess T-cells unattached to the GelMA hydrogels were removed by rinsing in PBS and the cell-laden hydrogels with T-cells adhered to the endothelial cells were cultured for 2 days in MM.

5.3.7. Analysis of TALL-104 cell distribution within GelMA hydrogel

Fluorescent images of GelMA hydrogels infiltrated with fluorescently labeled TALL-104 cells at $\text{Day}^{T}0$ through $\text{Day}^{T}2$ were analyzed and processed using a custom written code in Matlab. In brief, the circular cross section of the hydrogel was partitioned into 9 annular regions as indicated in the inset of Figure 4C. The number of cells within each region were counted and normalized by the total number of cells within the hydrogel. The cell fraction within each zone was plotted against the position of the midpoint in each annular region normalized to the radius of the entire GelMA hydrogel.

To obtain the value for the Distribution of T-cells (DoT), the centroid of each cell was obtained and the following formula was used: $\sum_{i=1}^{n} m_i \mathrm{r}_i^2$, where i is an individual T-cell, n is the total number of T-cells throughout the construct at $\text{Day}^{T}2$, m_i is $1/n$, and r_i is the distance between the center of the bilayer GelMA hydrogel to the centroid of a particular T-cell.

5.4. Results

5.4.1. Characterization of 3D photopatterned GelMA hydrogels within a fluidics device

GelMA precursor solution containing green fluorescent particles of 200 nm diameters is photopatterned into a cylindrical structure within a microfluidics device.

The X-Z confocal section shows the GelMA hydrogel sandwiched between two PAm hydrogels, embedded with far-red fluorescent particles of 200 nm diameters, on the top and bottom of the flow chamber (Fig. 5.1A). The X-Y confocal sections at the vertical positions Z1 and Z3 depict the interfaces between the GelMA and PAm hydrogels while the Z2 position illustrates the circular cross section of the GelMA hydrogel at the middle of the fluidics chamber (Fig. 5.1A).

5.4.2. Monocytes intravasate into the perfused media from the GelMA hydrogel containing a multi-cellular co-culture

GelMA hydrogels laden with a cancer spheroid, monocytes, and endothelial cells were monitored as a function of culture time. Brightfield images show the formation of an endothelial layer at the periphery of the hydrogel in the absence and presence of cancer cells (Fig. 5.1B). In addition, the fluorescence images show a decrease in the number of encapsulated monocytes with culture time. The quantification of monocyte density indicates a ~30% decrease after two days in culture with and without a cancer spheroid (Fig. 5.1C). Furthermore, the local cell density after two days of culture shows a low monocyte density in zone 1 (center of the cylinder) compared to zones 2-4 (towards the periphery) suggesting a sustained departure of these cells from the GelMA hydrogel into the perfusing media (Fig. 5.1D).

5.4.3. Additive 3D photopatterning for spatial organization and compartmentalization of multi-cellular co-cultures

To position and compartmentalize different cell types within the same microfluidics device, GelMA precursor solutions containing different cells were polymerized sequentially. Specifically, a 350 μm diameter cylindrical hydrogel encased within a larger cylinder with an outer diameter of 1000 μm was created. The X-Z confocal section of the acellular hydrogels show an inner core embedded with red particles surrounded by an exterior hydrogel layer of ~ 325 μm thickness (Fig. 5.2A). The X-Y confocal sections at different z positions show the PAm-GelMA interface along with the two distinct hydrogel structures: an inner cylindrical core (visualized by red particles) and an exterior cylindrical hydrogel (visualized by green particles) (Fig. 5.2A).

5.4.4. Formation of a cancer spheroid-immune cell co-culture encased within an endothelial barrier using the additive photopatterning approach

Using the additive photopatterning approach, a cancer spheroid and monocytes were encapsulated within a cylindrical GelMA hydrogel (7% wt/v) prior to polymerizing the outer hydrogel from 10% wt/v GelMA precursor solution containing endothelial cells. The brightfield image of the encapsulated cells at Day 0 depicts the presence of a cancer spheroid surrounded by monocytes labeled with a green fluorescent dye (Fig. 5.2A Top Left panel). After two days of culture, the endothelial cells were observed to migrate to the periphery of the hydrogel composite structure to form an endothelial layer (Fig. 5.2A Top Right panel).

We next characterize the effect of exterior GelMA hydrogel concentration on the encapsulated cells. Brightfield images of endothelial cells encapsulated in 10% or 7% GelMA hydrogels show the formation of an endothelial layer at the periphery after two days of culture irrespective of GelMA concentration (Fig. 5.2A). Additionally, GelMA hydrogels at all concentrations retain a substantial number of fluorescently labeled monocytes with culture time unlike the single step encapsulation process (Fig. 5.2B). Further quantification suggests that ~80% of the monocytes remained in the inner GelMA hydrogel even after 4 days of culture irrespective of the concentration of the GelMA hydrogel (Fig. 5.2C). We next assessed the effect of GelMA concentration on the growth rate of the cancer spheroids. Our results indicate the decreased GelMA concentration in the exterior hydrogel facilitated the growth of the cancer cells as the largest spheroids resulted from the 7% wt/v GelMA hydrogels after 4 days of culture (Fig. 5.2D). For all subsequent studies, the 7% wt/v GelMA hydrogels were used to create both the interior and exterior hydrogels due to the high retention of the encapsulated monocytes and its support of cancer spheroid growth.

5.4.5. Isolating the effect of cancer cell-cell contact using a dispersed cancer and immune cell co-cultures

To isolate the effect of cell-cell contact within cancer spheroids on the recruitment of T-cells into the cancer stromal, a mixture of individual cancer cells and fluorescently labeled monocytes (green) were encapsulated within the inner cylindrical hydrogel. Brightfield and fluorescent images of the encapsulated cells at Day 0 reveal the homogeneous distribution of monocytes amongst the cancer cells, which is maintained throughout culture time (Fig. 5.3A). Similar to the co-culture system containing cancer spheroids, endothelial cells are observed to form a layer at the periphery (Fig. 5.3A). Additionally, we assessed the retention of cancer cells and monocytes within the GelMA hydrogel. Using fluorescently labeled cells, the density of both cancer cells and monocytes maintained at approximately ~90% of the cell density at Day 0 after two days of culture (Fig. 5.3B). The morphology of the cancer cell and monocyte mixture was further characterized to ensure that the cancer cells remain as single cells or small clusters (2-3 cells) despite two days of culture time. XZ confocal section along with XY sections at specified vertical positions (Z1, Z2, and Z3) indicate that the cancer cells, labeled as green, and monocytes, labeled as red, remain dispersed within the inner cylindrical GelMA hydrogel (Fig. 5.3C). Furthermore, the confocal sections reveal a high density of cancer cells to recapitulate the high cell number present within a cancer spheroid (Fig. 5.3C).

5.4.6. Monocytes and cancer spheroid synergistically recruit T-cells into the cell-laden GelMA hydrogel

T-cell line, TALL-104, was allowed to extravasate from the surrounding media into GelMA hydrogels containing different cell types to determine the T-cell recruitment capacity of multi-cellular co-cultures. The following cell types were used within the bilayer hydrogel: cancer spheroid and monocytes (CS + Mo), cancer spheroid (CS), dispersed cancer cells and monocytes (DC + Mo), dispersed cancer cells alone (DC), and monocytes alone (Mo). The bright field images of GelMA hydrogels containing a cancer spheroid and monocytes immediately after T-cell infiltration assay (Day^{T} 0) show the cancer spheroid at the center of the construct surrounded by numerous single cells and an endothelial layer at the periphery (Fig. 5.4A). In addition, fluorescent images at Day^{T} 0 indicate the presence of T-cells, stained with a red fluorescent dye, at the hydrogel periphery and monocytes, stained with a green dye, near the center of the GelMA hydrogel (Fig. 5.4A, Day^{T} 0 Panel). After allowing two days for further infiltration (Day^{T} 2), fluorescent images of the same construct reveal the high distribution of T-cells (red) throughout the interior of the hydrogel and the magnified fluorescent image of the center of the hydrogel (designated by "C") show a high density of T-cells near the cancer spheroid and amongst the monocytes (green) (Fig. 5.4A, Day^{T} 2 Panel). In addition, bright field and fluorescent images of T-cell hydrogels containing different cell types at Day^{T} 2 reveal the differential recruitment of T-cells by the encapsulated cells (Fig. 5.4B). This differential T-cell recruitment into the GelMA hydrogels was quantified by examining the fraction of labeled T-cells at various normalized radial positions within the circular XY section of the hydrogel at Day^{T} 0, Day^{T} 1, and Day^{T} 2. Here, normalized radial position (R^{0}) of 0 and 1 indicates the center and the edge of the GelMA hydrogel, respectively. Our analysis indicates that hydrogels containing cancer spheroids show a higher fraction of T-cells at normalized radial positions lower than 0.56 at Day^{T} 1 and Day^{T} 2 compared to any other constructs (Fig. 5.4B-G). This indicates that the presence of a cancer spheroid better recruits T-cells compared to hydrogels containing individual cancer cells (DC and DC + Mo). Furthermore, the inclusion of monocytes with either a cancer spheroid or with individual cancer cells leads to higher T-cell presence at lower normalized positions at Day^T 1 and Day^T 2 (Fig. 5.4C-F). Interestingly, the presence of monocytes alone does not induce infiltration of T-cells into the interior as the majority of T-cells remain at high values of normalized radial positions throughout culture time (Fig. 5.4F).

To concisely summarize the recruitment of T-cells into each construct, the distribution of T-cells (DoT) within the GelMA hydrogel at Day^T 2 was calculated. Large and small values of DoT indicates that the peripheral and central location of T-cells, respectively, within the GelMA hydrogel. Using this analysis, the DoT values for hydrogels with different cell types from lowest to highest are CS + Mo < CS < DC + Mo < DC < Mo (Fig. 5.4G). This result suggests that the cancer spheroids can better recruit T-cells compared to individual cancer cells and this recruitment is further enhanced by the presence of monocytes.

5.5. Discussion

We have created a multi-cellular co-culture system containing breast cancer cells, monocytes, and endothelial cells within a microfluidics device. Moreover, we have used an additive photopatterning technique to encapsulate and position different cell types within a bilayer cylindrical hydrogel where a mixture of monocytes with a cancer spheroid or cancer cells reside in the interior and endothelial cells in the exterior hydrogel. After days of culture, the endothelial cells in the exterior were observed to form a layer at the periphery of the entire GelMA hydrogels encompassing the cell-laden scaffold. We assessed the capacity of the cancer and/or monocytes to recruit T-cells by allowing T-cells to extravasate from the surrounding media into the GelMA hydrogels. The analysis of T-cell distribution within the cell-laden construct after two days post extravasation reveals that a cancer spheroid and not individual cancer cells can significantly recruit T-cells. Additionally, the co-culture of monocytes and cancer spheroids synergistically increased T-cell recruitment although monocytes alone cannot attract T-cells.

The use of additive photopatterning approach maintained the monocyte population in the GelMA hydrogel compared to the single encapsulation process where a significant loss of monocytes was observed with culture time. The inclusion of a cancer spheroid within the hydrogel was used to attract and maintain a monocyte population within the GelMA hydrogel. This was not achieved since density of monocytes decreased by ~70% compared to Day 0 post encapsulation. Contrastingly, the additive photopatterning approach halted the loss of monocytes although the exact mechanism is unknown. However, we speculate that the presence of an interface between the two bilayers may have resulted in a physical barrier that deterred the migration of monocytes into the exterior hydrogel. The physical barrier may be an increase in rigidity at the hydrogel interface, however the validation of this hypothesis is beyond the scope of this study. Nevertheless, the TALL-104 cells infiltrating into GelMA hydrogels, containing a cancer spheroid and monocytes, traversed the bilayer interface as they are observed amongst the monocytes in the interior hydrogel. In contrast to the T-cells, the monocytes may not have the degradative capacity to overcome the increased in interfacial rigidity.

TALL-104 cells were used as a model cell line representing cytotoxic T-cells within this study due to their cytotoxic activity towards MCF7 breast cancer cells *in vitro*

(196-198). TALL-104 cells were isolated from a patient with ALL and treated with IL-2 and a co-stimulatory factor *in vitro* to induce lymphokine activated killer activity. Studies have indicated the capacity of these cells to selectively kill cancer cells originating from different tissues such as breast and brain in an MHC-independent manner (198). In addition, these cells retain key cell surface receptors implicated in chemokine-induced recruitment of cytotoxic T-cells such as CXCR3, CX3CR1, and CCR5 (199). Therefore, these cells serve as a model cell line to recapitulate the recruitment of cytotoxic T-cells or CAR T-cell recruitment into the cancer microenvironment as seen *in vivo*.

Within the study, GelMA hydrogel containing cancer spheroids were shown to recruit T-cells in contrast to single cancer cells. To isolate the effect of cell number dependent secretion of chemokines, the dispersed mixture of cancer cells and monocytes were encapsulated at high densities to recapitulate the number of cancer cells present within the spheroid. Therefore, the differential secretion of chemokines is caused the morphological difference between single cancer cells in 3D and cancer cells within a tumor spheroid. The highly dense packing of cancer cells along with the consumption of nutrients throughout the spheroid can potentially deprive the cells within the interior from nutrients as well as inhibit efficient waste removal (146). These conditions create gradients within the tumor spheroid thereby inducing unique cues that may be absent within individual cancer cells. Furthermore, the depravation of oxygen within the interior of the cancer spheroid can lead to hypoxia therefore triggering a cascade of pathways associated with HIF-1α activation (41, 146, 200). However, it is also possible that the differences observed in the recruitment of T-cells may not be attributed to nutrient depravation. The presence of cell-cell contact via cell surface receptors may induce differential secretion of chemokines, which must be explored in future studies.

5.6. Acknowledgements

AA acknowledges the support from ARCS foundation and the Ruth L. Kirschstein National Research Service Award NIH/NHLBI T32 HL 105373.

Chapter 5, in full, is currently being prepared for submission for publication of the material. “Engineered tumor-on-a-chip device with cancer-immune interactions for assessing T-cell recruitment”. Aung, Aereas; Theprungsirikul, Jomkuan; Davey, Shruti K.; Varghese, Shyni. The dissertation author is the primary investigator and author of this material.

5.7. Figures

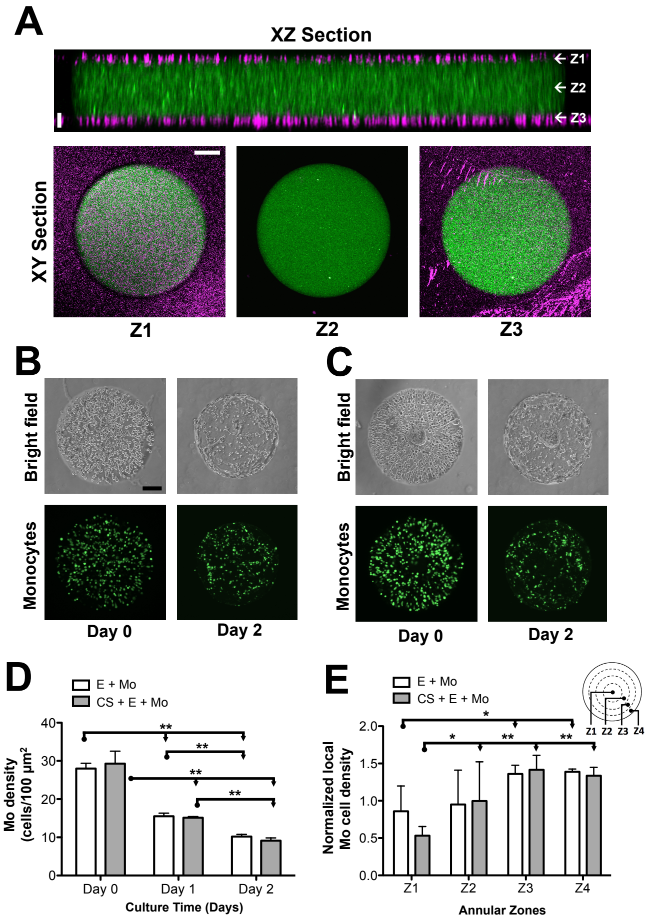

Figure 5.1: Single step encapsulation process for co-cultures of cancer cells, monocytes, and endothelial cells.

(A) XZ confocal section of a cylindrical GelMA hydrogel sandwiched between two PAm hydrogels. XY confocal sections at vertical positions Z1 and Z3 show the interface between the hydrogels and Z2 show the circular cross section of the GelMA structure. GelMA and PAm hydrogels are embedded with green and magenta particles, respectively, for visualization of the hydrogels. Horizontal scale bar: 200 µm. Vertical scale bar: 20 µm. Bright field and fluorescent images of GelMA hydrogels containing a co-culture of endothelial and monocytes (B) or cancer spheroid, monocytes, and endothelial cells (C) immediately after encapsulation, Day 0, and after two days of culture, Day 2. Scale bar: 200 µm. Monocyte density within the GelMA hydrogels as a function of culture time (D) and within the zones, Z1 through Z4, after two days of culture (E) in the absence (white) and presence (shaded) of a cancer spheroid. Cancer spheroids, monocytes, and endothelial cells are denoted by CS, Mo, and E, respectively. * and ** indicate statistically significant differences of $p < 0.05$ and 0.01, respectively, as obtained from pair wise t-test between samples designated by • and ➔.

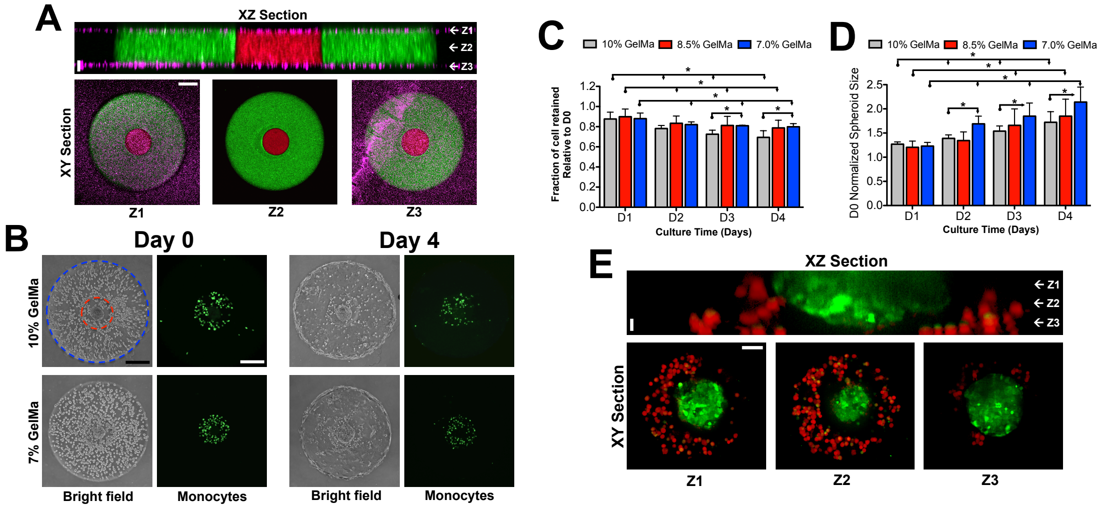

Figure 5.2: Additive photoencapsulation process for a spatially controlled co-culture of cancer spheroid, monocytes and endothelial cells.

(A) XZ confocal section of a bilayer GelMA hydrogel comprised of two concentric cylinders sandwiched by PAm hydrogels at the top and bottom surfaces. XY confocal sections at vertical positions, Z1 through Z3, show the interface between GelMA and PAm hydrogel as well as the cross section of the bilayer structure. The interior and exterior GelMA hydrogels are labeled with red and green fluorescent particles, respectively, while the PAm hydrogels are labeled with magenta fluorescent particles. (B) Brightfield and fluorescent images of GelMA hydrogels embedded cells post-encapsulation (Day 0) and after two days in culture (Day 4). The interior hydrogel contains fluorescently labeled monocytes (green) while the exterior contains endothelial cells. Red and blue lines designate the boundaries of the interior and exterior hydrogels, respectively. Top and bottom rows show cell-laden constructs with 7% and 10% GelMA concentration for the exterior hydrogels. Scale bar: 200 µm. Day 0 normalized number of monocytes (C) and cancer spheroid size within the GelMA hydrogel (D) as a function of culture time, D1 through D4, and exterior GelMA hydrogel concentration, 10%, 8.5%, and 7% wt/v. * and ** indicate statistically significant differences of $p < 0.05$ and 0.01, respectively, as obtained from pair wise t-test between samples designated by • and ➔.

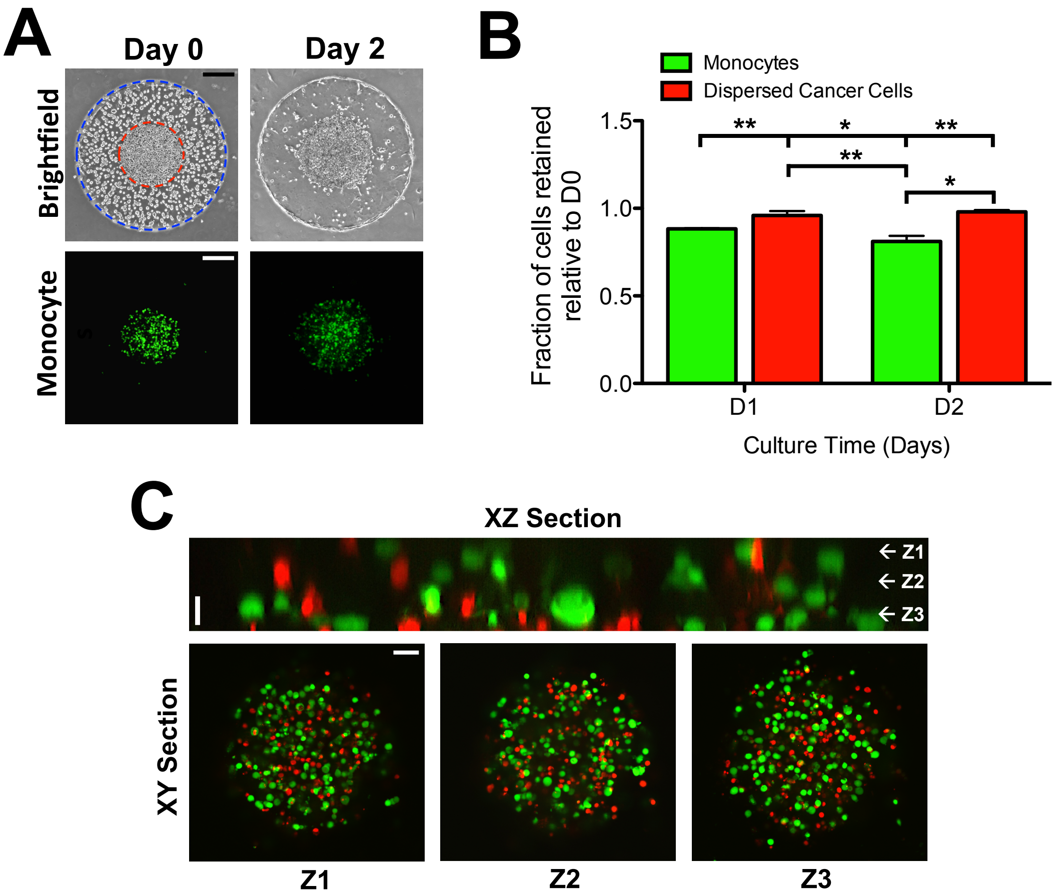

Figure 5.3: Co-culture system with dispersed cancer cells, monocytes, and endothelial cells.

(A) Brightfield and fluorescent images of cell-laden bilayer GelMA hydrogel. The interior hydrogel contains a mixture of cancer cells and fluorescently labeled monocytes while the exterior contains endothelial cells. The boundaries of the interior and exterior hydrogels are lined with red and blue circles, respectively. (B) Quantification of normalized monocyte (white) and cancer cell (shaded) number within the GelMA hydrogel as a function of culture time. (C) Confocal sections of dispersed cancer cell and monocyte mixture in the interior of the bilayer GelMA hydrogel. XZ section along with XY section as at labeled vertical positions (Z1-Z3) show homogeneously distributed cancer cells and monocytes. Here, cancer cells and monocytes are labeled as green and red, respectively. Horizontal scale bar: 200 µm. Vertical scale bar: 20 µm. * and ** indicate statistically significant differences of $p < 0.05$ and 0.01, respectively, as obtained from pair wise t-test between samples designated by • and ➔.

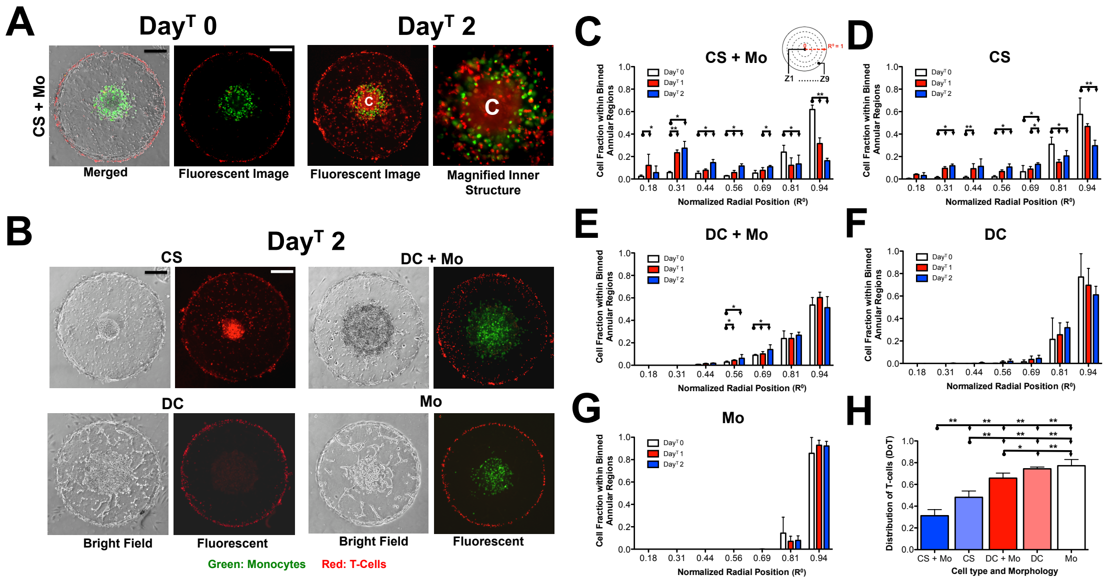

Figure 5.4: TALL-104 cell infiltration into bilayer GelMA hydrogels laden with cells.

(A, Day^{T}0 Panel) Merged and fluorescent image of bilayer GelMA hydrogels containing a cancer spheroid, fluorescently labeled monocytes, endothelial cells, and fluorescently labeled T-cells (CS + Mo) immediately after T-cell infiltration assay, Day^T 0. (A, Day^T 2 Panel) Fluorescent image of the entire hydrogel and magnified center of the hydrogel two days post-infiltration (Day^T 2). The center of the hydrogel is designated by the letter "C". (B) Brightfield and fluorescent image of the bilayer hydrogels with cancer spheroid (CS), dispersed caner cells and monocytes (DC + Mo), dispersed cancer cells (DC), and monocytes (Mo) in the interior hydrogel at Day^T 2. Monocytes and T-cells are labeled with green and red dye, respectively. (C-G) Fraction of cells residing within each annular region, diagram shown in the inset from Day^T 0 to Day^T 2 for hydrogels containing CS + Mo, CS, DC + Mo, DC, and Mo. The normalized radial position denotes the radial midpoint location in each annulus. (H) Quantification of the Distribution of T-cells (DoT) for hydrogels containing different cell types and morphologies. DoT is calculated from $\sum_{i=1}^{n} m_i r_i^2$, where i is an individual T-cell, n is the total number of T-cells throughout the construct at Day^T 2, m_i is $1/n$, and r_i is the distance between the center of the bilayer GelMA hydrogel to the centroid of a particular T-cell. Lower and higher DoT values indicate the distribution of T-cells towards the center and periphery, respectively. * and ** indicate statistically significant differences of $p < 0.05$ and 0.01, respectively, as obtained from pair wise t-test between samples designated by • and ➔.

Chapter 6: Future Directions

Within this thesis, I have investigated the interplay between traction force and protease activity within cancer cells invading in to an ECM network. The findings from this study indicate that the cells must reach a force threshold prior to proteolysis triggered by transport of MT1-MMP from the cytoplasm to the cell surface. In addition, I have explored the pathway by which MT1-MMP is transported by investigating the role of CARTS pathway during cancer cell invasion. I have shown that MT1-MMP is packaged within Golgi vesicles involved in the CARTS pathway and is transported to the cell surface along with a known CARTS pathway cargo. Furthermore, the disruption of this transport pathway was shown to abrogate the invasion process. In addition to investigating the invasion of cancer cells, I have created *in vitro* platforms recapitulating the cancer microenvironment using a combination of 3D photopatterning and microfluidics technology developed within our lab. To this end, I developed a tumor-on-a-chip system containing cancer spheroids entrapped within an ECM network and encompassed within an endothelial barrier at the periphery. The encapsulated cells exhibited a dose-dependent response to doxorubicin thereby illustrating the platform's capacity to serve as a drug-screening tool. Lastly, I have improved upon this system by using an additive photopatterning technique to incorporate monocytes and tune the morphology of cancer cell to study the effect of cancer-immune interactions on the recruitment of cytotoxic T-cells.

Within the co-culture system containing cancer cells, monocytes, and endothelial cells, the differential recruitment of cytotoxic T-cells were observed as a function of cell morphology and cell type. Further investigation into the differences in soluble factors causing the differential recruitment could be of great interest. Using mass spectrometry, we can identify the soluble factors unique to each culture combinations and further investigate into these factors. This form of analysis may uncover unique factors beyond known chemokines or uncover chemokines that may not have been considered to influence the recruitment of cytotoxic T-cells.

The use of monocytes polarized towards M1 or M2 phenotypes in place of monocytes may yet increase the complexity and physiological relevancy of this system. Here, the polarization towards M2 phenotypes can create a pro-tumor microenvironment that may potentially curb T-cell infiltration. Contrastingly, the presence of M1 macrophages will generate an inflamed microenvironment, which will affect T-cell infiltration. Furthermore, the incorporation of other cell types such as fibroblasts, which play a vital pro-tumor role in the cancer micro environment, may be needed to increase the complexity of this *in vitro* system. Nevertheless, the use of mass spectroscopy to identify soluble factors within this co-culture system uncovers novel interactions that would otherwise be difficult within an *in vivo* model.

Beyond investigating the infiltration of T-cells, the fluidics-based co-culture platform containing cancer and immune cells can be used to study the recruitment of other types of immune cells. These studies in particular may require the use of peripheral blood mononuclear cells (PBMC) where a plethora of immune cell types exists. In this manner, evolution of the cancer immune contexture can be recapitulated *in vitro* in a controlled manner to better understand how this microenvironment was generated *in vivo*. To this end, the use of particular cell types within the co-culture system is crucial due the capacity for cross reactivity of immune cells towards cell lines. Therefore, syngeneic cancer cell lines along with murine PBMCs may prove to be the optimal pairing that is needed to execute this study.

The co-culture system described within this thesis provides a 3D microenvironment, allows for positioning and compartmentalization of different cell types, and provides perfusion of media that can be used to allow cells to extravasate into the cell-laden hydrogels. The versatility of this platform creates endless opportunities to closely recapitulate the *in vivo* microenvironment especially for complex phenomena such as cancer-immune interactions. Such a technology can be an invaluable tool in furthering the capacity of immunotherapies, which hold the highest potential in curing the cancer epidemic.

References

1. American Cancer Society. 2016. Cancer Facts & Figures 2016.
2. Cekanova, M., and K. Rathore. 2014. Animal models and therapeutic molecular targets of cancer: utility and limitations. Drug Des Dev Ther 8:1911-1922.
3. Sharpless, N. E., and R. A. DePinho. 2006. Model organisms - The mighty mouse: genetically engineered mouse models in cancer drug development. Nat Rev Drug Discov 5:741-754.
4. Frese, K. K., and D. A. Tuveson. 2007. Maximizing mouse cancer models. Nat Rev Cancer 7:645-658.
5. Cheon, D. J., and S. Orsulic. 2011. Mouse Models of Cancer. Annu Rev Pathol-Mech 6:95-119.
6. Zhang, Z., and S. Nagrath. 2013. Microfluidics and cancer: are we there yet? Biomed Microdevices 15:595-609.
7. Ying, L., and Q. Wang. 2013. Microfluidic chip-based technologies: emerging platforms for cancer diagnosis. Bmc Biotechnol 13.
8. Peter Friedl, K. w. 2009. Plasticity of cell migration: a multiscale tuning model. Journal of Cell Biology 188:11-19.
9. Friedl, P. 2004. Prespecification and plasticity: shifting mechanisms of cell migration. Curr Opin Cell Biol 16:14-23.
10. Lammermann, T., and M. Sixt. 2009. Mechanical modes of 'amoeboid' cell migration. Curr Opin Cell Biol 21:636-644.
11. Lammermann, T., B. L. Bader, S. J. Monkley, T. Worbs, R. Wedlich-Soldner, K. Hirsch, M. Keller, R. Forster, D. R. Critchley, R. Fassler, and M. Sixt. 2008. Rapid leukocyte migration by integrin-independent flowing and squeezing. Nature 453:51-+.
12. Poincloux, R., O. Collin, F. Lizarraga, M. Romao, M. Debray, M. Piel, and P. Chavrier. 2011. Contractility of the cell rear drives invasion of breast tumor cells in 3D Matrigel. P Natl Acad Sci USA 108:1943-1948.
13. Sanz-Moreno, V., and C. J. Marshall. 2009. Rho-GTPase signaling drives melanoma cell plasticity. Cell Cycle 8:1484-1487.
14. Yoshida, K., and T. Soldati. 2006. Dissection of amoeboid movement into two mechanically distinct modes. J Cell Sci 119:3833-3844.

15. Miron-Mendoza, M., J. Seemann, and F. Grinnell. 2008. Collagen fibril flow and tissue translocation coupled to fibroblast migration in 3D collagen matrices. Mol Biol Cell 19:2051-2058.

16. Lauffenburger, D. A., and A. F. Horwitz. 1996. Cell migration: A physically integrated molecular process. Cell 84:359-369.

17. Harley, B. A. C., H. D. Kim, M. H. Zaman, I. V. Yannas, D. A. Lauffenburger, and L. J. Gibson. 2008. Microarchitecture of three-dimensional scaffolds influences cell migration behavior via junction interactions. Biophys J 95:4013-4024.

18. Haston, W. S., J. M. Shields, and P. C. Wilkinson. 1982. Lymphocyte Locomotion and Attachment on Two-Dimensional Surfaces and in 3-Dimensional Matrices. Journal of Cell Biology 92:747-752.

19. Provenzano, P. P., D. R. Inman, K. W. Eliceiri, S. M. Trier, and P. J. Keely. 2008. Contact Guidance Mediated Three-Dimensional Cell Migration is Regulated by Rho/ROCK-Dependent Matrix Reorganization. Biophys J 95:5374-5384.

20. Kirmse, R., H. Otto, and T. Ludwig. 2011. Interdependency of cell adhesion, force generation and extracellular proteolysis in matrix remodeling. J Cell Sci 124:1857-1866.

21. Beningo, K. A., M. Dembo, I. Kaverina, J. V. Small, and Y. L. Wang. 2001. Nascent focal adhesions are responsible for the generation of strong propulsive forces in migrating fibroblasts. Journal of Cell Biology 153:881-887.

22. Blaser, H., M. Reichman-Fried, I. Castanon, K. Dumstrei, F. L. Marlow, K. Kawakami, L. Solnica-Krezel, C. P. Heisenberg, and E. Raz. 2006. Migration of zebrafish primordial germ cells: A role for myosin contraction and cytoplasmic flow. Dev Cell 11:613-627.

23. Kramer, N., A. Walzl, C. Unger, M. Rosner, G. Krupitza, M. Hengstschlager, and H. Dolznig. 2013. In vitro cell migration and invasion assays. Mutat Res-Rev Mutat 752:10-24.

24. Yang, Y. L., L. M. Leone, and L. J. Kaufman. 2009. Elastic Moduli of Collagen Gels Can Be Predicted from Two-Dimensional Confocal Microscopy. Biophys J 97:2051-2060.

25. Zaman, M. H., L. M. Trapani, A. L. Sieminski, D. Mackellar, H. Gong, R. D. Kamm, A. Wells, D. A. Lauffenburger, and P. Matsudaira. 2006. Migration of tumor cells in 3D matrices is governed by matrix stiffness along with cell-matrix adhesion and proteolysis. P Natl Acad Sci USA 103:10889-10894.

26. Hamilton, N. 2009. Quantification and its Applications in Fluorescent Microscopy Imaging. Traffic 10:951-961.

27. Polackwich, R. J., D. Koch, R. Arevalo, A. M. Miermont, K. J. Jee, J. Lazar, J. Urbach, S. C. Mueller, and R. G. McAllister. 2013. A Novel 3D Fibril Force Assay Implicates Src in Tumor Cell Force Generation in Collagen Networks. Plos One 8.

28. Koch, T. M., S. Munster, N. Bonakdar, J. P. Butler, and B. Fabry. 2012. 3D Traction forces in cancer cell invasion. Plos One 7:e33476.

29. Knupfer, M. M., F. Pulzer, I. Schindler, P. H. Driever, H. Knupfer, and E. Keller. 2001. Different effects of valproic acid on proliferation and migration of malignant glioma cells in vitro. Anticancer Res 21:347-351.

30. Konduri, S. D., A. Tasiou, N. Chandrasekar, and J. S. Rao. 2001. Overexpression of tissue factor pathway inhibitor-2 (TFPI-2), decreases the invasiveness of prostate cancer cells in vitro. Int J Oncol 18:127-131.

31. Kam, Y., C. Guess, L. Estrada, B. Weidow, and V. Quaranta. 2008. A novel circular invasion assay mimics in vivo invasive behavior of cancer cell lines and distinguishes single-cell motility in vitro. Bmc Cancer 8.

32. Albini, A., and R. Benelli. 2007. The chemoinvasion assay: a method to assess tumor and endothelial cell invasion and its modulation. Nat Protoc 2:504-511.

33. Albini, A., Y. Iwamoto, H. K. Kleinman, G. R. Martin, S. A. Aaronson, J. M. Kozlowski, and R. N. Mcewan. 1987. A Rapid Invitro Assay for Quantitating the Invasive Potential of Tumor-Cells. Cancer Res 47:3239-3245.

34. Marshall, J. 2011. Transwell (R) Invasion Assays. Methods Mol Biol 769:97-110.

35. Aung, A., Y. N. Seo, S. Y. Lu, Y. X. Wang, C. Jamora, J. C. del Alamo, and S. Varghese. 2014. 3D Traction Stresses Activate Protease-Dependent Invasion of Cancer Cells. Biophys J 107:2528-2537.

36. Gaggioli, C., S. Hooper, C. Hidalgo-Carcedo, R. Grosse, J. F. Marshall, K. Harrington, and E. Sahai. 2007. Fibroblast-led collective invasion of carcinoma cells with differing roles for RhoGTPases in leading and following cells. Nat Cell Biol 9:1392-U1392.

37. Kunz-Schughart, L. A. 1999. Multicellular tumor spheroids: intermediates between monolayer culture and in vivo tumor. Cell Biol Int 23:157-161.

38. Hsiao, A. Y., Y. S. Torisawa, Y. C. Tung, S. Sud, R. S. Taichman, K. J. Pienta, and S. Takayama. 2009. Microfluidic system for formation of PC-3 prostate cancer co-culture spheroids. Biomaterials 30:3020-3027.

39. Hsiao, A. Y., Y. C. Tung, X. G. Qu, L. R. Patel, K. J. Pienta, and S. Takayama. 2012. 384 hanging drop arrays give excellent Z-factors and allow versatile formation of co-culture spheroids. Biotechnol Bioeng 109:1293-1304.

40. Minchinton, A. I., and I. F. Tannock. 2006. Drug penetration in solid tumours. Nat Rev Cancer 6:583-592.

41. Doublier, S., D. C. Belisario, M. Polimeni, L. Annaratone, C. Riganti, E. Allia, D. Ghigo, A. Bosia, and A. Sapino. 2012. HIF-1 activation induces doxorubicin resistance in MCF7 3-D spheroids via P-glycoprotein expression: a potential model of the chemoresistance of invasive micropapillary carcinoma of the breast. Bmc Cancer 12.

42. Walsh, C. L., B. M. Babin, R. W. Kasinskas, J. A. Foster, M. J. McGarry, and N. S. Forbes. 2009. A multipurpose microfluidic device designed to mimic microenvironment gradients and develop targeted cancer therapeutics. Lab Chip 9:545-554.

43. Sabhachandani, P., V. Motwani, N. Cohen, S. Sarkar, V. Torchilin, and T. Konry. 2016. Generation and functional assessment of 3D multicellular spheroids in droplet based microfluidics platform. Lab Chip 16:497-505.

44. Kwapiszewska, K., A. Michalczuk, M. Rybka, R. Kwapiszewski, and Z. Brzozka. 2014. A microfluidic-based platform for tumour spheroid culture, monitoring and drug screening. Lab Chip 14:2096-2104.

45. Ehsan, S. M., K. M. Welch-Reardon, M. L. Waterman, C. C. W. Hughes, and S. C. George. 2014. A three-dimensional in vitro model of tumor cell intravasation. Integr Biol-Uk 6:603-610.

46. Bersini, S., J. S. Jeon, R. D. Kamm, and M. Moretti. 2015. Human 3D Vascularized Organotypic Microfluidic Models for the Study of Breast Cancer Cell Extravasation. Tissue Eng Pt A 21:S207-S207.

47. Jeon, J. S., S. Bersini, M. Gilardi, G. Dubini, J. L. Charest, M. Moretti, and R. D. Kamm. 2015. Human 3D vascularized organotypic microfluidic assays to study breast cancer cell extravasation (vol 112, pg 214, 2014). P Natl Acad Sci USA 112:E818-E818.

48. Zervantonakis, I. K., S. K. Hughes-Alford, J. L. Charest, J. S. Condeelis, F. B. Gertler, and R. D. Kamm. 2012. Three-dimensional microfluidic model for tumor cell intravasation and endothelial barrier function. P Natl Acad Sci USA 109:13515-13520.

49. Albanese, A., A. K. Lam, E. A. Sykes, J. V. Rocheleau, and W. C. W. Chan. 2013. Tumour-on-a-chip provides an optical window into nanoparticle tissue transport.

Nat Commun 4.

50. Bhatia, S. N., and D. E. Ingber. 2014. Microfluidic organs-on-chips. Nat Biotechnol 32:760-772.

51. Esch, E. W., A. Bahinski, and D. Huh. 2015. Organs-on-chips at the frontiers of drug discovery. Nat Rev Drug Discov 14:248-260.

52. Sung, J. H., M. B. Esch, and M. L. Shuler. 2010. Integration of in silico and in vitro platforms for pharmacokinetic-pharmacodynamic modeling. Expert Opin Drug Met 6:1063-1081.

53. Sung, J. H., C. Kam, and M. L. Shuler. 2010. A microfluidic device for a pharmacokinetic-pharmacodynamic (PK-PD) model on a chip. Lab Chip 10:446-455.

54. LoRusso, P. M., S. Prakash, A. Wozniak, L. Flaherty, M. Zalupski, A. Shields, H. Sands, R. Parchment, and B. Jasti. 2002. Phase I clinical trial of 5-fluoro-pyrimidinone (5FP), an oral prodrug of 5-fluorouracil (5FU). Invest New Drug 20:63-71.

55. Albini, A., G. Pennesi, F. Donatelli, R. Cammarota, S. De Flora, and D. M. Noonan. 2010. Cardiotoxicity of Anticancer Drugs: The Need for Cardio-Oncology and Cardio-Oncological Prevention. Jnci-J Natl Cancer I 102:14-25.

56. Wolchok, J. D. 2015. Melanoma.

57. Ledford, H. 2013. Immunotherapy's cancer remit widens. Nature 497:544-544.

58. Smyth, M. J., G. P. Dunn, and R. D. Schreiber. 2006. Cancer immunosurveillance and immunoediting: The roles of immunity in suppressing tumor development and shaping tumor immunogenicity. Adv Immunol 90:1-50.

59. Dunn, G. P., A. T. Bruce, H. Ikeda, L. J. Old, and R. D. Schreiber. 2002. Cancer immunoediting: from immunosurveillance to tumor escape. Nat Immunol 3:991-998.

60. Shankaran, V., H. Ikeda, A. T. Bruce, J. M. White, P. E. Swanson, L. J. Old, and R. D. Schreiber. 2001. IFN gamma and lymphocytes prevent primary tumour development and shape tumour immunogenicity. Nature 410:1107-1111.

61. Loeb, L. A., K. R. Loeb, and J. P. Anderson. 2003. Multiple mutations and cancer. P Natl Acad Sci USA 100:776-781.

62. Lengauer, C., K. W. Kinzler, and B. Vogelstein. 1998. Genetic instabilities in human cancers. Nature 396:643-649.

63. Phan, G. Q., E. Wang, and F. M. Marincola. 2001. T-cell-directed cancer vaccines: mechanisms of immune escape and immune tolerance. Expert Opin Biol Th 1:511-523.

64. Algarra, I., T. Cabrera, and F. Garrido. 2000. The HLA crossroad in tumor immunology. Hum Immunol 61:65-73.

65. He, J. B., Y. Hu, M. M. Hu, and B. L. Li. 2015. Development of PD-1/PD-L1 Pathway in Tumor Immune Microenvironment and Treatment for Non-Small Cell Lung Cancer. Sci Rep 5.

66. Knutson, K. L., and M. L. Disis. 2005. Tumor antigen-specific T helper cells in cancer immunity and immunotherapy. Cancer Immunol Immun 54:721-728.

67. Fridman, W. H., F. Pages, C. Sautes-Fridman, and J. Galon. 2012. The immune contexture in human tumours: impact on clinical outcome. Nat Rev Cancer 12:298-306.

68. Noy, R., and J. W. Pollard. 2014. Tumor-Associated Macrophages: From Mechanisms to Therapy (vol 41, pg 49, 2014). Immunity 41:866-866.

69. Bloch, O., C. A. Crane, R. Kaur, M. Safaee, M. J. Rutkowski, and A. T. Parsa. 2013. Gliomas Promote Immunosuppression through Induction of B7-H1 Expression in Tumor-Associated Macrophages. Clin Cancer Res 19:3165-3175.

70. Ng, T. H. S., G. J. Britton, E. V. Hill, J. Verhagen, B. R. Burton, and D. C. Wraith. 2013. Regulation of adaptive immunity; the role of interleukin-10. Front Immunol 4.

71. Oh, S. A., and M. O. Li. 2013. TGF-beta: Guardian of T Cell Function. J Immunol 191:3973-3979.

72. Sangaletti, S., E. Di Carlo, S. Gariboldi, S. Miotti, B. Cappetti, M. Parenza, C. Rumio, R. A. Brekken, C. Chiodoni, and M. P. Colombo. 2008. Macrophage-Derived SPARC Bridges Tumor Cell-Extracellular Matrix Interactions toward Metastasis. Cancer Res 68:9050-9059.

73. Quail, D. F., and J. A. Joyce. 2013. Microenvironmental regulation of tumor progression and metastasis. Nat Med 19:1423-1437.

74. Condeelis, J., and J. W. Pollard. 2006. Macrophages: Obligate partners for tumor cell migration, invasion, and metastasis. Cell 124:263-266.

75. Hanahan, D., and R. A. Weinberg. 2011. Hallmarks of Cancer: The Next Generation. Cell 144:646-674.

76. Tripathi, C., B. N. Tewari, R. K. Kanchan, K. S. Baghel, N. Nautiyal, R.

Shrivastava, H. Kaur, M. L. B. Bhatt, and S. Bhadauria. 2014. Macrophages are recruited to hypoxic tumor areas and acquire a Pro-Angiogenic M2-Polarized phenotype via hypoxic cancer cell derived cytokines Oncostatin M and Eotaxin. Oncotarget 5:5350-5368.

77. Lee, D. W., D. M. Barrett, C. Mackall, R. Orentas, and S. A. Grupp. 2012. The Future Is Now: Chimeric Antigen Receptors as New Targeted Therapies for Childhood Cancer. Clin Cancer Res 18:2780-2790.

78. Sharma, R. K., Z. S. Chheda, V. R. Jala, and B. Haribabu. 2015. Regulation of cytotoxic T-Lymphocyte trafficking to tumors by chemoattractants: implications for immunotherapy. Expert Rev Vaccines 14:537-549.

79. Viola, A., and A. D. Luster. 2008. Chemokines and their receptors: Drug targets in immunity and inflammation. Annu Rev Pharmacol 48:171-197.

80. Li, J., M. O'Malley, P. Sampath, P. Kalinski, D. L. Bartlett, and S. H. Thorne. 2012. Expression of CCL19 from Oncolytic Vaccinia Enhances Immunotherapeutic Potential while Maintaining Oncolytic Activity. Neoplasia 14:1115-+.

81. Wolf, K., and P. Friedl. 2011. Extracellular matrix determinants of proteolytic and non-proteolytic cell migration. Trends Cell Biol 21:736-744.

82. Moya, M., D. Tran, and S. C. George. 2013. An integrated in vitro model of perfused tumor and cardiac tissue. Stem Cell Res Ther 4.

83. Chaffer, C. L., and R. A. Weinberg. 2011. A perspective on cancer cell metastasis. Science 331:1559-1564.

84. Sabeh, F., R. Shimizu-Hirota, and S. J. Weiss. 2009. Protease-dependent versus -independent cancer cell invasion programs: three-dimensional amoeboid movement revisited. J Cell Biol 185:11-19.

85. Wolf, K., I. Mazo, H. Leung, K. Engelke, U. H. von Andrian, E. I. Deryugina, A. Y. Strongin, E. B. Brocker, and P. Friedl. 2003. Compensation mechanism in tumor cell migration: mesenchymal-amoeboid transition after blocking of pericellular proteolysis. J Cell Biol 160:267-277.

86. Wolf, K., M. Te Lindert, M. Krause, S. Alexander, J. Te Riet, A. L. Willis, R. M. Hoffman, C. G. Figdor, S. J. Weiss, and P. Friedl. 2013. Physical limits of cell migration: Control by ECM space and nuclear deformation and tuning by proteolysis and traction force. J Cell Biol 201:1069-1084.

87. Wirtz, D., K. Konstantopoulos, and P. C. Searson. 2011. The physics of cancer: the role of physical interactions and mechanical forces in metastasis. Nature reviews. Cancer 11:512-522.

88. Pathak, A., and S. Kumar. 2012. Independent regulation of tumor cell migration by matrix stiffness and confinement. P Natl Acad Sci USA 109:10334-10339.

89. Friedl, P., and S. Alexander. 2011. Cancer invasion and the microenvironment: plasticity and reciprocity. Cell 147:992-1009.

90. Jerrell, R. J., and A. Parekh. 2014. Cellular traction stresses mediate extracellular matrix degradation by invadopodia. Acta Biomater 10:1886-1896.

91. Alexander, N. R., K. M. Branch, A. Parekh, E. S. Clark, I. C. Iwueke, S. A. Guelcher, and A. M. Weaver. 2008. Extracellular matrix rigidity promotes invadopodia activity. Curr Biol 18:1295-1299.

92. Butcher, D. T., T. Alliston, and V. M. Weaver. 2009. A tense situation: forcing tumour progression. Nature reviews. Cancer 9:108-122.

93. Levental, K. R., H. Yu, L. Kass, J. N. Lakins, M. Egeblad, J. T. Erler, S. F. Fong, K. Csiszar, A. Giaccia, W. Weninger, M. Yamauchi, D. L. Gasser, and V. M. Weaver. 2009. Matrix crosslinking forces tumor progression by enhancing integrin signaling. Cell 139:891-906.

94. Tse, J. M., G. Cheng, J. A. Tyrrell, S. A. Wilcox-Adelman, Y. Boucher, R. K. Jain, and L. L. Munn. 2012. Mechanical compression drives cancer cells toward invasive phenotype. P Natl Acad Sci USA 109:911-916.

95. Mierke, C. T., N. Bretz, and P. Altevogt. 2011. Contractile forces contribute to increased glycosylphosphatidylinositol-anchored receptor CD24-facilitated cancer cell invasion. J Biol Chem 286:34858-34871.

96. Guck, J., S. Schinkinger, B. Lincoln, F. Wottawah, S. Ebert, M. Romeyke, D. Lenz, H. M. Erickson, R. Ananthakrishnan, D. Mitchell, J. Kas, S. Ulvick, and C. Bilby. 2005. Optical deformability as an inherent cell marker for testing malignant transformation and metastatic competence. Biophys J 88:3689-3698.

97. Hur, S. S., Y. Zhao, Y. S. Li, E. Botvinick, and S. Chien. 2009. Live Cells Exert 3-Dimensional Traction Forces on Their Substrata. Cell Mol Bioeng 2:425-436.

98. Gospodarowicz, D., R. Gonzalez, and D. K. Fujii. 1983. Are factors originating from serum, plasma, or cultured cells involved in the growth-promoting effect of the extracellular matrix produced by cultured bovine corneal endothelial cells? J Cell Physiol 114:191-202.

99. Dimitriadis, E. K., F. Horkay, J. Maresca, B. Kachar, and R. S. Chadwick. 2002. Determination of elastic moduli of thin layers of soft material using the atomic force microscope. Biophys J 82:2798-2810.

100. del Alamo, J. M., R.; Alvarez-Gonzalez, B; Alonso-Latorre, B; Firtel, RA;

Lasheras, JC. in press. Three-Dimensional Quantification of Cellular Traction Forces and Mechanosensing of Thin Substrata by Fourier Traction Force Microscopy. Plos One.

101. Ouyang, M., J. Sun, S. Chien, and Y. Wang. 2008. Determination of hierarchical relationship of Src and Rac at subcellular locations with FRET biosensors. P Natl Acad Sci USA 105:14353-14358.

102. Lu, S., M. Ouyang, J. Seong, J. Zhang, S. Chien, and Y. Wang. 2008. The spatiotemporal pattern of Src activation at lipid rafts revealed by diffusion-corrected FRET imaging. PLoS Comput Biol 4:e1000127.

103. Lu, S., T. J. Kim, C. E. Chen, M. Ouyang, J. Seong, X. Liao, and Y. Wang. 2011. Computational analysis of the spatiotemporal coordination of polarized PI3K and Rac1 activities in micro-patterned live cells. Plos One 6:e21293.

104. Troeberg, L., and H. Nagase. 2003. Measurement of matrix metalloproteinase activities in the medium of cultured synoviocytes using zymography. Methods in molecular biology 225:77-87.

105. Ilina, O., G. J. Bakker, A. Vasaturo, R. M. Hofmann, and P. Friedl. 2011. Two-photon laser-generated microtracks in 3D collagen lattices: principles of MMP-dependent and -independent collective cancer cell invasion. Phys Biol 8:015010.

106. Friedl, P., and K. Wolf. 2010. Plasticity of cell migration: a multiscale tuning model. J Cell Biol 188:11-19.

107. del Alamo, J. C., R. Meili, B. Alvarez-Gonzalez, B. Alonso-Latorre, E. Bastounis, R. Firtel, and J. C. Lasheras. 2013. Three-dimensional quantification of cellular traction forces and mechanosensing of thin substrata by fourier traction force microscopy. Plos One 8:e69850.

108. Del Alamo, J. C., R. Meili, B. Alonso-Latorre, J. Rodriguez-Rodriguez, A. Aliseda, R. A. Firtel, and J. C. Lasheras. 2007. Spatio-temporal analysis of eukaryotic cell motility by improved force cytometry. P Natl Acad Sci USA 104:13343-13348.

109. Butler, J. P., I. M. Tolic-Norrelykke, B. Fabry, and J. J. Fredberg. 2002. Traction fields, moments, and strain energy that cells exert on their surroundings. Am J Physiol Cell Physiol 282:C595-605.

110. Legant, W. R., J. S. Miller, B. L. Blakely, D. M. Cohen, G. M. Genin, and C. S. Chen. 2010. Measurement of mechanical tractions exerted by cells in three-dimensional matrices. Nat Methods 7:969-971.

111. Khetan, S., M. Guvendiren, W. R. Legant, D. M. Cohen, C. S. Chen, and J. A. Burdick. 2013. Degradation-mediated cellular traction directs stem cell fate in

covalently crosslinked three-dimensional hydrogels. Nat Mater 12:458-465.

112. Bloom, R. J., J. P. George, A. Celedon, S. X. Sun, and D. Wirtz. 2008. Mapping local matrix remodeling induced by a migrating tumor cell using three-dimensional multiple-particle tracking. Biophys J 95:4077-4088.

113. Khatau, S. B., R. J. Bloom, S. Bajpai, D. Razafsky, S. Zang, A. Giri, P. H. Wu, J. Marchand, A. Celedon, C. M. Hale, S. X. Sun, D. Hodzic, and D. Wirtz. 2012. The distinct roles of the nucleus and nucleus-cytoskeleton connections in three-dimensional cell migration. Sci Rep 2:488.

114. Reed, J., W. J. Walczak, O. N. Petzold, and J. K. Gimzewski. 2009. In situ mechanical interferometry of matrigel films. Langmuir 25:36-39.

115. Poincloux, R., F. Lizarraga, and P. Chavrier. 2009. Matrix invasion by tumour cells: a focus on MT1-MMP trafficking to invadopodia. J Cell Sci 122:3015-3024.

116. Schoumacher, M., R. D. Goldman, D. Louvard, and D. M. Vignjevic. 2010. Actin, microtubules, and vimentin intermediate filaments cooperate for elongation of invadopodia. J Cell Biol 189:541-556.

117. Buccione, R., J. D. Orth, and M. A. McNiven. 2004. Foot and mouth: podosomes, invadopodia and circular dorsal ruffles. Nat Rev Mol Cell Biol 5:647-657.

118. Yu, X. Z., and L. M. Machesky. 2012. Cells Assemble Invadopodia-Like Structures and Invade into Matrigel in a Matrix Metalloprotease Dependent Manner in the Circular Invasion Assay. Plos One 7.

119. Artym, V. V., Y. Zhang, F. O. Seillier-Moiseiwitsch, K. M. Yamada, and S. C. Mueller. 2006. Dynamic interactions of cortactin and membrane type 1 matrix metalloproteinase at invadopodia: Defining the stages of invadopodia formation and function. Cancer Res 66:3034-3043.

120. Bergert, M., S. D. Chandradoss, R. A. Desai, and E. Paluch. 2012. Cell mechanics control rapid transitions between blebs and lamellipodia during migration. P Natl Acad Sci USA 109:14434-14439.

121. Giri, A., S. Bajpai, N. Trenton, H. Jayatilaka, G. D. Longmore, and D. Wirtz. 2013. The Arp2/3 complex mediates multigeneration dendritic protrusions for efficient 3-dimensional cancer cell migration. Faseb J.

122. Lu, S., Y. Wang, H. Huang, Y. Pan, E. J. Chaney, S. A. Boppart, H. Ozer, and A. Y. Strongin. 2013. Quantitative FRET imaging to visualize the invasiveness of live breast cancer cells. Plos One 8:e58569.

123. Trappmann, B., J. E. Gautrot, J. T. Connelly, D. G. Strange, Y. Li, M. L. Oyen, M. A. Cohen Stuart, H. Boehm, B. Li, V. Vogel, J. P. Spatz, F. M. Watt, and W. T.

Huck. 2012. Extracellular-matrix tethering regulates stem-cell fate. Nat Mater 11:642-649.

124. Ayala, R., C. Zhang, D. Yang, Y. Hwang, A. Aung, S. S. Shroff, F. T. Arce, R. Lal, G. Arya, and S. Varghese. 2011. Engineering the cell-material interface for controlling stem cell adhesion, migration, and differentiation. Biomaterials 32:3700-3711.

125. Adhikari, A. S., J. Chai, and A. R. Dunn. 2011. Mechanical load induces a 100-fold increase in the rate of collagen proteolysis by MMP-1. J Am Chem Soc 133:1686-1689.

126. Beaty, B. T., and J. Condeelis. 2014. Digging a little deeper: The stages of invadopodium formation and maturation. Eur J Cell Biol 93:438-444.

127. Itoh, Y. 2006. MT1-MMP: A key regulator of cell migration in tissue. Iubmb Life 58:589-596.

128. Will, H., S. J. Atkinson, G. S. Butler, B. Smith, and G. Murphy. 1996. The soluble catalytic domain of membrane type 1 matrix metalloproteinase cleaves the propeptide of progelatinase A and initiates autoproteolytic activation - Regulation by TIMP-2 and TIMP-3. Journal of Biological Chemistry 271:17119-17123.

129. Itoh, Y., A. Takamura, N. Ito, Y. Maru, H. Sato, N. Suenaga, T. Aoki, and M. Seiki. 2001. Homophilic complex formation of MT1-MMP facilitates proMMP-2 activation on the cell surface and promotes tumor cell invasion. Embo Journal 20:4782-4793.

130. Li, X. Y., I. Ota, I. Yana, F. Sabeh, and S. J. Weiss. 2008. Molecular dissection of the structural machinery underlying the tissue-invasive activity of membrane type-1 matrix metalloproteinase. Mol Biol Cell 19:3221-3233.

131. Hotary, K., E. Allen, A. Punturieri, I. Yana, and S. J. Weiss. 2000. Regulation of cell invasion and morphogenesis in a three-dimensional type I collagen matrix by membrane-type matrix metalloproteinases 1, 2, and 3. Journal of Cell Biology 149:1309-1323.

132. Sabeh, F., I. Ota, K. Holmbeck, H. Birkedal-Hansen, P. Soloway, M. Balbin, C. Lopez-Otin, S. Shapiro, M. Inada, S. Krane, E. Allen, D. Chung, and S. J. Weiss. 2004. Tumor cell traffic through the extracellular matrix is controlled by the membrane-anchored collagenase MT1-MMP. Journal of Cell Biology 167:769-781.

133. Bravo-Cordero, J. J., R. Marrero-Diaz, D. Megias, L. Genis, A. Garcia-Grande, M. A. Garcia, A. G. Arroyo, and M. C. Montoya. 2007. MT1-MMP proinvasive activity is regulated by a novel Rab8-dependent exocytic pathway. Embo Journal

26:1499-1510.

134. Lafleur, M. A., F. A. Mercuri, N. Ruangpanit, M. Seiki, H. Sato, and E. W. Thompson. 2006. Type I collagen abrogates the clathrin-mediated internalization of membrane type 1 matrix metalloproteinase (MT1-MMP) via the MT1-MMP hemopexin domain. Journal of Biological Chemistry 281:6826-6840.

135. Remacle, A. G., D. V. Rozanov, P. C. Baciu, A. V. Chekanov, V. S. Golubkov, and A. Y. Strongin. 2005. The transmembrane domain is essential for the microtubular trafficking of membrane type-1 matrix metalloproteinase (MT1-MMP). J Cell Sci 118:4975-4984.

136. Itoh, Y., and M. Seiki. 2006. MT1-MMP: A potent modifier of pericellular microenvironment. J Cell Physiol 206:1-8.

137. Wakana, Y., J. van Galen, F. Meissner, M. Scarpa, R. S. Polishchuk, M. Mann, and V. Malhotra. 2012. A new class of carriers that transport selective cargo from the trans Golgi network to the cell surface. Embo J 31:3976-3990.

138. Wakana, Y., J. Villeneuve, J. van Galen, D. Cruz-Garcia, M. Tagaya, and V. Malhotra. 2013. Kinesin-5/Eg5 is important for transport of CARTS from the trans-Golgi network to the cell surface. Journal of Cell Biology 202:241-250.

139. Wang, P., X. Wang, and D. Q. Pei. 2004. Mint-3 regulates the retrieval of the internalized membrane-type matrix metalloproteinase, MT5-MMP, to the plasma membrane by binding to its carboxyl end motif EWV. Journal of Biological Chemistry 279:20461-20470.

140. Wang, X., D. W. Ma, J. Keski-Oja, and D. Q. Pei. 2004. Co-recycling of MT1-MMP and MT3-MMP through the trans-Golgi network - Identification of DKV582 as a recycling signal. Journal of Biological Chemistry 279:9331-9336.

141. Bretscher, M. S. 2008. On the shape of migrating cells - a 'front-to-back' model. J Cell Sci 121:2625-2628.

142. Clark, E. S., and A. M. Weaver. 2008. A new role for cortactin in invadopodia: Regulation of protease secretion. Eur J Cell Biol 87:581-590.

143. Sakurai-Yageta, M., C. Recchi, G. Le Dez, J. B. Sibarita, L. Daviet, J. Camonis, C. D'Souza-Schorey, and P. Chavrier. 2008. The interaction of IQGAP1 with the exocyst complex is required for tumor cell invasion downstream of Cdc42 and RhoA. Journal of Cell Biology 181:985-998.

144. Steffen, A., G. Le Dez, R. Poincloux, C. Recchi, P. Nassoy, K. Rottner, T. Galli, and P. Chavrier. 2008. MT1-MMP-dependent invasion is regulated by TI-VAMP/VAMP7. Current Biology 18:926-931.

145. Gong, X., C. Lin, J. Cheng, J. S. Su, H. Zhao, T. L. Liu, X. J. Wen, and P. Zhao. 2015. Generation of Multicellular Tumor Spheroids with Microwell-Based Agarose Scaffolds for Drug Testing. Plos One 10.

146. Mehta, G., A. Y. Hsiao, M. Ingram, G. D. Luker, and S. Takayama. 2012. Opportunities and challenges for use of tumor spheroids as models to test drug delivery and efficacy. J Control Release 164:192-204.

147. Tung, Y. C., A. Y. Hsiao, S. G. Allen, Y. S. Torisawa, M. Ho, and S. Takayama. 2011. High-throughput 3D spheroid culture and drug testing using a 384 hanging drop array. Analyst 136:473-478.

148. Chauhan, V. P., and R. K. Jain. 2013. Strategies for advancing cancer nanomedicine. Nat Mater 12:958-962.

149. Debnath, J., S. K. Muthuswamy, and J. S. Brugge. 2003. Morphogenesis and oncogenesis of MCF-10A mammary epithelial acini grown in three-dimensional basement membrane cultures. Methods 30:256-268.

150. Wei, S. C., L. Fattet, J. H. Tsai, Y. R. Guo, V. H. Pai, H. E. Majeski, A. C. Chen, R. L. Sah, S. S. Taylor, A. J. Engler, and J. Yang. 2015. Matrix stiffness drives epithelial mesenchymal transition and tumour metastasis through a TWIST1-G3BP2 mechanotransduction pathway. Nat Cell Biol 17:678-U306.

151. Xu, X., L. A. Gurski, C. Zhang, D. A. Harrington, M. C. Farach-Carson, and X. Q. Jia. 2012. Recreating the tumor microenvironment in a bilayer, hyaluronic acid hydrogel construct for the growth of prostate cancer spheroids. Biomaterials 33:9049-9060.

152. Albrecht, D. R., G. H. Underhill, T. B. Wassermann, R. L. Sah, and S. N. Bhatia. 2006. Probing the role of multicellular organization in three-dimensional microenvironments. Nat Methods 3:369-375.

153. Lovitt, C. J. S., T. B.; Avery, V. M. 2014. Advanced cell culture techniques for cancer drug discovery. Biology 3:345-367.

154. Seo, B. R., P. Bhardwaj, S. Choi, J. Gonzalez, R. C. A. Eguiluz, K. Wang, S. Mohanan, P. G. Morris, B. H. Du, X. K. Zhou, L. T. Vahdat, A. Verma, O. Elemento, C. A. Hudis, R. M. Williams, D. Gourdon, A. J. Dannenberg, and C. Fischbach. 2015. Obesity-dependent changes in interstitial ECM mechanics promote breast tumorigenesis. Sci Transl Med 7.

155. Upreti, M., A. Jamshidi-Parsian, N. A. Koonce, J. S. Webber, S. K. Sharma, A. A. A. Asea, M. J. Mader, and R. J. Griffin. 2011. Tumor-Endothelial Cell Three-dimensional Spheroids: New Aspects to Enhance Radiation and Drug Therapeutics. Transl Oncol 4:365-U138.

156. Kim, T., I. Doh, and Y. H. Cho. 2012. On-chip three-dimensional tumor spheroid formation and pump-less perfusion culture using gravity-driven cell aggregation and balanced droplet dispensing. Biomicrofluidics 6.

157. Sung, J. H., and M. L. Shuler. 2009. A micro cell culture analog (mu CCA) with 3-D hydrogel culture of multiple cell lines to assess metabolism-dependent cytotoxicity of anti-cancer drugs. Lab Chip 9:1385-1394.

158. Kwak, B., A. Ozcelikkale, C. S. Shin, K. Park, and B. Han. 2014. Simulation of complex transport of nanoparticles around a tumor using tumor-microenvironment-on-chip. J Control Release 194:157-167.

159. Chaw, K. C., M. Manimaran, E. H. Tay, and S. Swaminathan. 2007. Multi-step microfluidic device for studying cancer metastasis. Lab Chip 7:1041-1047.

160. Bersini, S., J. S. Jeon, G. Dubini, C. Arrigoni, S. Chung, J. L. Charest, M. Moretti, and R. D. Kamm. 2014. A microfluidic 3D in vitro model for specificity of breast cancer metastasis to bone. Biomaterials 35:2454-2461.

161. Bagley, A. F., R. Scherz-Shouval, P. A. Galie, A. Q. Zhang, J. Wyckoff, L. Whitesell, C. S. Chen, S. Lindquist, and S. N. Bhatia. 2015. Endothelial Thermotolerance Impairs Nanoparticle Transport in Tumors. Cancer Res 75:3255-3267.

162. Davey, S. K., A. Aung, G. Agrawal, H. L. Lim, M. Kar, and S. Varghese. 2015. Embedded 3D Photopatterning of Hydrogels with Diverse and Complex Architectures for Tissue Engineering and Disease Models. Tissue Eng Part C-Me 21:1188-1196.

163. Aung, A., I. S. Bhullar, J. Theprungsirikul, S. K. Davey, H. L. Lim, Y. J. Chiu, X. Y. Ma, S. Dewan, Y. H. Lo, A. McCulloch, and S. Varghese. 2016. 3D cardiac mu tissues within a microfluidic device with real-time contractile stress readout. Lab Chip 16:153-162.

164. Fairbanks, B. D., M. P. Schwartz, C. N. Bowman, and K. S. Anseth. 2009. Photoinitiated polymerization of PEG-diacrylate with lithium phenyl-2,4,6-trimethylbenzoylphosphinate: polymerization rate and cytocompatibility. Biomaterials 30:6702-6707.

165. Nichol, J. W., S. T. Koshy, H. Bae, C. M. Hwang, S. Yamanlar, and A. Khademhosseini. 2010. Cell-laden microengineered gelatin methacrylate hydrogels. Biomaterials 31:5536-5544.

166. Kang, H. M., Y. R. V. Shih, Y. Hwang, C. Wen, V. Rao, T. Seo, and S. Varghese. 2014. Mineralized gelatin methacrylate-based matrices induce osteogenic differentiation of human induced pluripotent stem cells. Acta Biomater 10:4961-

4970.

167. Aung, A., G. Gupta, G. Majid, and S. Varghese. 2011. Osteoarthritic Chondrocyte-Secreted Morphogens Induce Chondrogenic Differentiation of Human Mesenchymal Stem Cells. Arthritis Rheum-Us 63:148-158.

168. Kaemmerer, E., F. P. W. Melchels, B. M. Holzapfel, T. Meckel, D. W. Hutmacher, and D. Loessner. 2014. Gelatine methacrylamide-based hydrogels: An alternative three-dimensional cancer cell culture system. Acta Biomater 10:2551-2562.

169. Sun, Z. J., D. J. Murry, S. P. Sanghani, W. I. Davis, N. Y. Kedishvili, Q. Zou, T. D. Hurley, and W. F. Bosron. 2004. Methylphenidate is stereoselectively hydrolyzed by human carboxylesterase CES1A1. J Pharmacol Exp Ther 310:469-476.

170. Di Carlo, D., N. Aghdam, and L. P. Lee. 2006. Single-cell enzyme concentrations, kinetics, and inhibition analysis using high-density hydrodynamic cell isolation arrays. Anal Chem 78:4925-4930.

171. Chen, Y. L., Y. T. Tsai, C. Y. Lee, C. H. Lee, C. Y. Chen, C. M. Liu, J. J. Chen, S. H. Loh, and C. S. Tsai. 2014. Urotensin II Inhibits Doxorubicin-Induced Human Umbilical Vein Endothelial Cell Death by Modulating ATF Expression and via the ERK and Akt Pathway. Plos One 9.

172. Bar-Even, A., E. Noor, Y. Savir, W. Liebermeister, D. Davidi, D. S. Tawfik, and R. Milo. 2011. The Moderately Efficient Enzyme: Evolutionary and Physicochemical Trends Shaping Enzyme Parameters. Biochemistry-Us 50:4402-4410.

173. Liu, Y. A., and G. Zeng. 2012. Cancer and Innate Immune System Interactions: Translational Potentials for Cancer Immunotherapy. J Immunother 35:299-308.

174. Maude, S. L., N. Frey, P. A. Shaw, R. Aplenc, D. M. Barrett, N. J. Bunin, A. Chew, V. E. Gonzalez, Z. H. Zheng, S. F. Lacey, Y. D. Mahnke, J. J. Melenhorst, S. R. Rheingold, A. Shen, D. T. Teachey, B. L. Levine, C. H. June, D. L. Porter, and S. A. Grupp. 2014. Chimeric Antigen Receptor T Cells for Sustained Remissions in Leukemia. New Engl J Med 371:1507-1517.

175. Kochenderfer, J. N., and S. A. Rosenberg. 2013. Treating B-cell cancer with T cells expressing anti-CD19 chimeric antigen receptors. Nat Rev Clin Oncol 10:267-276.

176. Gettinger, S. N., L. Horn, L. Gandhi, D. R. Spigel, S. J. Antonia, N. A. Rizvi, J. D. Powderly, R. S. Heist, R. D. Carvajal, D. M. Jackman, L. V. Sequist, D. C. Smith, P. Leming, D. P. Carbone, M. C. Pinder-Schenck, S. L. Topalian, F. S. Hodi, J. A. Sosman, M. Sznol, D. F. McDermott, D. M. Pardoll, V. Sankar, C. M. Ahlers, M. Salvati, J. M. Wigginton, M. D. Hellmann, G. D. Kollia, A. K. Gupta, and J. R.

Brahmer. 2015. Overall Survival and Long-Term Safety of Nivolumab (Anti-Programmed Death 1 Antibody, BMS-936558, ONO-4538) in Patients With Previously Treated Advanced Non-Small-Cell Lung Cancer. J Clin Oncol 33:2004-U2032.

177. Topalian, S. L., F. S. Hodi, J. R. Brahmer, S. N. Gettinger, D. C. Smith, D. F. McDermott, J. D. Powderly, R. D. Carvajal, J. A. Sosman, M. B. Atkins, P. D. Leming, D. R. Spigel, S. J. Antonia, L. Horn, C. G. Drake, D. M. Pardoll, L. P. Chen, W. H. Sharfman, R. A. Anders, J. M. Taube, T. L. McMiller, H. Y. Xu, A. J. Korman, M. Jure-Kunkel, S. Agrawal, D. McDonald, G. D. Kollia, A. Gupta, J. M. Wigginton, and M. Sznol. 2012. Safety, Activity, and Immune Correlates of Anti-PD-1 Antibody in Cancer. New Engl J Med 366:2443-2454.

178. Newick, K. M., E; Albelda, S. M. 2016. Chimeric antigen receptor T-cell therapy for solid tumors. Molecular Therapy-Oncolytics 3.

179. Craddock, J. A., A. Lu, A. Bear, M. Pule, M. K. Brenner, C. M. Rooney, and A. E. Foster. 2010. Enhanced Tumor Trafficking of GD2 Chimeric Antigen Receptor T Cells by Expression of the Chemokine Receptor CCR2b. J Immunother 33:780-788.

180. Harlin, H., Y. Meng, A. C. Peterson, Y. Y. Zha, M. Tretiakova, C. Slingluff, M. McKee, and T. F. Gajewski. 2009. Chemokine Expression in Melanoma Metastases Associated with CD8(+) T-Cell Recruitment. Cancer Res 69:3077-3085.

181. Shiao, S. L. G., A.P.; Rugo, H.S.; Coussens, L.M. 2011. Immune microenvironments in solid tumors: new targets for therapy. Genes and Development 25:2559-2572.

182. Burkholder, B., R. Y. Huang, R. Burgess, S. H. Luo, V. S. Jones, W. J. Zhang, Z. Q. Lv, C. Y. Gao, B. L. Wang, Y. M. Zhang, and R. P. Huang. 2014. Tumor-induced perturbations of cytokines and immune cell networks. Bba-Rev Cancer 1845:182-201.

183. DeNardo, D., P. Andreu, and L. M. Coussens. 2010. Interactions between lymphocytes and myeloid cells regulate pro- versus anti-tumor immunity. Cancer Metast Rev 29:309-316.

184. Braumuller, H., T. Wieder, E. Brenner, S. Assmann, M. Hahn, M. Alkhaled, K. Schilbach, F. Essmann, M. Kneilling, C. Griessinger, F. Ranta, S. Ullrich, R. Mocikat, K. Braungart, T. Mehra, B. Fehrenbacher, J. Berdel, H. Niessner, F. Meier, M. van den Broek, H. U. Haring, R. Handgretinger, L. Quintanilla-Martinez, F. Fend, M. Pesic, J. Bauer, L. Zender, M. Schaller, K. Schulze-Osthoff, and M. Rocken. 2013. T-helper-1-cell cytokines drive cancer into senescence. Nature 494:361-365.

185. Schlecker, E., A. Stojanovic, C. Eisen, C. Quack, C. S. Falk, V. Umansky, and A. Cerwenka. 2012. Tumor-Infiltrating Monocytic Myeloid-Derived Suppressor Cells Mediate CCR5-Dependent Recruitment of Regulatory T Cells Favoring Tumor Growth. J Immunol 189:5602-5611.

186. Liou, G. Y., H. Doppler, B. Necela, M. Krishna, H. C. Crawford, M. Raimondo, and P. Storz. 2013. Macrophage-secreted cytokines drive pancreatic acinar-to-ductal metaplasia through NF-kappa B and MMPs. Journal of Cell Biology 202:563-577.

187. Biswas, S. K., and A. Mantovani. 2010. Macrophage plasticity and interaction with lymphocyte subsets: cancer as a paradigm. Nat Immunol 11:889-896.

188. Helmlinger, G., P. A. Netti, H. C. Lichtenbeld, R. J. Melder, and R. K. Jain. 1997. Solid stress inhibits the growth of multicellular tumor spheroids. Nat Biotechnol 15:778-783.

189. Hirschhaeuser, F., H. Menne, C. Dittfeld, J. West, W. Mueller-Klieser, and L. A. Kunz-Schughart. 2010. Multicellular tumor spheroids: An underestimated tool is catching up again. J Biotechnol 148:3-15.

190. Barbone, D., T. M. Yang, J. R. Morgan, G. Gaudino, and V. C. Broaddus. 2008. Mammalian target of rapamycin contributes to the acquired apoptotic resistance of human mesothelioma multicellular spheroids. Journal of Biological Chemistry 283:13021-13030.

191. Dardousis, K., C. Voolstra, M. Roengvoraphoj, A. Sekandarzad, S. Mesghenna, J. Winkler, Y. Ko, J. Hescheler, and A. Sachinidis. 2007. Identification of differentially expressed genes involved in the formation of multicellular tumor spheroids by HT-29 colon carcinoma cells. Mol Ther 15:94-102.

192. Kunz-Schughart, L. A. G., K.; Mueller-Klieser, W. 1996. Three-dimensional cell culture induces novel proliferative and metabolic alterations associated with oncogenic transformation. Internation Journal of Cancer 66:578-586.

193. Friedrich, J., R. Ebner, and L. A. Kunz-Schughart. 2007. Experimental anti-tumor therapy in 3-D: Spheroids - old hat or new challenge? Int J Radiat Biol 83:849-871.

194. Mueller-Klieser, W. 2000. Tumor biology and experimental therapeutics. Crit Rev Oncol Hemat 36:123-139.

195. Aung, A. T., J.; Lim, H. L.; Varghese, S. 2016. Chemotaxis-driven assembly of endothelial barrier in a tumor-on-a-chip platform. Lab Chip 16:1886-1898.

196. Cesano, A. S., D. 1992. Two unique human leukemic T-cell lines endowed with a stable cytotoxic function and a different spectrum of target reactivity analysis and

modulation of their lytic mechanisms. In Vitro Cell Developmental Biology 28A:648-656.

197. Kruse, C. A., S. Visonneau, B. K. Kleinschmidt-DeMasters, C. J. Gup, G. G. Gomez, D. B. Paul, and D. Santoli. 2000. The human leukemic T-cell line, TALL-104, is cytotoxic to human malignant brain tumors and traffics through brain tissue: Implications for local adoptive immunotherapy. Cancer Res 60:5731-5739.

198. Gomez, G. G., S. B. Read, L. E. Gerschenson, D. Santoli, A. Zweifach, and C. A. Kruse. 2004. Interactions of the allogeneic effector leukemic T cell line, TALL-104, with human malignant brain tumors. Neuro-Oncology 6:83-95.

199. Schmidt, T. L. 2010. Cytokine-induced killer cell trafficking to tumors: A chemokine-directed migration. Stanford University, Doctor of Philosophy Thesis.

200. Shekhar, M. P. V. 2011. Drug Resistance: Challenges to Effective Therapy. Curr Cancer Drug Tar 11:613-623.